



TECHNISCHE UNIVERSITÄT MÜNCHEN

Fakultät für Informatik

Lehrstuhl für Bildverarbeitung und Mustererkennung

**A Convex Optimization Framework for
Connectivity Constraints in Image Segmentation and
3D Reconstruction**

Jan Stühmer

Vollständiger Abdruck der von der Fakultät für Informatik der Technischen Universität München zur Erlangung des akademischen Grades eines

Doktors der Naturwissenschaften (Dr. rer. nat.)

genehmigten Dissertation.

Vorsitzender:

Prof. Dr. Nassir Navab

Prüfer der Dissertation:

1. Prof. Dr. Daniel Cremers

2. Prof. William T. Freeman

Massachusetts Institute of Technology

Cambridge, MA, USA

Die Dissertation wurde am 17.08.2016 bei der Technischen Universität München eingereicht und durch die Fakultät für Informatik am 07.11.2016 angenommen.

Summary

This thesis presents a framework for image segmentation and 3D reconstruction under topological constraints, specifically constraints on the connectivity of the reconstructed object, a problem class that is not yet sufficiently solved by existing methods.

Image segmentation, the partition of an image into meaningful parts, is one of the most important and well studied problems in Computer Vision. This stems on the one hand from its high importance for practical applications, often the first step towards a semantic interpretation of the image data, for example in object detection and classification, or image based quantification in medical imaging. On the other hand, image segmentation problems are interesting from a theoretical perspective. Even moderate tasks, for example segmenting an image into more than two regions, result in problems which remain hard to solve and require advanced knowledge in mathematical optimization.

Although the field has been studied for decades, existing methods often share a common drawback. They fail in cases when the object of interest has an elongated and thin shape. This occurs often in practical applications, for example the segmentation of blood vessels in medical imaging or in 3D reconstruction, when the object contains thin or small detailed structures.

In this thesis, we present a framework for image segmentation and 3D reconstruction, that is specifically successful in these cases of thin and elongated structures and allows improved results in comparison to existing methods. The framework allows to incorporate constraints on the topology of the object, specifically on its connectedness. The major contribution of this thesis is, that the constraints can be formulated as linear constraints in a convex optimization framework, which allows to solve the resulting optimization problem to global optimality. In comparison to most prior work, the method is very efficient both in runtime and memory requirements, which allows applications on large scale practical problems in medical imaging and 3D reconstruction. Furthermore, an efficient projection method onto the feasible set is presented, that significantly reduces the runtime complexity in cases when the connections have to span larger distances.

Additionally, the thesis presents an approach to define a probabilistic model of the data term used for image segmentation and, based on the uncertainty of the classifier, to improve the probabilistic model over time by presenting informative queries to the user. Furthermore, we present two real-time capable approaches: an improvement of our previously published real-time dense geometry reconstruction method, and a novel approach for model based object tracking with phase based Time-of-Flight depth cameras.

keywords: image segmentation, 3D reconstruction, convex optimization, topological constraints, connectedness

Zusammenfassung

Diese Arbeit beschreibt eine einheitliche Formulierung des Problems der Bildsegmentierung und 3D Rekonstruktion, die es erlaubt Nebenbedingungen über die Topologie des rekonstruierten Objektes zu formulieren, eine Problemstellung die von bisherigen Ansätzen nur unzureichend für praktische Anwendungen gelöst wurde.

Die Problemstellung der Bildsegmentierung, der Aufteilung eines Bildes in spezifische Teilsegmente, ist eines der am längsten und besten untersuchten Teilgebiete des Forschungsfeldes "Maschinelles Sehen". Dies ist zum einen durch die hohe praktische Relevanz der Problemstellung gegeben, meist ist die Bildsegmentierung eine Voraussetzung für eine semantische Analyse von Bilddaten, zum Beispiel für die Objekt-Detektion und Klassifizierung und bei Anwendungen in der medizinischen Bildverarbeitung zur bildbasierten Quantifizierung. Zum anderen sind Bildsegmentierungsprobleme aus algorithmisch-analytischer Perspektive interessant: Bereits relativ einfache Aufgaben, zum Beispiel die Segmentierung in mehr als zwei Regionen, resultieren in mathematisch anspruchsvolle Problemstellungen und erfordern fortgeschrittene Methoden der mathematischen Optimierung.

Obwohl das Aufgabengebiet der Bildsegmentierung bereits seit mehreren Jahrzehnten erforscht wird, sind existierende Verfahren unzureichend, wenn das zu rekonstruierende Objekt dünne Strukturen aufweist. Dies ist in der Praxis ein häufig auftretendes Problem, zum Beispiel bei der Segmentierung von Blutgefäßen in der medizinischen Bildverarbeitung.

In dieser Arbeit wird ein Methode zur Bildsegmentierung und 3D Rekonstruktion vorgestellt, die insbesondere in solchen Fällen von dünnen Strukturen eine deutliche Verbesserung der Ergebnisse im Vergleich zu existierenden Verfahren erzielt. Der Ansatz erlaubt, Nebenbedingungen über die Topologie des zu rekonstruierenden Objektes zu formulieren, insbesondere über die Konnektivität des Objektes. Einer der Hauptbeiträge der Arbeit ist, dass sich die Nebenbedingungen als lineare Nebenbedingungen in einem Ansatz der konvexen Optimierung formulieren lassen. Hierdurch ist es möglich, das resultierende Optimierungsproblem global optimal zu lösen. Im Vergleich zu existierenden Ansätzen ist das vorgestellte Verfahren sehr effizient im Hinblick auf Laufzeit und Speicher, und erlaubt daher die praktische Anwendung bei Fragestellungen größerer Komplexität, zum Beispiel in der medizinischen Bildverarbeitung von dreidimensionalen Datensätzen der Computertomographie oder der 3D Rekonstruktion von dynamischen Szenen. Darüberhinaus wird ein effizientes Projektionsverfahren auf den Lösungsraum vorgestellt, der die Laufzeit besonders in solchen Fällen signifikant verkürzt, in denen Verbindungen größerer Distanz zwischen den einzelnen Teilen des Objektes gefunden werden müssen.

Weitere Teile der Arbeit umfassen die Bestimmung eines Modells für den Datenterm des Segmentierungsmodells mit Hilfe von Gauß-Prozessen, das basierend auf der Unsicherheit der Klassifikation verbessert wird, indem unsicher klassifizierte Bildbereiche identifiziert und dem Benutzer zu Begutachtung präsentiert werden. Darüberhinaus enthält diese Arbeit zwei echtzeitfähige Verfahren: eine Verbesserung unseres Ansatzes zur Schätzung von dichten Tiefenkarten aus mehreren Bildern, sowie einen neuartigen Ansatz zur Objektverfolgung mit Hilfe von phasenmodulierten Tiefenkameras.

Stichworte: Bildsegmentierung, 3D-Rekonstruktion, Konvexe Optimierung, Topologische Nebenbedingungen, Konnektivität

Acknowledgements

Thanks to all the people who supported me during the years, first and foremost my advisors: My supervisor **Daniel Cremers**, who enabled me to learn and explore the various fields which are touched by computer vision, among them the theory of convex optimization, differential geometry, computational topology, discrete optimization and machine learning. Thanks for all the freedom to explore. My co-advisor **Peter Schröder**, who introduced me to the field of discrete differential geometry and enabled me to learn mathematics in such an inspiring and cheerful way, and who managed to find time to listen to my ideas, even with nine hours of time shift. Thanks to **Sebastian Nowozin** and **Jamie Shotton**, for this productive, cooperative and very joyful working experience at Microsoft Research Cambridge, where I learned a lot about probabilistic models and the propagation of light, not to forget the foosball matches.

Then there were my colleagues at the **Computer Vision Group** at TUM, who I thank for inspiring discussions, all the good times during coffee breaks, group retreats, our spare time and the lively atmosphere during the seminars. Thanks to Michael, for his precision in answering mathematical questions, his overall excitement about math, and for proofreading the manuscript. Thanks to Rudolph for the great atmosphere in our office, explanation of uncertainty in machine learning and associated white board sketches, and for proofreading the manuscript. Thank you Thomas and Thomas, for inspiring mathematical discussions that delve into the fascinating world of convex optimization, topology and measure theory, and for proofreading the manuscript. Thanks to Christian for proofreading the manuscript. Special thanks to Konstantin, for discussing convex optimization and proximal algorithms with me, and for proofreading the manuscript. At **Caltech**, there were also so many people who supported me: Armeen, Keenan, Michael, Albert, Fernando, Martin, Daniela and Justin.

I am also very grateful to the **TUM Institute for Advanced Studies** for funding and the opportunity to broaden my knowledge at inspiring talks, seminars, and lectures, and to the **European Research Council** for funding.

Table of Contents

Summary	iii
Acknowledgements	vii
Table of Contents	ix

Part I	Introduction	1
1	Introduction	3
1.1	Key Contributions	4
1.2	Outline of the Thesis	5
1.3	Publications	6
1.4	Collaborations	6
1.5	Notation and Mathematical Symbols	7
2	Introductory Material on Convex Optimization	9
2.1	Convex Analysis	9
2.2	Convex Optimization Problem	9
2.3	Convex Conjugate	10
2.4	Lagrange Duality	11
2.4.1	Weak and Strong and Duality	11
2.4.2	Legendre-Fenchel Transform and the Lagrangian	12
2.5	Primal-Dual Hybrid Gradient Method	14
3	Total Variation and its Minimization	15
3.1	Definition of Total Variation	15
3.2	Minimizing Functionals with Total Variation Regularizer as Saddle Point Problem	16
3.3	Geometric Interpretation of the Total Variation	16
3.4	The Coarea Formula	16
3.5	Total Variation as Regularizer in Image Segmentation and 3D Reconstruction	17
3.6	The Shrinking Bias	17
4	Connectedness as Topological Property	19
4.1	Connectedness of Topological Spaces	19
4.1.1	Path Connectedness	19
4.1.2	Simply Connected Topological Space	20
4.2	Connectedness of a Graph	21
4.2.1	k-Connected Graph	21

Part II	Image Segmentation	23
----------------	---------------------------	-----------

5	Connectivity Constraints for Image Segmentation	25
5.1	Introduction	25
5.1.1	Related Work	27
5.1.2	Problem Formulation	28
5.2	The Continuous Case: Connectivity Along Geodesics	29
5.2.1	An Image Depending Geodesic Topology	29
5.2.2	Connectivity Constraint as Monotonicity Constraint	30
5.2.3	The Thresholding Theorem	30
5.3	Image Segmentation on the Discrete Domain of a Weighted Graph	32
5.3.1	Gradient and Divergence Operators on Weighted Graphs	33
5.3.2	The Segmentation Model in the Weighted Graph Framework	34
5.3.3	A Primal-Dual Method for Vertex Labeling	34
5.3.4	Comparison of the Primal Dual Algorithm on a Graph and the Graph-Cut Framework	36
5.4	The Connectivity Constraint on a Discrete Domain	36
5.4.1	Discrete Geodesics	36
5.4.2	Legendre-Fenchel Duality	40
5.5	Experimental Results	40
5.6	Conclusion	44
6	A Fast Projection Method for Connectivity Constraints	45
6.1	Introduction	45
6.2	Connectivity Constraints in Image Segmentation	46
6.3	Constrained Convex Optimization	47
6.3.1	Optimization via Fenchel Duality	48
6.3.2	Projection onto the Constraint Set	48
6.3.3	Isotonic Regression on a Tree	49
6.4	Experimental Results	52
6.5	Conclusion	58
7	Active Online Learning using Sparse Gaussian Processes	59
7.1	Introduction	59
7.1.1	Related Work	60
7.2	Algorithm Overview	61
7.3	Gaussian Process Classification	63
7.3.1	Information-theoretic Sparsification	63
7.4	Online Update of the IVM	64
7.4.1	Efficient Online Computation of the Class Prediction	64
7.5	Segmentation Model	66
7.6	Experimental Results	67
7.6.1	Benefits of the GP classifier	68
7.6.2	Advantage of the Online Inference Algorithm	69
7.7	Conclusion	69

Part III	3D Reconstruction and Tracking	71
-----------------	---------------------------------------	-----------

8	Connectivity in 3D Reconstruction	73
8.1	Introduction	73
8.1.1	Contributions	74
8.1.2	Related Work	74
8.2	3D Reconstruction with Connectivity Constraints	75
8.2.1	Spatio-temporal Multi-view Reconstruction	75
8.2.2	Connectivity Constraints for 3D Reconstruction	77
8.3	Loop Connectivity	78
8.3.1	Loop Connectivity Constraints	78
8.3.2	Handle and Tunnel Loops	80
8.4	Numerical Optimization	83
8.5	Experiments	85
8.6	Conclusion	87
9	The Direct Geometry Approach for Real-Time 3D Reconstruction	89
9.1	Introduction	89
9.2	Dense Depth Map Estimation from Multiple Images	90
9.2.1	Half Quadratic Splitting	91
9.3	Dualization of the Data Term	92
9.3.1	Infimal Convolution and the Huber loss	94
9.3.2	Huber-TV for Depth Map Estimation	95
9.4	Implementation	96
9.5	Experimental Results	96
9.6	Conclusion	100
10	3D Tracking from Raw ToF data	101
10.1	Introduction	101
10.2	Background	104
10.2.1	Phase-Modulation Time-of-Flight	104
10.2.2	Model-Based Tracking	105
10.3	Method	106
10.3.1	Motion model $P(X_{t+1} X_t)$	106
10.3.2	Observation model $P(Y_t X_t)$ for raw ToF	107
10.4	Implementation and Validation	109
10.5	Experiments	111
10.5.1	Failure of Depth Based Tracking	112
10.5.2	Tracking with Raw ToF Observations	113
10.5.3	Benefit of Equispacing	113
10.6	Discussion	114
10.6.1	Tracking from Raw ToF	114
10.6.2	Equispaced ToF Captures	115
10.6.3	Limitations and Future Work	115
10.7	Conclusion	115

Part IV	Conclusions and Outlook	117
11	Concluding Remarks	119
11.1	Summary	119
11.2	Advantages	119
11.3	Limitations and Future Work	120
	References	123

Part I.

Introduction

1. Introduction

Current state-of-the-art image segmentation methods fail when the object, that should be segmented, contains thin small scale structures. This is due to the so called shrinking bias of the commonly used boundary length regularizer: the regularizer favors compact and round objects, which results in thin structures being removed from the foreground region.

Segmentation problems with thin, fine-scale details frequently arise in several areas of computer vision. The most prominent ones are in medical applications, *e.g.* when segmenting the vascular network, which allows biophysical simulations of the blood flow, or when segmenting neural structures in microscopy images. Another application area is in satellite imagery, where street networks and rivers should be detected.

We propose to use topological constraints to preserve these thin structures and impose connectedness of the segmented region, which also acts as a regularizer that suppresses noise and spurious detections, and furthermore fills and re-connects incomplete areas. We show that connectivity constraints are well suited for interactive segmentation, by allowing to extract a single connected component with user interactive definition of object parts that should be connected to the foreground component. Also, we show that connectivity constraints greatly improve current state-of-the-art methods for multiview 3D scene reconstruction, especially when the scene contains thin fine-scaled details. This allows to reconstruct even very thin object parts, that previously could not be reconstructed with existing methods.

In Fig. 1.1 we depict several application areas of connectivity constraints in computer vision. In multiview 3D reconstruction of dynamic scenes, the connectivity constraints allow to reconstruct thin structures, in this example a rope, which otherwise are very hard to reconstruct by state-of-the-art approaches. Other application areas include biomedical image segmentation of 2D data, here blood vessel segmentation in the retina, as well as of 3D data, in this case 3D CT angiography of the vascular tree in the lung. Especially

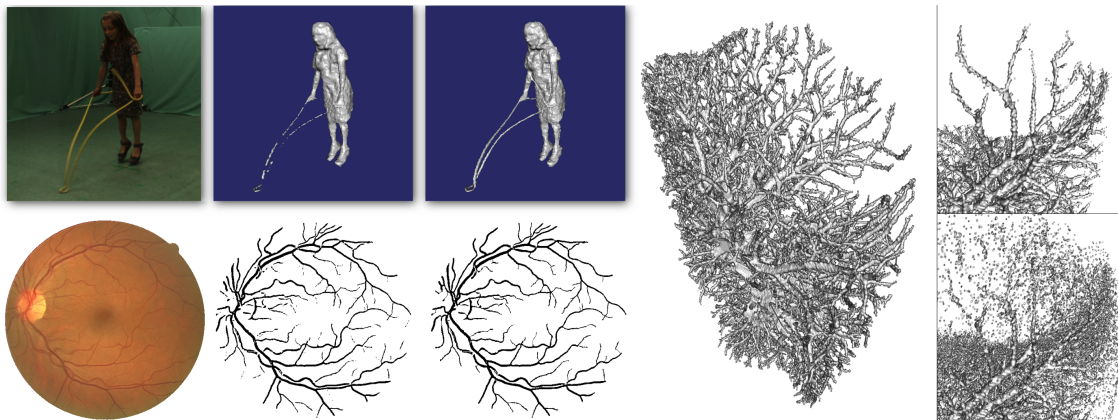


Figure 1.1.: Segmentation problems with thin, fine-scale details arise in several areas of computer vision and medical imaging. Top left: 3D multiview dynamic scene reconstruction. Right: CT angiography. Bottom Left: Segmentation of the retinal vascular tree.

the 3D angiography example depicts the benefits of the proposed approach: it allows to remove noise from the data and to fill in missing parts of the foreground.

1.1. Key Contributions

This thesis presents the first practicable approach for connectivity constraints in image segmentation and 3D reconstruction. These two application domains are covered in Part II and Part III respectively. Further results include a method for active learning in image segmentation, a review and extension of our work on real-time dense geometry reconstruction, and a novel approach for real-time object tracking with a time-of-flight camera.

Image Segmentation with Connectivity Constraints

In Part II of this thesis, we present a very efficient method for connectivity constraints in image segmentation. In contrast to previous approaches, that aim to approximate a solution to the underlying NP hard optimization problem, we propose to reformulate the connectivity constraint along geodesics in the image domain. The main advantage of the proposed approach is that the resulting optimization problem is convex, and can be solved to global optimality. Furthermore, the result is independent of the initialization and only depends on the chosen root of the geodesics. In contrast to graph-cut based methods, the proposed approach does not suffer from metrication artifacts. A recent study of Rempfler *et al.* [117] evaluates the proposed method in comparison to an exact global optimal solution and finds no difference regarding F1-measure, precision, and recall on a medical image segmentation benchmark.

Connectivity Constraints for Image Segmentation The general framework for connectivity constraints is described in Chapter 5 where we propose to formulate the constraints along geodesics in the image domain. We include the constraints in a continuous image segmentation framework and provide a proof of the thresholding theorem, which states that a thresholded version of a solution to the relaxed problem is an optimal solution of the original discrete image segmentation problem. The constrained optimization problem is convex, and the constraints are included via Legendre-Fenchel duality. Furthermore, we derive a formulation of the primal-dual hybrid gradient method on the domain of a discrete graph.

Direct Projection onto the Constraint Set In Chapter 6 we provide an alternative approach to solve the resulting constrained optimization problem, and present an efficient projection method that allows a direct projection onto the feasible set. Especially for long range connections the method is by several orders of magnitudes faster than the approach based on Legendre-Fenchel duality, reducing the required run-time from hundreds of seconds to well below 10 seconds for medium problem sizes.

Active Learning for Image Segmentation Chapter 7 describes an active learning framework to train a classifier for image segmentation. Based on the classification uncertainty, the method queries additional labels for previously unlabeled regions from the user and subsequently improves the segmentation. The method is especially useful for large image datasets, for example satellite imagery and volumetric data in medical

imaging, where it is unfeasible to manually correct the classification result. We validate in experiments, that the uncertainty based queries quickly improve the classification performance.

3D Reconstruction and Tracking

In Part III, we describe several contributions for image based 3D reconstruction, including the first method for connectivity constraints in multi-view 3D reconstruction, an improved version of our real time dense reconstruction method, and a novel approach for object tracking with a time-of-flight camera.

Connectivity in 3D Reconstruction We present the first method which includes topological constraints into multi-view 3D reconstruction. By combining a recent method for dynamic 3D reconstruction with the proposed framework for connectivity constraints, we can clearly improve the state-of-the-art, especially in case of very thin object parts, that cannot be sufficiently reconstructed with existing methods.

Real-time Dense 3D Reconstruction We review our seminal work for real-time dense multi-view 3D reconstruction and extend it by introducing dual variables in the data term. In contrast to the previously used half-quadratic splitting method, the proposed method allows to compute an exact minimizer of every linearized sub-problem. Furthermore, we discuss the connection between half quadratic splitting and infimal convolution and from these considerations motivate to use the Huber loss in the regularizer of the depth map.

Raw Time-of-Flight based Tracking We propose a novel approach for model based object tracking by directly tracking the object in the raw infrared signal of a time-of-flight camera. The proposed method is able to track and to infer the depth of even very quickly moving objects, for which the usual approach of first performing a depth reconstruction and then tracking in the reconstructed depth image fails. In contrast to the standard approach, the proposed method is not affected by the motion artifacts from phase unwrapping of the time-of-flight signal. Additionally, we propose an equidistant exposure timing, which is more suitable for object tracking than the standard exposure timing of a time-of-flight camera.

1.2. Outline of the Thesis

In Chapter 2 we give an introduction to several concepts from convex optimization which will be used throughout the thesis, including convex analysis, the convex conjugate, Lagrange duality, conditions for weak and strong duality, and the primal-dual hybrid gradient method. In Chapter 3 we describe the total variation of a function, its geometric interpretation, and how it can be minimized using the mathematical concepts described in Chapter 2. In Chapter 4 we give an introduction to connectedness, as property of topological spaces, and in the context of graph theory, which concludes the introductory material.

The following two parts II and III contain the contributions discussed above, with the general topic of image segmentation in Part II and 3D reconstruction in Part III. The

thesis is concluded in Chapter 11 which provides an overview of the achieved results and discusses possible directions for future research.

1.3. Publications

Most of the work in this thesis appears in the following publications:

- [1] J. Stühmer, S. Nowozin, A. Fitzgibbon, R. Szeliski, T. Perry, S. Acharya, D. Cremers, and J. Shotton. Model-Based Tracking at 300Hz using Raw Time-of-Flight Observations. In *Proc. International Conference on Computer Vision*. Santiago, Chile, 2015.
- [2] J. Stühmer and D. Cremers. A Fast Projection Method for Connectivity Constraints in Image Segmentation. In X.-C. Tai, E. Bae, T. F. Chan, and M. Lysaker (Editors), *Proceedings of the International Conference on Energy Minimization Methods in Computer Vision and Pattern Recognition*, LNCS. 2015. (Oral Presentation).
- [3] M. R. Oswald, J. Stühmer, and D. Cremers. Generalized Connectivity Constraints for Spatio-temporal 3D Reconstruction. In *Proc. European Conference on Computer Vision*, pages 32–46. 2014.
- [4] R. Triebel, J. Stühmer, M. Souiai, and D. Cremers. Active Online Learning for Interactive Segmentation using Sparse Gaussian Processes. In *German Conference on Pattern Recognition*. 2014.
- [5] J. Stühmer, P. Schröder, and D. Cremers. Tree Shape Priors with Connectivity Constraints using Convex Relaxation on General Graphs. In *Proc. International Conference on Computer Vision*. Sydney, Australia, 2013. (Oral Presentation).

The following publications contain parts of my Diploma thesis [134] and are the foundation of Chapter 9:

- [6] J. Stühmer, S. Gumhold, and D. Cremers. Real-time Dense Geometry from a Handheld Camera. In *Pattern Recognition (Proc. DAGM)*, pages 11–20. Darmstadt, Germany, 2010. (Oral Presentation). (Part of Diploma Thesis).
- [7] J. Stühmer, S. Gumhold, and D. Cremers. Parallel Generalized Thresholding Scheme for Live Dense Geometry from a Handheld Camera. In *ECCV Workshop on Computer Vision on GPUs (CVGPU)*. Heraklion, Greece, 2010. (Oral Presentation). (Part of Diploma Thesis).

This thesis extends the work from the Diploma thesis by a dual optimization scheme for the data term and a robust Huber loss for the regularizer.

1.4. Collaborations

The research presented in this thesis was partly conducted as a member of the student researcher visiting program at the California Institute of Technology, Pasadena, USA, and the research intern program at Microsoft Research Cambridge, UK.

1.5. Notation and Mathematical Symbols

α	a scalar
x	a vector
\mathbb{R}	the real numbers
$\mathbb{R}_{\geq 0}$	positive real numbers (including zero)
I	an image
Ω	the image domain
$\Sigma_{f>\mu}$	the upper levelset of a function f thresholded at the value μ
∇	gradient operator
div	divergence operator
$\partial_i f_j$	for a function f , defined over the vertices of a graph, this is the directional derivative along the edge ij
π	projection
Π	orthogonal projection onto a set
G	graph
T_s	tree with root vertex s
\mathcal{N}	neighborhood of a vertex
V	vertex set of a graph
E	edge set of a graph
E_T	edge set of the tree T
\mathbb{V}	volume domain
\mathbb{T}	time domain
$\mathbb{V} \times \mathbb{T}$	space-time domain
Σ	surface
$int(\Sigma)$	surface interior
$ext(\Sigma)$	surface exterior

2. Introductory Material on Convex Optimization

This chapter gives an introduction to convex optimization methods, which provide a unifying framework for many of the algorithms derived in this thesis. Throughout the chapter, we follow the definitions and notation of Boyd and Vandenberghe [17] and Parikh and Boyd [110] while adding some additional remarks on the equivalence of the Legendre-Fenchel-transform and Lagrangian multipliers in convex optimization. Furthermore, we add references to relevant algorithms in the field of computer vision when necessary.

2.1. Convex Analysis

Affine Set We consider the set $C \subset \mathbb{R}^n$. Let x and x' be two distinct points in C . The set C is called *affine* if the line through x and x' lies in C , i.e. if for any $x, x' \in C$ and $\theta \in \mathbb{R}$, we have $\theta x + (1 - \theta)x' \in C$ [17].

We extend this concept and consider a set of points x_1, \dots, x_k and a set of coefficients $\theta_1, \dots, \theta_k$ with $\theta_1 + \dots + \theta_k = 1$, i.e. that sum up to one, and call a point $\theta_1 x_1 + \dots + \theta_k x_k$ an *affine combination* of the points x_1, \dots, x_k .

The set of all affine combinations of points in a set $C \subset \mathbb{R}^n$ is called the *affine hull* of C , which we denote with **aff**.

Relative Interior The *relative interior* of a set C is defined as

$$\mathbf{relint} C = \{x \in C \mid B(x, r) \cap \mathbf{aff} C \subset C \text{ for some } r > 0\}, \quad (2.1)$$

where $B(x, r) = \{y \mid \|y - x\| \leq r\}$ is a ball of radius r centered at x . The norm $\|\cdot\|$ can be any norm, and all norms define the same relative interior [17].

Convex Set We consider the set $C \subset \mathbb{R}^n$. Let x and x' be two distinct points in C . The set C is called *convex* if the line segment between x and x' lies in C , i.e. if for any $x, x' \in C$ and $\theta \in \mathbb{R}$ with $0 \leq \theta \leq 1$, it holds that $\theta x + (1 - \theta)x' \in C$ [17].

2.2. Convex Optimization Problem

In mathematical optimization, a *convex optimization problem* is of the form

$$\begin{aligned} & \text{minimize} && f_0(x) \\ & \text{s.t.} && f_i(x) \leq b_i, \quad i = 1, \dots, m, \end{aligned} \quad (2.2)$$

where the functions $f_0, \dots, f_m : \mathbb{R}^n \mapsto \mathbb{R} \cup \{+\infty\}$ are *convex*, which means that they satisfy

$$f_i(\alpha x + \beta y) \leq \alpha f_i(x) + \beta f_i(y)$$

for all $x, y \in \mathbf{dom} f$ and all $\alpha, \beta \in \mathbb{R}$ with $\alpha + \beta = 1$, $\alpha \geq 0$, $\beta \geq 0$, and $\mathbf{dom} f_i$ are convex sets for $i = 0, \dots, m$.

With $\mathbf{dom} f$ we denote the *effective domain* of a function f which is defined as

$$\mathbf{dom} f = \{x \in \mathbb{R}^n \mid f(x) < +\infty\}, \quad (2.3)$$

thus it is the set of points for which f maps to finite values.

Fundamental for this research is the following property:

Theorem 2.2.1. *Every locally optimal point of (2.2) is globally optimal.*

Proof [17]. To show this, let us assume that x is a locally optimal point of a convex optimization problem. This means x is feasible and for some $R > 0$ it holds that

$$f_0(x) = \inf\{f_0(z) \mid z \text{ feasible, } \|z - x\|_2 \leq R\}. \quad (2.4)$$

Let us assume that x is not globally optimal, then there has to exist a feasible y with $f_0(y) < f_0(x)$. From (2.4) it follows that $\|y - x\|_2 > R$, otherwise the globally optimal point would be within the distance R considered for the locally optimal point.

We consider a point z , a linear combination of x and y

$$z = (1 - \theta)x + \theta y$$

for some

$$0 < \theta < \frac{R}{\|y - x\|_2}$$

such that $\|z - x\|_2 < R$. From convexity of the feasible set it follows that this point z is feasible. Because f_0 is convex it follows that

$$f_0(z) \leq (1 - \theta)f_0(x) + \theta f_0(y)$$

and from $\theta > 0$ and $f_0(y) < f_0(x)$ that

$$f_0(z) < f_0(x)$$

which contradicts (2.4). □

2.3. Convex Conjugate

Let $f : \mathbb{R}^n \mapsto \mathbb{R} \cup \{+\infty\}$. The *convex conjugate* $f^* : \mathbb{R}^n \mapsto \mathbb{R} \cup \{+\infty\}$ of the function f is defined as the supremum

$$f^*(y) = \sup_{x \in \mathbf{dom} f} (y^T x - f(x)), \quad (2.5)$$

It is also known as the *Legendre-Fenchel transform* of f .

The Fenchel *bi-conjugate* f^{**} yields the *convex envelope*, the largest closed convex underapproximation of f [17]. Furthermore, an important property of the bi-conjugate is that $f = f^{**}$ iff f is convex and lower semi-continuous, which in finite dimensions holds for all convex functions with closed *epigraph* and nonempty domain, where the *epigraph* of a convex function f is defined as

$$\mathbf{epi}(f) = \{(x, d) \in \mathbb{R}^{n+1} \mid f(x) \leq d\}. \quad (2.6)$$

2.4. Lagrange Duality

Let's consider the following *constrained optimization problem* [17]

$$\begin{aligned} & \text{minimize} && f_0(x) \\ & \text{s.t.} && f_i(x) \leq 0, \quad i = 1, \dots, m \\ & && h_i(x) = 0, \quad i = 1, \dots, p. \end{aligned} \tag{2.7}$$

The variable $x \in \mathbb{R}^n$ is the *optimization variable* and the function $f_0 : \mathbb{R}^n \mapsto \mathbb{R}$ is called the *objective function*. The inequalities $f_i(x) \leq 0$ are called the *inequality constraints* and the functions $f_i(x) : \mathbb{R}^n \mapsto \mathbb{R}$ are the *inequality constraint functions*. Correspondingly, the equations $h_i(x) = 0$ are called the *equality constraints* and the functions $h_i(x) : \mathbb{R}^n \mapsto \mathbb{R}$ are the *equality constraint functions*. Because the right hand side of the constraints is 0, this optimization problem is considered being in *standard form*. We do not necessarily assume that the optimization problem is convex.

The associated *Lagrangian* $L : \mathbb{R}^n \times \mathbb{R}^m \times \mathbb{R}^p \mapsto \mathbb{R}$ is defined as

$$L(x, \lambda, \mu) = f_0(x) + \sum_{i=1}^m \lambda_i f_i(x) + \sum_{i=1}^p \mu_i h_i(x). \tag{2.8}$$

The variables λ_i and μ_i are called *Lagrange multiplier* and their vectors λ and μ are called *dual variables*.

The *Lagrange dual function* $g : \mathbb{R}^m \times \mathbb{R}^p \mapsto \mathbb{R} \cup \{-\infty\}$ is defined as the minimum value of the Lagrangian over x :

$$g(\lambda, \mu) = \inf_x L(x, \lambda, \mu) = \inf_x \left(f_0(x) + \sum_{i=1}^m \lambda_i f_i(x) + \sum_{i=1}^p \mu_i h_i(x) \right). \tag{2.9}$$

For $\lambda \geq 0$ the Lagrange dual yields a lower bound on the optimal value of (2.7). Maximization of this lower bound leads to the *Lagrange dual problem* associated to (2.7)

$$\begin{aligned} & \sup_{\lambda, \mu} && g(\lambda, \mu) \\ & \text{s.t.} && \lambda \geq 0. \end{aligned} \tag{2.10}$$

2.4.1. Weak and Strong and Duality

So far we only have the guarantee, that the optimal value of the Lagrange dual problem (2.10), which we denote with d^* , gives the maximum lower bound on the optimal value of the original constrained optimization problem (2.7), which we denote with p^* :

$$d^* \leq p^* \tag{2.11}$$

This property of the Lagrange dual holds even when the original problem is not convex and is called *weak duality*.

When this property holds as equality

$$d^* = p^*$$

we say that *strong duality* holds. In this case, the *optimal duality gap* $p^* - d^*$ is zero, and we say that the maximum lower bound retrieved by the Lagrange dual is tight.

Strong duality holds when special conditions on the constraints are fulfilled, the so called *constraint qualifications*.

In case the primal problem is convex, with f_0, \dots, f_m convex, and h_1, \dots, h_p affine, one of these constraint qualifications is *Slater's condition*, which holds when there exists an x in the relative interior of the domain, $x \in \mathbf{relint} \mathcal{D}$, such that it is strictly feasible:

$$f_i(x) < 0, \quad i = 1, \dots, m, \quad \text{and} \quad h_j(x) = 0, \quad j = 1, \dots, p.$$

When also some of the inequality constraint functions f_i are affine, Slater's condition can be refined: Let the first k functions f_1, \dots, f_k be affine, then strong duality holds provided that there exists an x in the relative interior of the domain with

$$f_i(x) \leq 0, \quad i = 1, \dots, k, \quad f_i(x) < 0, \quad i = k + 1, \dots, m, \quad \text{and} \quad h_j(x) = 0, \quad j = 1, \dots, p.$$

The interesting property of this refined Slater condition is, that Slater's condition reduces to feasibility when all of the constraint functions are affine. Thus feasibility of the solution of a convex optimization problem with affine constraints is already a sufficient condition for strong duality.

2.4.2. Legendre-Fenchel Transform and the Lagrangian

The Legendre-Fenchel transform and the Lagrangian are closely related. Let us again consider the constrained optimization problem in standard form (2.7)

$$\begin{aligned} & \text{minimize} && f_0(x) \\ & \text{s.t.} && f_i(x) \leq 0, \quad i = 1, \dots, m \\ & && h_i(x) = 0, \quad i = 1, \dots, p. \end{aligned} \tag{2.12}$$

We define the *indicator functions* of the inequality constraints as

$$\delta_{\leq 0}(f_i(x)) = \begin{cases} 0 & \text{if } f_i(x) \leq 0, \\ +\infty & \text{else.} \end{cases} \tag{2.13}$$

Correspondingly, the indicator functions of the equality constraints are defined as

$$\delta_{=0}(h_i(x)) = \begin{cases} 0 & \text{if } h_i(x) = 0, \\ +\infty & \text{else.} \end{cases} \tag{2.14}$$

Recall that the conjugate, also called the Legendre-Fenchel transform, $f^* : \mathbb{R}^n \mapsto \mathbb{R} \cup \{+\infty\}$ of a function $f : \mathbb{R}^n \mapsto \mathbb{R} \cup \{+\infty\}$ is defined as

$$f^*(y) = \sup_{x \in \mathbf{dom} f} (y^T x - f(x)). \tag{2.15}$$

We get as *conjugate of the inequality indicator function*

$$\delta_{\leq 0}^*(y) = \sup_x (y^T x - \delta_{\leq 0}(x)) = \begin{cases} 0 & \text{if } y \geq 0, \\ +\infty & \text{else} \end{cases} \tag{2.16}$$

$$= \delta_{\geq 0}(y). \tag{2.17}$$

The *bi-conjugate of the inequality indicator function* is again the original indicator function itself

$$\delta_{\leq 0}^{**}(y) = \sup_x (y^T x - \delta_{\leq 0}^*(x)) \quad (2.18)$$

$$= \sup_{x \geq 0} (y^T x) = \begin{cases} 0 & \text{if } y \leq 0, \\ +\infty & \text{else} \end{cases} \quad (2.19)$$

$$= \delta_{\leq 0}(y). \quad (2.20)$$

Accordingly, we get as *conjugate of the equality indicator function*

$$\delta_{=0}^*(y) = \sup_x (y^T x - \delta_{=0}(x)) \quad (2.21)$$

$$= 0 \quad \forall y. \quad (2.22)$$

The *bi-conjugate of the equality indicator function* again equals the original indicator function

$$\delta_{=0}^{**}(y) = \sup_x (y^T x - \delta_{=0}^*(x)) \quad (2.23)$$

$$= \sup_x (y^T x) = \begin{cases} 0 & \text{if } y = 0, \\ +\infty & \text{else} \end{cases} \quad (2.24)$$

$$= \delta_{=0}(y). \quad (2.25)$$

Now we can rewrite the constrained optimization problem (2.7) using the indicator functions of the constraints as

$$\inf_x f_0(x) + \sum_{i=1}^m \delta_{\leq 0}(f_i(x)) + \sum_{i=1}^p \delta_{=0}(h_i(x)) \quad (2.26)$$

With the bi-conjugate of the indicator functions we get

$$= \inf_x f_0(x) + \sum_{i=1}^m \delta_{\leq 0}^{**}(f_i(x)) + \sum_{i=1}^p \delta_{=0}^{**}(h_i(x)) \quad (2.27)$$

$$= \inf_x f_0(x) + \sum_{i=1}^m \sup_{\lambda \geq 0} (\lambda f_i(x)) + \sum_{i=1}^p \sup_{\mu} (\mu h_i(x))$$

We introduce individual variables λ_i and μ_i for each constraint function and arrive at the associated Lagrangian

$$= \inf_x \sup_{\lambda_i \geq 0} \sup_{\mu_i} f_0(x) + \sum_{i=1}^m \lambda_i f_i(x) + \sum_{i=1}^p \mu_i h_i(x) \quad (2.28)$$

$$= \inf_x \sup_{\lambda_i \geq 0} \sup_{\mu_i} L(x, \lambda, \mu).$$

Later in this thesis we will use this framework to solve constrained convex optimization problems with affine inequality constraints. In case of affine constraints, feasibility of a solution is already sufficient for Slater's condition and we have strong duality. In this case above result is equal to the Lagrange dual

$$= \sup_{\lambda \geq 0} \sup_{\mu} \inf_x L(x, \lambda, \mu) \quad (2.29)$$

and a feasible solution to the Lagrange dual yields an optimal solution to the primal problem.

2.5. Primal-Dual Hybrid Gradient Method

In [24] the authors generalize their algorithm for minimizing total variation regularized functionals [23, 113, 114] to general optimization problems of the structure

$$\min_{x \in X} \max_{y \in Y} G(x) + \langle Kx, y \rangle - F^*(y), \quad (2.30)$$

where X and Y are two finite-dimensional real vector spaces equipped with the inner product $\langle \cdot, \cdot \rangle$, the map $K : X \mapsto Y$ is a continuous linear operator, and $G : X \mapsto [0, +\infty)$ and $F^* : Y \mapsto [0, +\infty)$ are proper convex lower-semicontinuous functions.

The authors provide three different variants of an algorithm to solve optimization problems of this structure. The central idea of the algorithm is to iterate a gradient ascent in the primal variable and a gradient descent in the dual variable. Because F and G do not need to be smooth and differentiable, the gradient steps are evaluated using the prox operator:

The **prox**-operator of a closed proper convex lower-semicontinuous function f is defined as

$$\mathbf{prox}_{\lambda f}(v) = \arg \min_x f(x) + \frac{1}{2\lambda} \|x - v\|_2^2. \quad (2.31)$$

The first variant (Algorithm 1 in [24]) can be applied to the most general problem, the variant 2 allows accelerated convergence when either G or F^* are strongly convex, and algorithm 3 can be applied when both G and F^* are strongly convex functions. For the problems studied in this thesis strong convexity does not hold, thus here we present the variant for this most general case.

Algorithm 1 Primal Dual Hybrid Gradient method from [24]

- 1: Initialize with $x^0, y^0 \in X \times Y$ and $\bar{x}^0 = x^0$.
- 2: Iterate

$$y^{n+1} = \mathbf{prox}_{\sigma F^*}(y^n + \sigma K \bar{x}^n) \quad (2.32)$$

$$x^{n+1} = \mathbf{prox}_{\tau G}(x^n - \tau K^* y^{n+1}) \quad (2.33)$$

$$\bar{x}^{n+1} = x^{n+1} + \theta (x^{n+1} - x^n) \quad (2.34)$$

The step sizes $\tau > 0$ and $\sigma > 0$ can be chosen by a diagonal preconditioning scheme as described in [112]. In this case, one gets instead of a unique τ and σ the diagonal matrices $T = \text{diag}(\tau)$ and $\Sigma = \text{diag}(\sigma)$, with

$$\tau_j = \frac{1}{\sum_{i=1}^m K_{i,j}^{2-\alpha}}, \quad \sigma_i = \frac{1}{\sum_{j=1}^n K_{i,j}^\alpha}, \quad (2.35)$$

with $n = \dim X$ and $m = \dim Y$ for some $\alpha \in [0, 2]$.

The primal dual hybrid gradient method can be interpreted as an approximative Douglas-Rachford splitting [36] on the dual problem which is also equivalent to the alternating direction method of multipliers (ADMM) [50, 53] on the primal problem. An overview of proximal algorithms can be found in [110] and a survey about ADMM and its applications in [16].

3. Total Variation and its Minimization

With the background material on convex optimization at hand, in this chapter we focus on a particular optimization problem, the minimization of the *total variation* of a function of *bounded variation*. It turns out that we can formulate the total variation minimization problem as a convex-concave saddle point problem, that can be optimized with the primal dual splitting algorithm discussed in the end of the previous chapter. Further information on the topic, especially in the context of image analysis, can be found in the publications [23, 24, 113, 114], and the introduction by Chambolle *et al.* [22].

3.1. Definition of Total Variation

Let Ω be an open subset of \mathbb{R}^n . The *total variation* of a function $u : \Omega^n \mapsto \mathbb{R}$ is defined as

$$TV(u, \Omega) = \sup \left\{ - \int_{\Omega} u(x) \operatorname{div} \phi(x) \, dx : \phi \in C_c^\infty(\Omega, \mathbb{R}^n), |\phi(x)| \leq 1, \forall x \in \Omega \right\}, \quad (3.1)$$

where $|\phi(x)|$ is the ℓ^2 norm of the vector valued function ϕ evaluated at x and C_c^∞ is the set of arbitrarily often continuously differentiable functions with compact support.

We choose this definition of the norm to clarify that we actually evaluate the ℓ^2 norm of $\phi(x)$ point-wise on Ω . In the literature, *e.g.* [2], the constraint on ϕ is also defined as $\|\phi\|_\infty \leq 1$, which denotes the essential supremum norm of ϕ on Ω . To avoid confusion with the point-wise supremum norm, we prefer above definition instead.

Indeed, our definition $|\phi(x)| \leq 1, \forall x \in \Omega$ is equivalent to $\|\phi\|_\infty \leq 1$, which in [20] is defined as

$$\|\phi\|_\infty = \operatorname{ess\,sup}_{x \in \Omega} \left(\sum_i^n |\phi_i(x)|^2 \right)^{\frac{1}{2}} \quad (3.2)$$

This norm takes the maximum over x of the point-wise ℓ^2 norm of ϕ . It is easy to see that $\|\phi\|_\infty \leq 1$ exactly holds iff $|\phi(x)| \leq 1, \forall x \in \Omega$.

We say that a function $u : \Omega^n \mapsto \mathbb{R}$ in L^1 has *bounded variation* on Ω when $TV(u, \Omega) < +\infty$ and we write $u \in \mathcal{BV}$.

The function ϕ can be interpreted as distributional derivative of u . For a differentiable function u it follows from the divergence theorem that

$$\int_{\Omega} u(x) \operatorname{div} \phi(x) \, dx = - \int_{\Omega} \nabla u(x) \cdot \phi(x) \, dx. \quad (3.3)$$

We take the supremum over ϕ with the essential supremum norm $\|\cdot\|_\infty \leq 1$. By using operator duality we get for differentiable functions u

$$\sup_{\|\phi\|_\infty \leq 1} - \int_{\Omega} u(x) \operatorname{div} \phi(x) \, dx = \sup_{\|\phi\|_\infty \leq 1} \int_{\Omega} \nabla u(x) \cdot \phi(x) \, dx = \int_{\Omega} |\nabla u(x)| \, dx, \quad (3.4)$$

where the last equality holds in the limit when $\phi(x) \rightarrow \frac{\nabla u}{\|\nabla u\|_2}$.

3.2. Minimizing Functionals with Total Variation Regularizer as Saddle Point Problem

In the previous section we saw that the total variation of a differentiable function is defined as the supremum over ϕ . Minimizing the total variation of a differentiable function u thus leads to the saddle point problem

$$\inf_u \int_{\Omega} f(u) + |\nabla u(x)| \, dx = \inf_u \sup_{\|\phi\|_{\infty} \leq 1} \int_{\Omega} f(u) - u(x) \operatorname{div} \phi(x) \, dx. \quad (3.5)$$

On a discrete finite domain Ω and for $\mathbf{dom}(u)$ convex this problem can be solved with the primal dual optimization method introduced in Section 2.5.

3.3. Geometric Interpretation of the Total Variation

In the following we will see that minimizing the total variation has a geometric interpretation and allows to compute sets of minimal surface. First, we define an indicator function of a set.

Let $S \subseteq \Omega \subset \mathbb{R}^n$. The *indicator function* $\mathbb{1}_S : \Omega \mapsto \{0, 1\}$ of S is defined as

$$\mathbb{1}_S(x) = \begin{cases} 1 & \text{if } x \in S, \\ 0 & \text{else.} \end{cases} \quad (3.6)$$

The *perimeter* of a measurable set $S \subseteq \Omega \subset \mathbb{R}^n$ is defined as $\operatorname{Per}(S, \Omega) = \mathcal{H}^{n-1}(\partial S)$, the $(n-1)$ -dimensional Hausdorff measure $\mathcal{H}^{n-1}(\cdot)$ of the boundary ∂S of S . It is a geometric measure, *e.g.* for $n=2$ it measures the length of the curve outlining the set S , for $n=3$ it measures the surface area of the boundary surface of S .

We will see in the following section that the $(n-1)$ -dimensional Hausdorff measure of the boundary of a set is equivalent to the total variation $TV(\mathbb{1}_S)$ of the indicator function of the set. This allows to measure boundary lengths of subsets in \mathbb{R}^2 and surface areas of subsets of \mathbb{R}^3 by computing the total variation of the indicator function.

3.4. The Coarea Formula

Recall that a convex function needs to have a convex domain. The indicator function maps to the discrete domain $\{0, 1\}$, which is not a convex set. To be able to minimize the total variation with convex optimization, we therefore often define a relaxed indicator function $u : \Omega \mapsto [0, 1]$ of bounded variation, which maps to the continuous interval between 0 and 1.

A relation between the geometric measure of a perimeter and the total variation of a continuous \mathcal{BV} -function is given by the *coarea formula* [43, 45]

$$\int_{\Omega} |\nabla f(x)| \, dx = \int_{-\infty}^{\infty} TV(\mathbb{1}_{\{f>\mu\}}, \Omega) \, d\mu = \int_{-\infty}^{\infty} \operatorname{Per}(\{x : f(x) > \mu\}, \Omega) \, d\mu. \quad (3.7)$$

Thus the total variation of the continuous function u is the integral over the length of all its level lines. Note that whenever we consider functions u whose range is restricted to

an interval we have to evaluate the integral only on this interval and get

$$\int_{\Omega} |\nabla u(x)| \, dx = \int_0^1 \text{Per}(\{x : u(x) > \mu\}, \Omega) \, d\mu. \quad (3.8)$$

It follows from the definition of the perimeter and the definition of functions with bounded variation that a set has finite perimeter in Ω iff $\mathbf{1}_S \in \mathcal{BV}(\Omega)$, i.e. its indicator function has bounded variation.

3.5. Total Variation as Regularizer in Image Segmentation and 3D Reconstruction

In image segmentation, the goal is to partition an image into meaningful parts. It is one of the best studied problems in computer vision, as image segmentation is often the first step to acquire semantic information from an image. While here we focus on the two region image segmentation problem and its relaxation by Chan *et al.* [25], we want to mention recent research results that allow a convex relaxation of the multi-label image segmentation problem [54, 92, 113, 115].

Weighted partition with minimum perimeter Let $f : \Omega \mapsto \mathbb{R}$. We define the optimal weighted partition with minimum perimeter as the set $S \subseteq \Omega$ that minimizes

$$\min_{S \subseteq \Omega} \int_S f(x) \, dx + \lambda \text{Per}(S, \Omega), \quad (3.9)$$

for a given $\lambda \geq 0$. We call the set S the *foreground region* or *object* and $\Omega \setminus S$ the *background region*. Both sets S and $\Omega \setminus S$ define a partition of Ω which we call a *segmentation*. Because the function f usually depends on the image data, the first term $\int_S f(x) \, dx$ is called *data term*.

For $\lambda = 0$ above problem is easy to solve, and the optimal solution can be achieved by choosing the set $S = \{x : f(x) < 0\}$. However, in image segmentation often the data term is disturbed by noise and simple thresholding of the data term would result in an irregular set. Therefore we regularize the solution by setting $\lambda > 0$. The second term in (3.9) is also called *boundary length regularizer* and favors a smooth partition.

For $\lambda > 0$ we cannot achieve a minimum partition of (3.9) by simple thresholding of f . Therefore we formulate the minimum weighted partition problem using the convex relaxation of Chan *et al.* [25] with a relaxed indicator function $u : \Omega \mapsto [0, 1]$ of bounded variation and replace the perimeter of S with the total variation of u and get

$$\min_{u \in \mathcal{BV}(\Omega; [0,1])} \int_{\Omega} f(x)u(x) \, dx + \lambda \text{TV}(u, \Omega). \quad (3.10)$$

In Section 5.2.3 we will see that by thresholding the solution of (3.10) by choosing the upper level set $\{x : u(x) > \mu\}$ with a threshold $\mu \in [0, 1)$ we get an optimal solution of the minimum weighted partition problem (3.9).

3.6. The Shrinking Bias

The boundary length regularizer achieves good results for segmenting compact objects in practice. However, this approach fails when the object contains thin structures, as these

structures have a higher boundary length in comparison to their area than more round, compact objects.

The regularizer therefore tends to favor compact round objects, while smoothing fine detailed features of the boundary. This effect is called the *shrinking bias* which leads to a shrinking of the foreground region to minimize its boundary length.

To overcome the shrinking bias, researchers have proposed to penalize the curvature of the boundary instead of its length, *e.g.* [38, 55, 124, 125, 126]. However, because curvature is a second order measure of the boundary, this usually leads to higher order cost functions that are hard to optimize efficiently.

4. Connectedness as Topological Property

In this chapter we will give an introduction to a fundamental topological property, the connectedness of a topological space and the connectedness of graphs. We will study different properties of connectedness, with a special look on path connectedness, which is underlying the connectivity constraints developed in this thesis. The following material follows the introductory literature on topology of [90, 140], and on graph theory of [33].

4.1. Connectedness of Topological Spaces

Given X is a topological space. We say that X is *connected* if there exists no separation of X into a pair of nonempty, disjoint, open subsets $U, V \subset X$ such that $X = U \cup V$.

This is the definition of a connected *space*, in the following we will study the connectedness of *subsets* of a topological space, for which we define the following topology.

Subspace Topology [90] Let $A \subset X$ be a subset of the topological space X . The *subspace topology* \mathcal{S}_a on A is defined as

$$\mathcal{S}_a = \{U \subset A : U = A \cap V \text{ for some open subset } V \subset X\}, \quad (4.1)$$

i.e. the open subsets of \mathcal{S}_a are the intersections of the open subsets of X with A .

We call a subset A of a topological space X *connected on X* if A is connected with respect to the subspace topology \mathcal{S}_a .

4.1.1. Path Connectedness

In this section, we will introduce an easier to use sufficient condition for connectedness, the *path connectedness*. First let's consider the connectedness of mappings on a topological space.

Theorem 4.1.1. Main Theorem on Connectedness [90] *Let X, Y be topological spaces and let $f : X \mapsto Y$ be a continuous map. If X is connected, then $f(X)$ is connected.*

Proof. [90] Let $f(X)$ be not connected, then there exist two open sets $U, V \subset Y$ which intersections with $f(X)$ are nonempty and disjoint and for which $f(X) \subset U \cup V$. Lets consider the preimages of those subsets $f^{-1}(U)$ and $f^{-1}(V)$. It follows immediately that these provide a separation of X , so X is not connected. \square

Now we are able to give a definition for *path connectedness*, which is much simpler than the definition of connectedness of a space, but yet provides a sufficient condition for its connectedness.

Path Connectedness [90] Let X be a topological space and $x, x' \in X$ two points in X . A path in X from x to x' is a continuous map $C_x^{x'} : [0, 1] \mapsto X$ with $C_x^{x'}(0) = x$ and $C_x^{x'}(1) = x'$. We say that X is *path connected* if for every $p, q \in X$, there is a path in X from p to q .

An important property that we will use in the following is, that path connectedness of a topological space X implies connectedness of X .

Furthermore, path connectedness is transitive in the sense that if there is a path connecting two points a and b and there is a path connecting the points b and c , then there also exists a path connecting a and c .

This becomes obvious when we define the path $C_a^c : [0, 1] \mapsto X$ from a to c as [140]

$$C_a^c(s) = \begin{cases} C_a^b(2s), & \text{if } s \in [0, \frac{1}{2}], \\ C_b^c(2s - 1), & \text{if } s \in [\frac{1}{2}, 1], \end{cases} \quad (4.2)$$

where $C_a^b : [0, 1] \mapsto X$ is the path from a to b and $C_b^c : [0, 1] \mapsto X$ is the path from b to c .

4.1.2. Simply Connected Topological Space

There are several definitions for *simply connectedness*, we choose an intuitive definition that is based on the homotopy of paths. First we provide the definition of a homotopy in general and then define the homotopy for paths.

Homotopy [90] Let X and Y be topological spaces, and let $f, g : X \mapsto Y$ be continuous maps. A *homotopy* from f to g is a continuous map $H : X \times [0, 1] \mapsto Y$ such that

$$H(x, 0) = f(x); \quad H(x, 1) = g(x), \quad (4.3)$$

for all $x \in X$.

Now we study the homotopy of two paths:

Path Homotopy Let X be a topological space and $x, x' \in X$ two points in X . We consider two paths f and g in X from x to x' . The *path homotopy* $H : [0, 1] \times [0, 1] \mapsto X$ from f to g is a family of paths with fixed endpoints x and x' , i.e. $H(0, t) = x$ and $H(1, t) = x'$ for all $t \in [0, 1]$, that is a continuous map from f to g , i.e. $H(s, 0) = f(s)$ and $H(s, 1) = g(s)$ for all $s \in [0, 1]$. We say that f and g are *path homotopic*, if there exists a path homotopy between them, and write $f \sim g$.

This allows us to formulate the definition of a *simply connected* topological space:

We call a topological space X *simply connected* when any two paths in X with the same initial and terminal points are path homotopic.

Hence all paths with the same initial and terminal points form an equivalence class. Simply connected in this case means that there is only a single equivalence class of paths.

This allows an intuitive understanding why a simply connected subset $A \subset X$ may not contain a hole, i.e. may not enclose another subset $B \subset X$ which is not in A . In this case no continuous mapping between any two paths "on different sides of B " exists that does not leave A .

4.2. Connectedness of a Graph

While the previous section considered continuous topological spaces, in this section we provide definitions to work on discrete graphs as topological spaces. We follow the notation and definitions in [33].

A graph contains of a set of vertices V and edges $E \subset V \times V$. We denote the vertex set of G with $V(G)$ and the edge set of G with $E(G)$. We call a vertex *incident* with an edge e if $v \in e$. The edges incident to a vertex v define a local neighborhood of *adjacent vertices* or *neighbors* of v . Two vertices i and j are *adjacent*, when there exists an edge $ij \in E$. The number of adjacent vertices is the *degree* of a vertex.

Let $G = (V, E)$ and $G' = (V', E')$ be two graphs. If $V(G') \subset V(G)$ and $E(G') \subset E(G)$, then we call G' a *subgraph* of G , and write $G' \subset G$.

If the subgraph $G' \subset G$ contains all edges in E with both endpoints in V' , i.e. all $ij \in E(G)$ for $i, j \in V[G']$, then we call G' an *induced subgraph* of G . We say that the set V' *induces* the subgraph G' in G , and denote the induced subgraph with $G' =: G[V']$. Thus any set of vertices $U \subset V$ induces a subgraph $G[U]$, which edges are those edges of G with both endpoints in U .

We define a *path in a graph* G as a non-empty graph $P = (V_p, E_p)$ with $V_p \subset V(G)$ and $E_p \subset E(G)$ and

$$V_p = \{x_0, x_1, \dots, x_k\} \quad E = x_0x_1, x_1x_2, \dots, x_{k-1}x_k \quad (4.4)$$

where all x_i are distinct from other. We call the vertices x_0 and x_k *linked* by P .

Let the graph $P = x_0 \dots x_{k-1}$ be a path with $k \geq 3$, then we call the graph $C := P \cup x_{k-1}x_0$, i.e. a path where both ends are connected, a *cycle*.

A connected *acyclic* graph, which does not contain any cycles, is called a *tree*. Vertices of degree 1 in a tree are called *leaves* or *leave vertices*. Furthermore, any interior vertex, i.e. a vertex which is not a leaf, of a tree has a degree of at least 2.

We can now define the property of *connectedness* for a graph [33], which reminds us of the definition of path-connectedness of a topological space.

A non-empty graph G is called *connected* if any two of its vertices are linked by a path in G . If the induced subgraph $G[U]$ of a subset $U \subset V(G)$ is connected, we also call U itself connected in G .

4.2.1. k-Connected Graph

We will use a special type of connectedness of graphs, the *k-connectedness*, sometimes called *k-vertex-connectedness*.

A graph $G = (V, E)$ is called *k-connected* for $k \in \mathbb{N}$ if $|V| > k$ and $G[V \setminus X]$ is connected for every set $X \subseteq V$ with $|X| < k$. Thus, G is connected when less than k vertices are removed from its vertex set. In case G is *2-connected*, we also call G *biconnected*. The greatest integer k for which G is k -connected is the *connectivity* of G .

In this thesis, the term *connectivity constraint* refers to a constraint which imposes connectedness in image partition problems by requiring a certain connectivity of a subgraph induced by the partition, thus sometimes we use the terms connectivity and connectedness synonymously. First, we describe a constraint on a tree which preserves the connectivity of 1 for the tree. In Chapter 8 we extend this constraint to loop preserving constraints,

which are defined on a biconnected graph. Thus we use the terms *1-connectivity constraint* and *2-connectivity constraint* respectively.

In this chapter we provided definitions of connectedness as a topological property of a continuous space and on the discrete topology of a graph. This chapter also concludes the introductory material. In the following we will see how the mathematical tools described so far can be used to solve image partition problems with the constraint, that the foreground partition is connected.

Part II.

Image Segmentation

5. Connectivity Constraints for the Segmentation of 2D and 3D Images

In this chapter, we present one of the first practicable methods to include connectivity constraints into image segmentation and 3D reconstruction. We propose to reformulate the connectivity constraint along geodesics, which in the discrete domain results in a fixed topology of a discrete graph, in this case a geodesic shortest path tree. While solving the original problem is NP-hard, the reformulated problem can be efficiently solved to global optimality. We show how a-priori information about the geometry of the structure of interest can be included when constructing the shortest path tree. To solve the resulting labeling problem, we generalize a recent primal-dual algorithm for continuous convex optimization to an arbitrary graph. Part of the results presented in this chapter have been published in [139], here we extend this work by a proof of the thresholding theorem for the image segmentation model with connectivity constraint.

The chapter is organized as follows: first, we give an overview on related work on topological constraints in image segmentation. Then we describe how the geodesic shortest path tree is constructed with a distance measure that is related to the image data and the bending energy of each path in the tree. We show how to formulate a global connectivity prior as a local constraint on this tree. The connectivity constraint results in a linear constraint on the labeling function and thus preserves convexity of the image segmentation problem. This allows to compute a globally optimal solution. In the end of the chapter we present results on data from medical imaging in angiography, retinal blood vessel segmentation and user interactive image segmentation.

5.1. Introduction

The task of image segmentation, the separation of an image into meaningful parts, is one of the most important and well studied problems in image processing and computer vision. While state-of-the art segmentation methods [18, 59, 147] perform well for segmenting compact objects, their performance on thin and elongated structures is often not satisfying. The commonly used length regularizer suppresses small structures and the correct topology cannot be reconstructed.

To overcome this shrinking bias, recently two different approaches have been suggested in the literature. First, curvature based measures have attracted the interest of researchers in computer vision to include them in image segmentation frameworks [38, 55, 126]. However, introducing these regularizers into segmentation algorithms lead to higher order cost functions, which are hard to optimize.

Another way to preserve thin structures is to use topological constraints. A special subclass of these constraints are connectivity constraints, which ensure the connectedness of a labeled region and therefore allow that thin connections between foreground regions are preserved in the final segmentation result. To overcome the limitation of topology preserving level set methods [63], that only locally optimal solutions can be achieved,

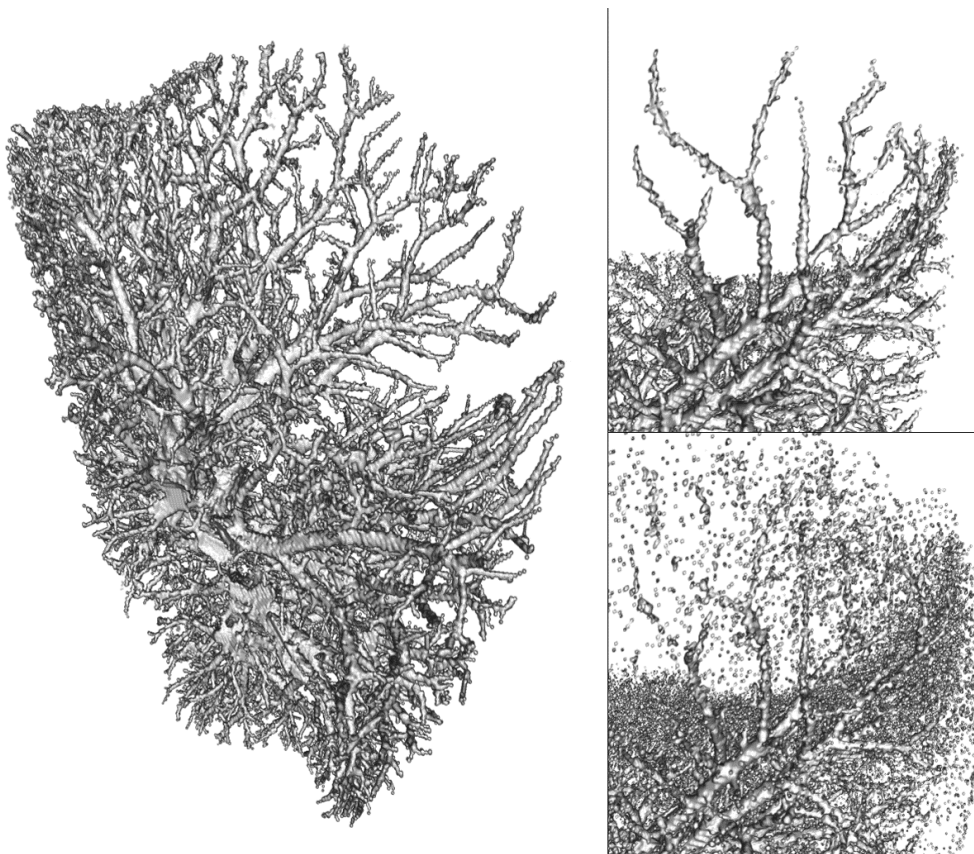


Figure 5.1.: By modeling the object of interest as a connected tree, the method is well suited for medical image segmentation tasks, in this case the segmentation of a blood vessel tree in angiography. Left image and top right: Lung vessel tree segmented with the proposed method. Bottom right: Segmentation result without connectivity constraint.

recent approaches include topological constraints in random field models [27, 104, 150]. So far, these methods only allow to compute an approximate solution of the global optimization problem.

5.1.1. Related Work

Topology preserving constraints have been recently proposed for different algorithmic frameworks. For the graph cut [19] framework, Zeng *et al.* [160] present an extension, that allows to preserve the topology of the result with respect to an initial segmentation. Beginning on a coarse scale, their method preserves the topology of the initial segmentation during refinement. A similar approach was proposed by Han *et al.* [63] for the level set framework. The drawback of both methods is that they depend on the initialization and therefore only reach a local optimum.

Vicente *et al.* [150] introduce a connectivity prior into interactive segmentation in a Markov random field framework and enforce connectivity to user given seed points. The authors show that the original problem is NP-hard and propose a greedy approximation scheme consisting of a Dijkstra algorithm where in every expansion step a graph cut needs to be solved. Their method also only reaches a local optimum.

Chen *et al.* [27] propose to alternately solve a graph cut and modify the unary terms based on a level-set representation until predefined topological constraints are fulfilled. However, they do not find minimal connections, for which the integral along the curve is minimized, instead they minimize the value of the maximum penalty along the curve which can lead to undesired results if this penalty is very high, as the path cost does not depend on the values of the data term at other positions than the maximum. Furthermore, the runtime complexity of this method prevents to use it for large scale problems.

Recently, methods that aim to reach a global optimum were proposed by different authors. First, Nowozin and Lampert [104] propose to formulate the image segmentation problem with topological constraints as a linear program relaxation. However, even for small image sizes the runtime complexity of the method does not scale well and the relaxation is not tight. In contrast to the method presented in this publication, their method is not suitable for large scale problems in 3D segmentation.

In a recent study, Rempfler *et al.* [117] propose a specifically adapted constraint generation scheme to solve the underlying discrete optimization problem, the minimum cost connected subgraph (MCCS) problem, in an integer linear programming framework. The reported median runtime of 500 s on images of the DRIVE benchmark prevents to use their method in practice, but the results can serve as ground truth solution for the benchmark. They compared their exact results with the results obtained with the geodesic shortest path method proposed in this chapter, and found no statistical significant difference between both methods. Further details on the comparison are described in the experimental section below.

Gulshan *et al.* [61] introduce a geodesic star shape prior into the graph-cut framework. The solution of the segmentation is restricted to the shape of a geodesic star around an input seed, while the geodesic distance depends on the image gradient. If multiple input seeds are given, the foreground segment takes the form of a geodesic forest, the union of the geodesic stars for every seed. A drawback of their method is that because they solve for the boundary length regularizer using the graph-cut framework their method is affected by a metrication error that depends on the discretization of the pixel neighborhood.

One application field of methods that preserve thin structures is in angiography, where the object of interest that should be segmented are blood vessels. Some of the most prominent existing methods for this special task are based on geodesic shortest paths. By using a local anisotropic metric and modeling the segmentation task as a path search problem with varying radius, of circles for 2D images [10] and spheres for 3D data [9], such methods are well suited for the special case of tubular structures like blood vessels, but at the same time are restricted to this specific task. Instead of modeling the objects that should be segmented explicitly as connected paths some authors propose to first pre-process the image data with filters that show a strong response in areas where elongated structures are present [47, 84]. In the recent work of Bauer *et al.* [8] a similar approach leads to an explicit model of short tubular segments that are in a second step connected to a whole tree of branching tubular structures. Therefore a connection confidence measure to join adjacent tube segments is defined, that depends on the distance and joining angle of the segments. The resulting minimization problem is solved by using the graph cut algorithm [19]. For a review on recent work in the particular application domain of blood vessel segmentation see [93].

Instead of optimizing over the boundary as proposed by Kass *et al.* [76] or using a level set formulation [26, 63], we introduce our connectivity constraints for the convex image segmentation framework of Chan *et al.* [25]. This has the benefit that, because the constraint can be formulated as linear constraints, the whole image segmentation problem with connectivity constraints remains a convex optimization problem, and thus allows to be solved to global optimality. In comparison to image segmentation methods that are based on the graph cut framework [19, 27], our methods does not suffer from discretization artifacts and instead measures the Euclidean norm of the boundary length.

5.1.2. Problem Formulation

Given an image I with the domain Ω , a bounded connected subset of \mathbb{R}^m , we wish to solve the constrained optimization problem

$$\begin{aligned} \min_{l: \Omega \mapsto \{0,1\}} \quad & \int_{\Omega} f(x) l(x) \, dx + \lambda \operatorname{Per}(\Sigma_l, \Omega) & (5.1) \\ \text{s.t.} \quad & \forall x, x' \in \Sigma_l : \exists C_x^{x'}, \forall t \in [0, 1], C_x^{x'}(t) \in \Sigma_l, & (C0) \end{aligned}$$

where $\Sigma_l \subseteq \Omega$ is the foreground segment, the part of the image which is labeled by the labeling function $l : \Omega \mapsto \{0, 1\}$ with the label 1,

$$\Sigma_l = \{x \in \Omega : l(x) = 1\}. \quad (5.2)$$

We assume that we are given a probabilistic model for every $x \in \Omega$, i.e. pixel of a 2D image or voxel of a 3D image, that depends on the image data and describes the likelihood for foreground and background

$$f(x) = \log \left(\frac{P(I(x)|l(x) = 0)}{P(I(x)|l(x) = 1)} \right), \quad (5.3)$$

where $P(I(x)|l(x) = 1)$ describes the probability of x being in the foreground region and $P(I(x)|l(x) = 0)$ of x being in the background respectively. The second term $\operatorname{Per}(\Sigma_l, \Omega)$ is the perimeter of the foreground segment Σ_l , the $m - 1$ dimensional Hausdorff measure of its boundary, details can be found in the introduction in Section 3.3. With $C_x^{x'}$ we formalize a connected trajectory from x to x' as a continuous function $C_x^{x'} : [0, 1] \mapsto \Sigma_l$ with $C_x^{x'}(0) = x$ and $C_x^{x'}(1) = x'$.

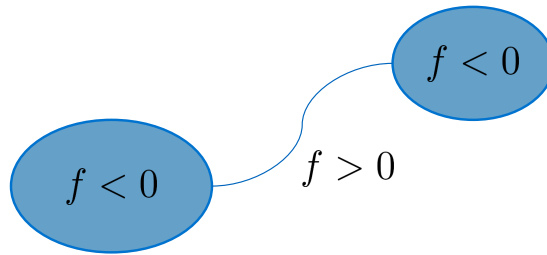


Figure 5.2.: Without the boundary length regularizer ($\lambda = 0$), the foreground segment is defined by the sign of the data term f . Obviously, in this case it holds for the data term f along the path connecting two unconnected parts of the foreground that $f > 0$.

The solution of the optimization problem should satisfy the connectivity constraint (C0):

For each pair of points $x, x' \in \Omega$ that belong to the foreground Σ_l there must exist a connected path from x to x' such that all $p \in C_{x'}^x \subset \Omega$ in the path between x and x' belong to the foreground.

This constraint is equivalent to the definition of *path connectedness* (Section 4.1.1) of Σ_l and ensures that the foreground segment is connected. Unfortunately even for the special case $\lambda = 0$, minimizing Eq. (5.1) with (C0) is NP-hard because the minimum Steiner tree problem can be reduced to this problem [150]. We will see in the following, how to reformulate the problem such that it becomes feasible to solve.

5.2. The Continuous Case: Connectivity Along Geodesics

To approximate a solution to Eq. (5.1) we propose to reformulate the connectivity constraint along the geodesics from each point $x \in \Sigma_l$ inside the foreground segment to a specific point $s \in \Sigma_l$ inside the foreground segment. In general, we call the connectivity requirement along geodesics *g-connectivity*, and here study the special case that these geodesics pass through the point $s \in \Sigma_l$, which we call *rooted g-connectivity*. The point s takes the role of a *root*, from which all the geodesics originate from, and specifying s and the local metric tensor g uniquely defines the topology of the geodesics.

5.2.1. An Image Depending Geodesic Topology

The geodesic shortest path topology is inspired by image segmentation methods based on geodesic distances, that depend on an image depending local metric. Such approaches have been successfully applied to medical image segmentation [9] as well as general image segmentation [5, 29]. In this context, we will show how to define this image depending local metric and how to additionally incorporate a-priori knowledge about the geometry of the object of interest.

First we have to choose an appropriate local metric. We propose to use the non negative cost function $f^+ = \max(0, f(x))$. This is motivated by the following: Lets consider the special case $\lambda = 0$, then the labeling function $l(x)$ takes on the value 1 for $f(x) < 0$ and 0 for $f(x) > 0$. We leave out the special case $f(x) = 0$ as it does not occur in practice. For all $x_p \in \Omega$ that do not belong to the foreground but need to be added to the foreground to satisfy the connectivity constraint obviously $l(x_p) = 0$ and therefore $f(x_p) \geq 0$. This is also illustrated in Fig. 5.2. The optimal cost of the connecting path between a fixed s

and any x in the region that should be connected on \mathcal{G}_s is then given by

$$\bar{C}_s^x = \min_{C_s^x} \int_0^1 f^+(C(t)) dt, \quad (5.4)$$

which motivates our choice of f^+ as image depending metric.

5.2.2. Connectivity Constraint as Monotonicity Constraint

We formalize the segmentation model with rooted g-connectivity constraint as

$$\min_{l: \Omega \mapsto \{0,1\}} \int_{\Omega} f(x) l(x) dx + \lambda \text{Per}(\Sigma_l, \Omega) \quad (\text{P1})$$

$$\text{s.t.} \quad \forall x \in \Sigma_l : \exists \bar{C}_s^x \in \mathcal{G}_s, \forall t \in [0, 1], \bar{C}_s^x(t) \in \Sigma_l, \quad (\text{C1})$$

where \mathcal{G}_s is the set of all geodesics through s and \bar{C}_s^x is the geodesic from s to x .

In contrast to the original image segmentation problem, we will show in the following that this constraint can be introduced as a linear constraint in a convex optimization framework and therefore allows the computation of an optimal solution.

We follow the convex relaxation approach of Chan *et al.* [25] and relax the discrete labeling function $l : \Omega \mapsto \{0, 1\}$ by introducing a continuously differentiable function $u : \Omega \mapsto [0, 1]$ of bounded variation. The perimeter of the foreground region is replaced by the *total variation* of the continuous labeling function. Further details on the relation between the total variation and the perimeter of a set are given in the introduction in Section 3.3. Now the connectivity constraint can be expressed as constraint on the directional derivative of u along a geodesic.

$$\min_{u: \Omega \mapsto [0,1]} \int_{\Omega} f(x) u(x) + \lambda |\nabla u| dx \quad (\text{P2})$$

$$\text{s.t.} \quad \forall x \in \Omega, \exists \bar{C}_s^x \in \mathcal{G}_s, \nabla_{\bar{C}_s^x} u(t) \leq 0, t \in [0, 1] \quad (\text{C2})$$

where $\nabla_{\bar{C}_s^x} u(t)$ is the directional derivative of u at t along the geodesic \bar{C}_s^x , in the direction of increasing distance from s , defined as

$$\nabla_{\bar{C}_s^x} u(t) = \lim_{h \rightarrow 0} \frac{u(\bar{C}_s^x(t+h)) - u(\bar{C}_s^x(t))}{h}. \quad (5.5)$$

In fact, we can solve the discrete labeling problem by computing a thresholded solution of the problem with continuous co-domain. A proof for this relation is given in the following section.

5.2.3. The Thresholding Theorem

In the following we show that every thresholded version of the optimal solution of the relaxed optimization problem (P2) provides a minimizer for the original binary labeling problem (P1). We show *optimality* of the thresholded version using the thresholding theorem of [25], which holds for almost every threshold and was extended to hold for every threshold by [12]. What is left to show is *feasibility* of the thresholded version: that every continuous solution which is feasible regarding the connectivity constraints in (P2) is connected in the discrete case of (P1).

First we reproduce the more concise version of the proof of Chan *et al.* that appeared in [81]. We consider the image segmentation problem without connectivity constraints and formulate the functional of the labeling problem with discrete indicator function $l : \Omega \mapsto \{0, 1\}$ as

$$\hat{E}(l) = \int_{\Omega} f(x) l(x) \, dx + \lambda \operatorname{Per}(\Sigma_l, \Omega). \quad (5.6)$$

We introduce a continuously differentiable function $u : \Omega \mapsto [0, 1]$ of bounded variation and replace the perimeter with the total variation of u .

$$E(u) = \int_{\Omega} f(x) u(x) + \lambda |\nabla u| \, dx \quad (5.7)$$

The thresholding theorem now states the following:

Theorem 5.2.1. [81] *Let $u^* : \mathbb{R}^n \mapsto [0, 1]$ be a global minimizer of (5.7). Then the upper level sets of u^**

$$\Sigma_{\{u^* > \mu\}} = \{x \in \mathbb{R}^n \mid u^*(x) > \mu\}, \quad \mu \in (0, 1), \quad (5.8)$$

thresholded at μ , are minimizers of the original binary labeling problem (5.6), for almost every threshold μ .

Proof. [81] We use the layer cake representation of the function $u^* : \mathbb{R}^n \mapsto [0, 1]$:

$$u^*(x) = \int_0^1 \mathbb{1}_{\{u^* > \mu\}}(x) \, d\mu, \quad (5.9)$$

and rewrite the first term in the functional (5.7) as

$$\int_{\mathbb{R}^n} f u^* \, dx = \int_{\mathbb{R}^n} f \left(\int_0^1 \mathbb{1}_{\{u^* > \mu\}} \, d\mu \right) \, dx = \int_0^1 \int_{\Sigma_{\{u^* > \mu\}}} f(x) \, dx \, d\mu. \quad (5.10)$$

The functional (5.7) then can be written as

$$E(u^*) = \int_0^1 \left\{ \int_{\Sigma_{\{u^* > \mu\}}} f(x) \, dx + \left| \partial \Sigma_{\{u^* > \mu\}} \right| \right\} \, d\mu \equiv \int_0^1 \hat{E}(\Sigma_{\{u^* > \mu\}}) \, d\mu, \quad (5.11)$$

where the total variation norm in (5.7) is written as the integral over the length of all level lines of u by using the coarea formula (see Section 3.4)

$$\int_{\Omega} |\nabla u(x)| \, dx = \int_{-\infty}^{\infty} \mathcal{H}_{n-1}(u^{-1}(t)) \, dt. \quad (5.12)$$

We see that the functional (5.11) can be expressed as an integral of the original binary labeling problem \hat{E} evaluated on the upper level sets of u^* .

Assume that theorem 5.2.1 does not hold for some threshold value $\tilde{\mu} \in (0, 1)$, i.e. there exists a minimizer Σ^* of the binary labeling problem with smaller energy

$$\hat{E}(\Sigma^*) < \hat{E}(\Sigma_{\tilde{\mu}, u^*}). \quad (5.13)$$

Then for the indicator function $\mathbb{1}_{\Sigma^*}$ of the set Σ^* we get

$$E(\mathbb{1}_{\Sigma^*}) = \int_0^1 \hat{E}(\Sigma^*) \, d\mu < \int_0^1 \hat{E}(\Sigma_{\{u^* > \mu\}}) \, d\mu = E(u^*), \quad (5.14)$$

which contradicts the assumption that u^* was a global minimizer of (5.7). \square

We now show that every thresholded version of a feasible minimizer of u^* (P2) is a feasible minimizer of (P1):

Theorem 5.2.2. *Let $u^* : \mathbb{R}^n \mapsto [0, 1]$ be a global minimizer of (P2) that is feasible with respect to the constraints (C2). Then all upper level sets, i.e. the thresholded versions*

$$\Sigma_{\{u^* > \mu\}} = \{x \in \mathbb{R}^n \mid u^*(x) > \mu\}, \quad \mu \in (0, 1), \quad (5.15)$$

of u^ are minimizers of the original binary labeling problem (P1), are connected and thus feasible with respect to the constraint (C1).*

Proof. Optimality of a thresholded version of a minimizer of (P2) for the binary labeling problem (P1) follows from Theorem 5.2.1. What is left to show is feasibility of the thresholded solution with respect to (C1). We show this by contradiction.

Let u^* be feasible with respect to (C2). Let's assume that the constraint (C1) does not hold, i.e. there exists an $x \in \Sigma_{\{u^* > \mu\}}$, thus $u^*(x) > \mu$ for some μ , and we have a geodesic $\bar{C}_s^x \in \mathcal{G}_s$ with $\bar{C}_s^x(0) = s$ and $\bar{C}_s^x(1) = x$ for which it does not hold for all $t \in [0, 1]$ that $\bar{C}_s^x(t) \in \Sigma_{\{u^* > \mu\}}$, i.e. it exists a $t^* \in [0, 1)$ for which $u^*(\bar{C}_s^x(t^*)) \leq \mu$.

But it holds that

$$u^*(x) = u^*(\bar{C}_s^x(1)) > \mu,$$

and thus

$$u^*(\bar{C}_s^x(1)) > u^*(\bar{C}_s^x(t^*)),$$

for some $0 \leq t^* < 1$ which violates the monotonicity constraint (C2) along \bar{C}_s^x . This concludes the proof. \square

We therefore have shown that by thresholding a feasible minimizer of the continuous optimization problem (C2) we obtain a binary solution of the original binary labeling problem which is optimal and feasible with respect to the original discrete optimization problem (C1).

5.3. Image Segmentation on the Discrete Domain of a Weighted Graph

Before we can solve the optimization problem numerically, we have to find a suitable discretization of the domain. Often, the image segmentation problem with total variation regularizer is discretized on the image grid, and the gradient and the divergence operator are realized using finite differences. Another common approach is to interpret the pixel grid as a graph, with a vertex for every pixel coordinate $x \in \Omega$.

A well known approach for image segmentation on the discrete domain of a graph is the graph-cut framework [19]. In this framework, the optimal subset with minimum boundary length problem is solved by computing a minimum cut through a discrete graph, which is equivalent to computing a maximum flow through the graph, a duality given by the max-flow min-cut theorem [39, 46]. Modern efficient algorithms exist to compute this maximum flow [18], which has led to a widespread application of the min-cut framework. However, a major drawback of this approach is that the boundary length is measured as a discretized quantity: it amounts to the sum of the weights of edges belonging to the cut, which results in a metrication error and leads to discretization artifacts.

When using the total variation regularizer, this metrication error can be avoided: as discussed in the introduction in Section 3.3, the total variation of the labeling function measures the accumulated Euclidean boundary length of the function's level lines. Here, we show instead how to define a regularizer on a discrete graph that is equivalent to the total variation regularizer. This allows, as shown in the following section, to also formulate the connectivity constraint on this discrete graph. First, we define the corresponding operators on a discrete graph and derive a *local variation* regularized segmentation model as theoretically sound equivalent to the continuous *total variation* model. As a consequence, the labeling problem on the weighted graph can be solved efficiently using a recent algorithm for continuous convex optimization [24]. We validate via experiments that, when choosing the ℓ^2 vector norm for the dual variable, the proposed method does not suffer the metrication artifacts of the graph cut framework. Furthermore we show that the metrication errors of the graph-cut framework can be reproduced when taking the ℓ^∞ norm of the dual variable.

5.3.1. Gradient and Divergence Operators on Weighted Graphs

Let $G = (V, E, W)$ be a graph with the set of vertices V with $|V| = n$, a set of edges $E \subset V \times V$ and a positive $n \times n$ weight matrix W that assigns a weight to every edge of the graph. We define the gradient and divergence operators on the graph following [66] and [15, 40]. Let $f : V \mapsto \mathbb{R}$ be a function of $\mathcal{H}(V)$, the Hilbert space of real-valued functions on the vertices of G that is equipped with the inner product $\langle f, g \rangle_{\mathcal{H}(V)} = \sum_{v \in V} f(v)g(v)$. We define the *difference operator* $d : \mathcal{H}(V) \mapsto \mathcal{H}(E)$ of f on an edge $(i, j) \in E$ as

$$(df)(e_{ij}) = \sqrt{w_{ij}}(f(j) - f(i)). \quad (5.16)$$

This difference operator can be interpreted as the *directional derivative* $\partial_i f_j := (df)(e_{ij})$ of a function f at a vertex i along the edge to vertex j .

The *weighted gradient operator* is the vector operator $\nabla_i f = (\partial_i f_j : (i, j) \in E)^T$. The ℓ_2 norm of this vector is the *local variation* of f at v

$$|\nabla_i f| := \sqrt{\sum_{ij \in E} (\partial_i f_j)^2} \quad (5.17)$$

$$= \sqrt{\sum_{ij \in E} w_{ij}(f_j - f_i)^2} \quad (5.18)$$

Equivalently, let $p : E \mapsto \mathbb{R}$ be a function of $\mathcal{H}(E)$, the Hilbert space of real-valued functions on the edges of G , that is equipped with the inner product $\langle f, g \rangle_{\mathcal{H}(E)} = \sum_{(i,j) \in E} f(i, j)g(i, j)$. The *adjoint* $d^* : \mathcal{H}(E) \mapsto \mathcal{H}(V)$ of the difference operator is given by

$$\langle df, p \rangle_{\mathcal{H}(E)} = \langle f, d^*p \rangle_{\mathcal{H}(V)}. \quad (5.19)$$

Following the definitions of the inner products, the *divergence operator* of p at a node i is

$$\text{div}_i p = -d^*(p)_i \quad (5.20)$$

$$= \sum_{ji \in E} \sqrt{w_{ji}}p_{ji} - \sum_{ij \in E} \sqrt{w_{ij}}p_{ij}. \quad (5.21)$$

With the directional derivative, the gradient, and the divergence operator, we have all required operators to formulate the total variation regularized image segmentation model on a weighted graph.

5.3.2. The Segmentation Model in the Weighted Graph Framework

In this section we derive our image segmentation algorithm in the weighted graph framework, which results in a highly adaptive and expressive model similar to the non-local TV model proposed by Gilboa and Osher [52].

In the following we denote with $u : V \mapsto [0, 1]$ the relaxed labeling function which assigns a value to every vertex, thus u is a function of $\mathcal{H}(V)$. With $f : V \mapsto \mathbb{R}$ we denote the term that depends on the conditional probabilities for foreground and background at every vertex, defined as $f(i) = -\log P_{\mathcal{F}}(x_i) + \log P_{\mathcal{B}}(x_i)$. As a short hand we write f_i for the value of f at a vertex i , and u_i for the value of u at a vertex i . The dual function $p : E \mapsto \mathbb{R}$ is defined over the edges of the graph and belongs to $\mathcal{H}(E)$. As a shorthand we write p_{ij} for the value of p on the edge ij . Also, we will use the notation x_i to refer to the position $x_i \in \Omega$ associated to the vertex i in the graph.

Given above definitions, we are able to formulate an image segmentation model with *local variation regularization* on a weighted graph

$$\min_{u:V \mapsto [0,1]} \sum_{i \in V} \left\{ f_i u_i + \lambda |\nabla_i u| \right\}. \quad (5.22)$$

By comparing this term with the definition of the local variation Eq. (5.18) we observe that the weight of the regularizer $\lambda \in \mathbb{R}^+$ corresponds to taking the edge weight $w_{ij} = \lambda^2$ for every edge $ij \in E$.

Taking different weights w_{ij} allows to define a local metric that measures the boundary length. How those weights are chosen strongly depends on the application, *e.g.* in image segmentation one can choose weights that depend on the gradient of the image to favor object boundaries at strong image gradients. Furthermore, the presented framework can be used to process 2-manifolds represented as discrete meshes. In [15, 40] the authors propose to apply the framework for surface denoising by smoothing over the vertex coordinates in \mathbb{R}^3 .

5.3.3. A Primal-Dual Method for Vertex Labeling

The definition of the weighted gradient and weighted divergence operators allows to formulate Eq. (5.22) as *saddle-point problem* on a weighted graph

$$\min_u \max_p \langle f, u \rangle_{\mathcal{H}(V)} + \langle u, \operatorname{div} p \rangle_{\mathcal{H}(V)} \quad (5.23)$$

$$\text{s.t.} \quad \forall i \in V, u_i \in [0, 1], |p_i| \leq 1, \quad (5.24)$$

where $|p_i|$ is the ℓ_2 norm of p defined over the edges incident with the vertex i

$$|p_i| = \sqrt{\sum_{ij \in E} p_{ij}^2}. \quad (5.25)$$

The update equations for the segmentation problem on a weighted graph can be derived following [24, 114]. As described in the introduction in section Section 2.5, the update steps in Algorithm 1 in [24] are computed using the **prox**-operator, which for a proper convex lower-semicontinuous function f is defined as

$$\mathbf{prox}_{\lambda F}(v) = \arg \min_x F(x) + \frac{1}{2\lambda} \|x - v\|_2^2. \quad (5.26)$$

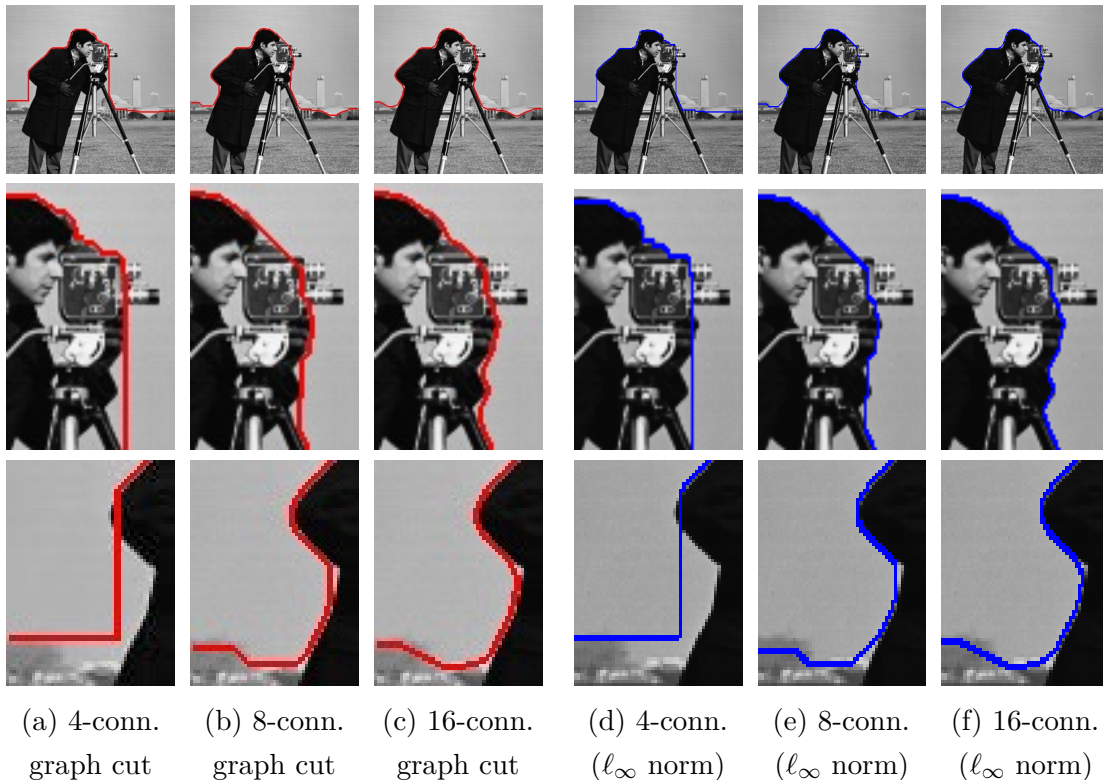


Figure 5.3.: The use of the ℓ_∞ norm for the dual variable p results in metrication artifacts similar to those of the graph-cut algorithm. *Graph cut results reprinted from [80] with kind permission of Maria Klodt.*

For our optimization problem, the **prox**-operator can be decomposed for the values of u_i for each vertex $i \in V$ and for the values of p_{ij} for each edge $ij \in E$. Because of operator duality of ∇_i and div_i , the update equations are given by

$$\begin{aligned} p_{ij}^{k+1} &= \mathbf{prox}_{\sigma F^*} \left(p_{ij}^k + \sigma \partial_i \bar{u}_j^k \right) \\ u_i^{k+1} &= \mathbf{prox}_{\tau G} \left(u_i^k + \tau \text{div}_i p^{k+1} \right) \\ \bar{u}_i^{k+1} &= u_i^{k+1} + \theta \left(u_i^{k+1} - u_i^k \right). \end{aligned} \quad (5.27)$$

With $F^*(p) = \delta_{\leq 1}(|p_i|)$, the indicator function of the unit ball constraints on p , and $G(u_i) = f_i u_i$, the image based data term, we evaluate the **prox**-operators in closed form and get the update equations

$$\begin{aligned} p_{ij}^{k+1} &= \pi_{|p_i| \leq 1} \left(p_{ij}^k + \sigma \partial_i \bar{u}_j^k \right) \\ u_i^{k+1} &= u_i^k + \tau \text{div}_i p^{k+1} - \tau f_i \\ \bar{u}_i^{k+1} &= u_i^{k+1} + \theta \left(u_i^{k+1} - u_i^k \right), \end{aligned} \quad (5.28)$$

with step sizes τ and σ , that are determined using the diagonal precondition method described in [112]. The projection $\pi_{|p_i| \leq 1}(\cdot)$ projects the values of p_{ij}^{k+1} onto the unit ball defined over the edges $ij \in E$ incident to $i \in V$ such that constraint (5.25) is fulfilled.

5.3.4. Comparison of the Primal Dual Algorithm on a Graph and the Graph-Cut Framework

In the previous section, we have shown how to discretize a model for image segmentation with a total variation regularizer on the discrete domain of a graph. As norm over the dual variable of all edges incident to a vertex we define the ℓ^2 norm in Eq. (5.25). The choice of the ℓ^2 norm follows from the definition of the total variation (see Section 3.1). As shown with the co-area formula, this allows to measure the Euclidean length of the level lines of u , which is a major advantage in comparison to the graph-cut framework, that is affected by metrication errors. Those metrication errors originate from the discrete nature of how the boundary length is defined in the discrete graph-cut framework: the boundary of a set is measured by computing the weight of a cut through the weighted graph, which is the sum of the weights of edges belonging to the cut.

Here we will show that by choosing a different norm for the dual variable p , we can reproduce the metrication artifacts that occur when using the graph-cut framework. In the graph-cut framework, the discrete representation of the boundary by measuring the sum over all edges belonging to a cut corresponds to measuring the ℓ_1 norm of the gradient of the labeling function. The dual of the ℓ_1 norm is the ℓ_∞ norm, also called essential supremum norm. We apply the essential supremum norm on the dual variable p_i , defined as

$$\|p_i\|_\infty = \max_{ij \in E} |p_{ij}|. \quad (5.29)$$

Thus the constraint $\|p_i\|_\infty \leq 1$ results in a point-wise projection of the values of p_{ij} onto the interval $[-1, +1]$ independently for every edge. As depicted in Fig. 5.3 the constraint on p_i with this ℓ_∞ norm results in metrication artifacts similar to those of the graph-cut framework.

A comparison of segmentation results for the ℓ_2 and the ℓ_∞ norm is provided in Fig. 5.4. Like in the graph-cut framework, the metrication error of the model with the ℓ_∞ norm can be reduced by extending the neighborhood of the grid. However, for the model with the ℓ_2 norm extending the neighborhood has no effect: the Euclidean length of the boundary is already correctly measured on a 4-grid.

5.4. The Connectivity Constraint on a Discrete Domain

In this section, we describe how the connectivity constraint along geodesics can be formulated on a discrete domain. First we introduce shortest paths as the equivalent to geodesics on the discrete domain. The shortest paths form a directed graph, the shortest path tree, and we show how the connectivity constraint, a monotonicity constraint along the shortest paths, can be formulated on this tree.

5.4.1. Discrete Geodesics

Shortest Path Tree On the discrete graph, a geodesic from the root s to a point x amounts to the shortest path between s and x . The edges of all those shortest paths originating in s form a tree which is rooted in s . Because we want to compute shortest paths in the graph that are equivalent to the geodesics in the continuous domain described in Section 5.2.1, we compute shortest paths in the metric defined by the positive part of the data term f^+ . Further details are given below.

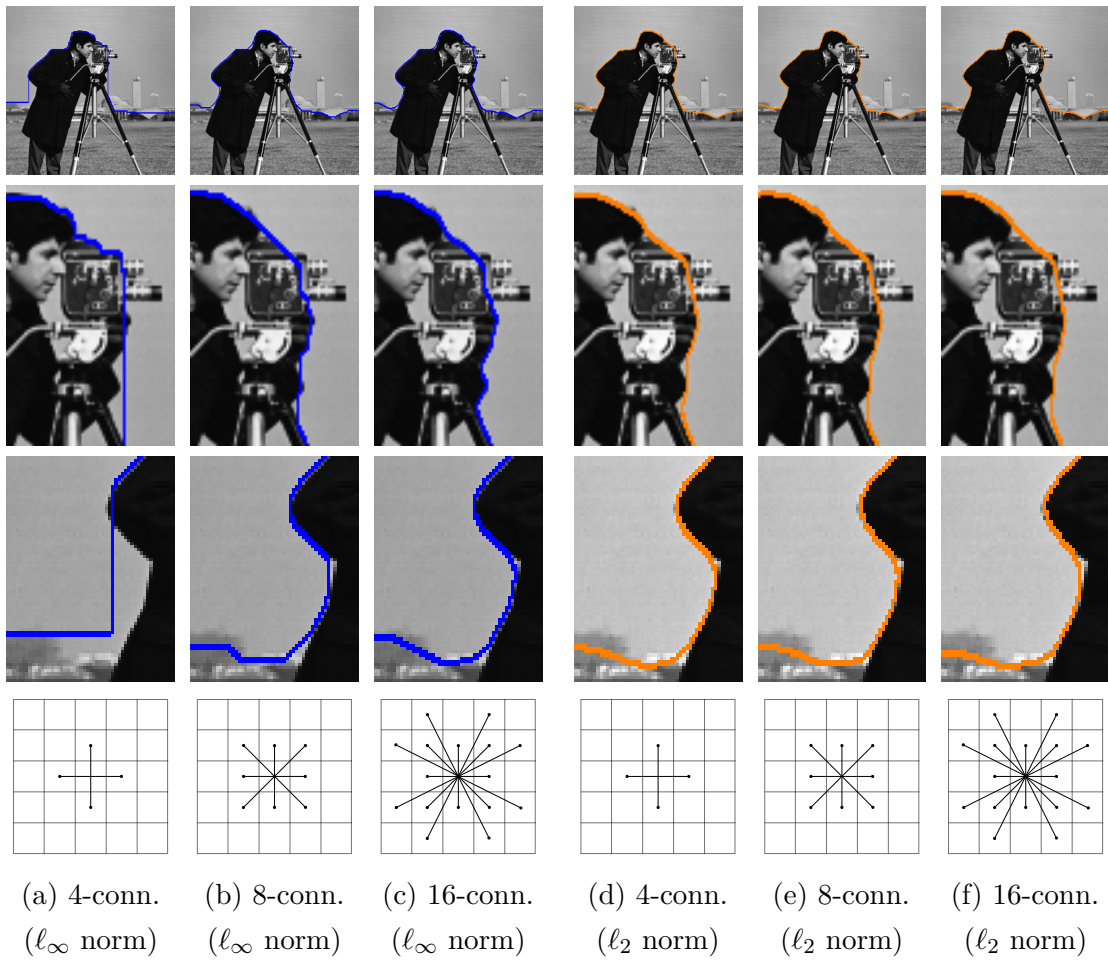


Figure 5.4.: Comparison of different neighborhood connectivities on the *cameraman* test image using the ℓ_∞ - and ℓ_2 -norm for the dual variable p . The use of the ℓ_∞ -norm results in metrication artifacts similar to those of the graph cut framework (Compare to Fig. 5.3). The ℓ_2 -norm allows to measure the Euclidean norm of the boundary length instead.

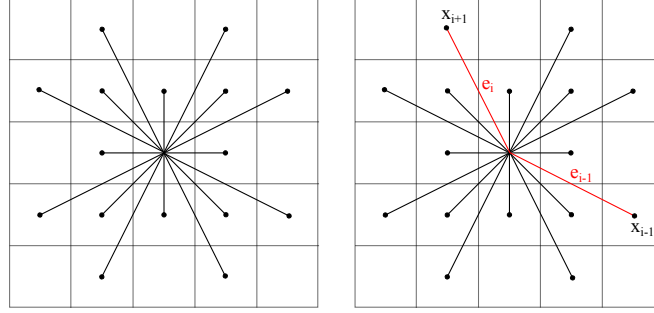


Figure 5.5.: Discretized neighborhood on the pixel grid that is used for the shortest path search. The bending energy depends on the two edges e_{i-1} and e_i joining at a node x_i .

Bending Energy Prior Additional a-priori information about the geometry of the object that should be segmented can be included in the framework, however this part is optional. For the special case of blood vessel segmentation in medical imaging it is a reasonable assumption, that a blood vessel in a stress free state minimizes its bending energy E_{bend} .

To compute the bending energy in a discretized framework we use the discretized bending energy of Bergou *et al.* [11] that can be applied for curves in 2D as well as spacecurves in 3D. It is expressed using the *curvature binormal*

$$(\kappa \mathbf{b})_i = \frac{2\mathbf{e}^{i-1} \times \mathbf{e}^i}{|\mathbf{e}^{i-1}| |\mathbf{e}^i| + \mathbf{e}^{i-1} \cdot \mathbf{e}^i} \quad (5.30)$$

with $e_i = x_{i+1} - x_i$ and $e_{i-1} = x_i - x_{i-1}$. Because this is an integrated quantity, dividing it by the length of the domain of integration, in this case half the length of the edges joining at x_i , gives the discretized version of the bending energy

$$E_{\text{bend}}(x_i) = \frac{1}{2} \alpha \left(\frac{(\kappa \mathbf{b})_i}{\bar{l}_i/2} \right)^2 \frac{\bar{l}_i}{2} = \frac{\alpha (\kappa \mathbf{b})_i^2}{\bar{l}_i}. \quad (5.31)$$

Note that the curvature binormal $(\kappa \mathbf{b})_i$ depends not only on the position x_i but also on the positions of the neighboring nodes x_{i+1} and x_{i-1} .

Computing the Shortest Path Tree Finally, the combination of the non negative data term and the bending energy prior leads to the (discretized) geodesic shortest path problem

$$\min_{sPx} \sum_{i=1}^{n(P)} f_\epsilon^+(P(i)) + E_{\text{bend}}(P(i)), \quad (5.32)$$

where with sPx we denote a path from s to x of length $n(P)$ in the discretized domain and $P(i)$ returns the i -th vertex in P . For numerical stability of the shortest path algorithm, we use the function $f_\epsilon^+(i) = \max(\epsilon, f(x_i))$.

Note that this is not a usual geodesic measure, because the bending energy term depends on the angle between the incoming and outgoing edge. Thus, standard first-order techniques [128, 144] can't be used. Instead, such cost functions can be minimized by computing a shortest path on a higher order graph, which contains a node for every edge in the original graph [3]. However, this approach results in a search problem of high complexity. To achieve a feasible runtime also for large datasets, we approximate

the minimal path by using a *greedy* optimization scheme, in this case Dijkstra's shortest path algorithm [34] on the pixel grid, using the extended pixel neighborhood depicted in Fig. 5.5. At every expansion step of Dijkstra's algorithm the value of (5.32) for the candidate nodes x_{i+1} is computed by taking the predecessor x_{i-1} in the current shortest path to x_i . Thus this approximation does not take into account different incoming directions to the node x_i but assumes the incoming directions to be fixed by x_{i-1} . The result of Dijkstra's shortest path algorithm is a geodesic shortest path tree, that spans the whole image, and defines a unique path from the source to every pixel in the image.

In the continuous setting, we formulated the connectivity constraint as monotonicity constraint along geodesics. As discussed in the previous Section 5.4.1, on the discrete domain, a geodesic from the root s to a point x amounts to the shortest path between s and x . Thus, the connectivity constraint corresponds to a monotonicity constraint along shortest paths. All the shortest paths originating from s form a shortest path tree T_s with root vertex s , and the shortest path from s to x in the discretized image domain is a connected path in T_s . Thus, the connectivity constraint along shortest paths can be formulated on the edges of T_s as follows.

On the shortest path tree T_s , the connectivity constraint is equivalent to the constraint that the label u_i of a node i is always greater or equal than the label of a neighboring node j with a larger distance $d(j)$ to the root node: $d(i) < d(j) \Rightarrow u_i \geq u_j$. Because the graph structure is a shortest path tree, the condition $d(i) < d(j)$ is satisfied for all nodes i and their child nodes j . The constraint $u_i \geq u_j$ then implies $\partial_i u_j \leq 0 \forall ij \in E(T_s)$. This constraint is linear in u , which preserves convexity of Eq. (5.22) and allows for an optimal solution.

The image segmentation problem with connectivity constraints defined over the edges of the tree T_s thus becomes

$$\min_{u:V \rightarrow [0,1]} \sum_{i \in V} \left\{ f_i u_i + \lambda |\nabla_i u| \right\} \quad (5.33)$$

$$\text{s.t.} \quad \forall ij \in E(T_s), \partial_i u_j \leq 0, \quad (5.34)$$

where we define the gradient operator ∇_i on a regular grid and the connectivity constraint over the edges of T_s .

Also for this discretized domain, we can show that every thresholded version of a feasible minimizer of (5.33) is feasible with respect to the constraints (C1) of the original optimization problem (P1).

Theorem 5.4.1. *Let u^* be a feasible minimizer of (5.33). Let $T_s = (E_T, V_T)$ denote the directed graph of the connectivity constraints, i. e. for each inequality constraint $u_i^* \geq u_j^*$ there exists a directed edge $(i, j) \in E$. Then every upper level set $\Sigma_{\{u^* > \mu\}}$ of u^* is a connected subset on G .*

Proof. Assume that $\Sigma_{\{u^* > \mu\}}$ is not connected on T_s . Then there has to exist a node $j \in V_T$, for which the parent $i \in V_T$ with $(i, j) \in E_T$ is not in $\Sigma_{\{u^* > \mu\}}$.

$$\begin{aligned} i \notin \Sigma_{\{u^* > \mu\}} &\implies u_i^* \leq \mu, \\ j \in \Sigma_{\{u^* > \mu\}} &\implies u_j^* > \mu, \end{aligned} \quad (5.35)$$

and therefore $u_i^* < u_j^*$.

This contradicts the connectivity constraint $(i, j) \in E_T \iff u_i^* \geq u_j^*$. \square

5.4.2. Legendre-Fenchel Duality

Note that the connectivity constraints (5.34) of the optimization problem (5.33) are linear constraints. Thus Slater's condition holds and we have strong duality (see Section 2.4.1 for further details).

We include the connectivity constraint by adding the indicator function

$$\delta_{\leq 0}(\partial_i u_j) = \begin{cases} 0 & \text{if } \partial_i u_j \leq 0, \\ \infty & \text{else.} \end{cases} \quad (5.36)$$

to the segmentation model and get

$$\min_{u: V \rightarrow [0,1]} \sum_{i \in V} \left\{ f_i u_i + \lambda |\nabla_i u| \right\} + \sum_{ij \in E(T_s)} \delta_{\leq 0}(\partial_i u_j). \quad (5.37)$$

As we have seen in Section 2.4.2, the indicator function of the inequality constraints in Eq. (5.37) can be included in the primal-dual framework by replacing it with its bi-conjugate

$$\delta_{\leq 0}^{**}(\partial_i u_j) = \sup_{\alpha_{ij} \geq 0} \alpha_{ij} \partial_i u_j, \quad (5.38)$$

where α_{ij} are dual variables defined over the edges $ij \in E(T_s)$ of the constraint graph.

We optimize also in these dual variables α_{ij} and get as final update equations with connectivity constraints

$$\begin{aligned} p_{ij}^{k+1} &= \pi_{|p_i| \leq 1} \left(p_{ij}^k + \sigma \partial_i \bar{u}_j^k \right) \\ \alpha_{ij}^{k+1} &= \pi_{|\cdot| \geq 0} \left(\alpha_{ij}^k + \nu \partial_i \bar{u}_j^k \right) \\ u_i^{k+1} &= u_i^k + \tau \operatorname{div}_i p^{k+1} + \tau \operatorname{div}_i^{T_s} \alpha^{k+1} - \tau f_i \\ \bar{u}_i^{k+1} &= u_i^{k+1} + \theta \left(u_i^{k+1} - u_i^k \right), \end{aligned} \quad (5.39)$$

where div^{T_s} is evaluated on the edges of the constraint graph.

Also in this case, we determine the step sizes τ , σ , and ν using the diagonal precondition method described in [112].

5.5. Experimental Results

We applied our method to different types of image data. Figure 5.1 shows the strong capabilities of our segmentation algorithm for the task of blood vessel segmentation in three dimensional CT angiography data¹. With the tree shape prior, even the small distal tips of the blood vessels are preserved in the final segmentation, while image noise that does not belong to the connected foreground region is successfully suppressed. To segment the whole volume of size $512 \times 512 \times 355$ voxels our algorithm needs 330 seconds on a single threaded 2.27 GHZ Intel Xeon architecture, which is less than 1 second per 512×512 volume slice.

Furthermore, the connectivity prior is also a useful extension in an interactive segmentation framework. Figure 5.6 shows an input image with additional user scribbles, that

¹ CT dataset taken from the *Vessel Segmentation in the Lung 2012 Grand Challenge* <http://vessel12.grand-challenge.org>.

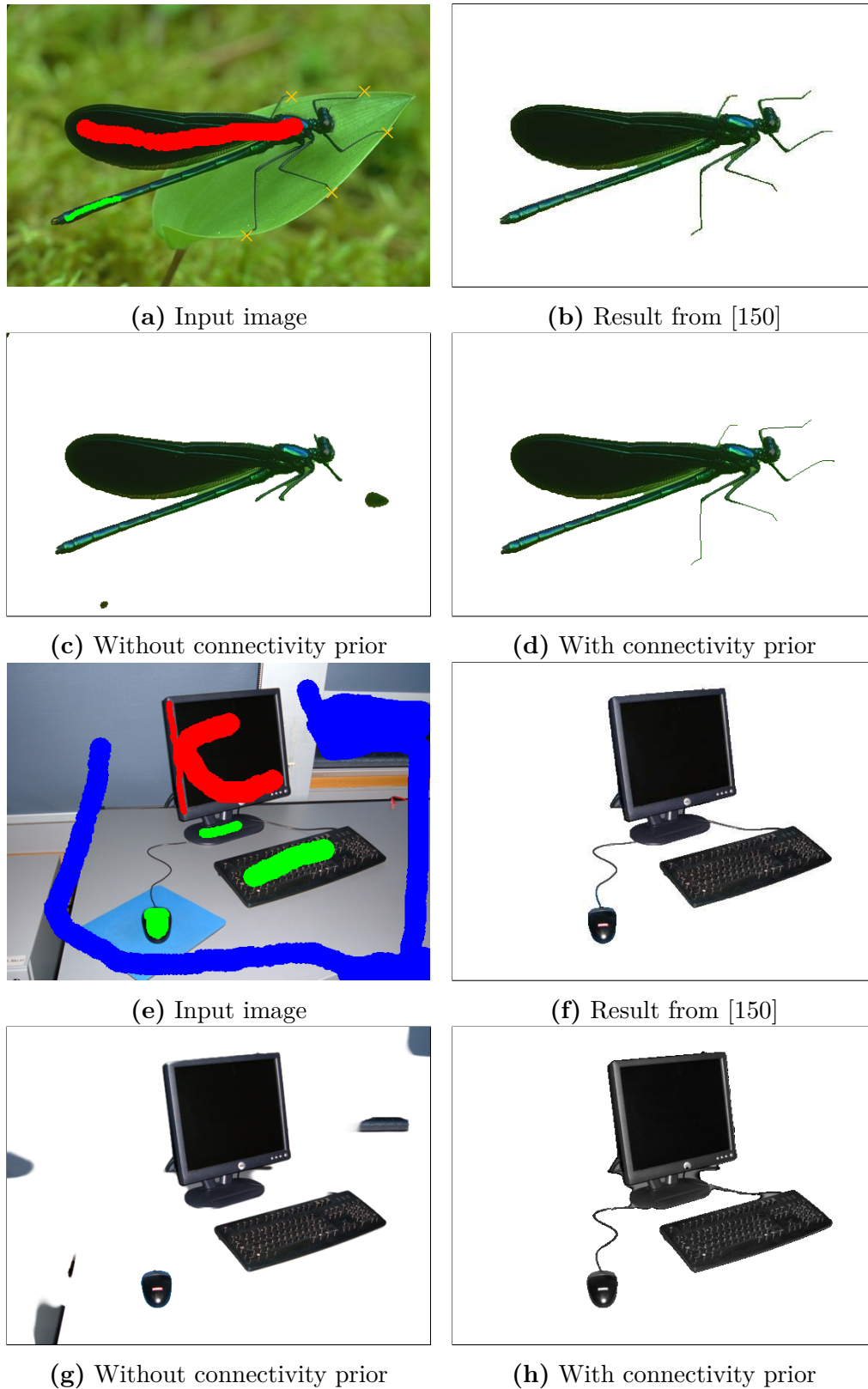


Figure 5.6.: Results for user interactive segmentation. For comparison we show the results on an image from [150]. (a) and (e) Input image with user scribbles. The red scribble is the source foreground region of the geodesic shortest path tree, green scribbles are foreground regions that should be connected and red scribbles are background regions. (b) and (f) Segmentation results from [150]. (c) and (g) Segmentation without connectivity prior. (d) and (h) Segmentation result with the proposed connectivity prior.

	Accuracy	Sensitivity	Specificity
2 nd Observer	94,73%		
Connectivity Prior			
w Bending Energy	94,57%	84,50%	95,83%
w/o Bending Energy	94,56%	84,65%	95,79%
Staal	94,42%		

Figure 5.7.: Quantitative evaluation results of the proposed method on the DRIVE database [131]. A combination of the connectivity prior with the method of Staal leads to the most accurate method on this dataset, almost reaching the performance of a second human observer.

provide hard constraints for foreground and background regions. With these scribbles the user can describe how the shortest path tree is constructed. One foreground region acts as the root node of the shortest path tree. Additional foreground regions can be added via brush strokes that should be connected to the root region.

In all our experiments, we estimate the probability density functions for foreground and background from user scribbles using a Parzen window estimator, with a Gaussian kernel $k_\sigma(I(x) - I_s)$ centered at every image value I_s of the user scribbles.

We quantitatively evaluated the method on the DRIVE database [131] of digital retinal images for vessel extraction. Because the main contribution in this work is the connectivity prior and not the design of a special data term for retinal blood vessel detection, the performance of the tree shape prior was evaluated by using the method of Staal [131] as data term. This is the currently best performing method in the benchmark with an accuracy of 94,42%. By combining this method with the proposed connectivity prior the accuracy can be increased to 94,57%. Therefore this is the highest accuracy reported for this database, almost reaching the accuracy of a human observer (94,73%). Including the bending energy term leads to an increased specificity and a slightly increased accuracy, while the sensitivity is slightly decreased. Overall, the number of true positive classified pixels is increased and the number of true negatives is decreased, and in some cases topological ambiguities are solved (Fig. 5.9). On average, the runtime until convergence on a single threaded 2.27 GHz Intel Xeon architecture was 71.65 s per image, with a standard deviation of 31.56 s. To determine the runtime needed for convergence we first computed a solution using a relatively large number of iterations (*e.g.* 10.000), restarted the algorithm and stopped when the difference between both results reached a value below 10^{-4} .

In a recent study, Rempfler *et al.* [117] propose a constraint generation scheme in an integer linear programming framework to solve the minimum cost connected subgraph (MCCS) problem, which corresponds to the original discrete optimization problem (5.1) without the boundary length regularizer. They are able to solve 12 out of 20 problem instances from the DRIVE benchmark to global optimality with a median runtime of 500 s per image. They compare the optimal solution of the MCCS problem with the solution obtained with the geodesic tree shape prior presented here, and found no difference regarding F1-score, precision, and recall. In all solvable cases, the geodesic tree shape prior result matched the exact result within a relative difference of 10^{-4} .

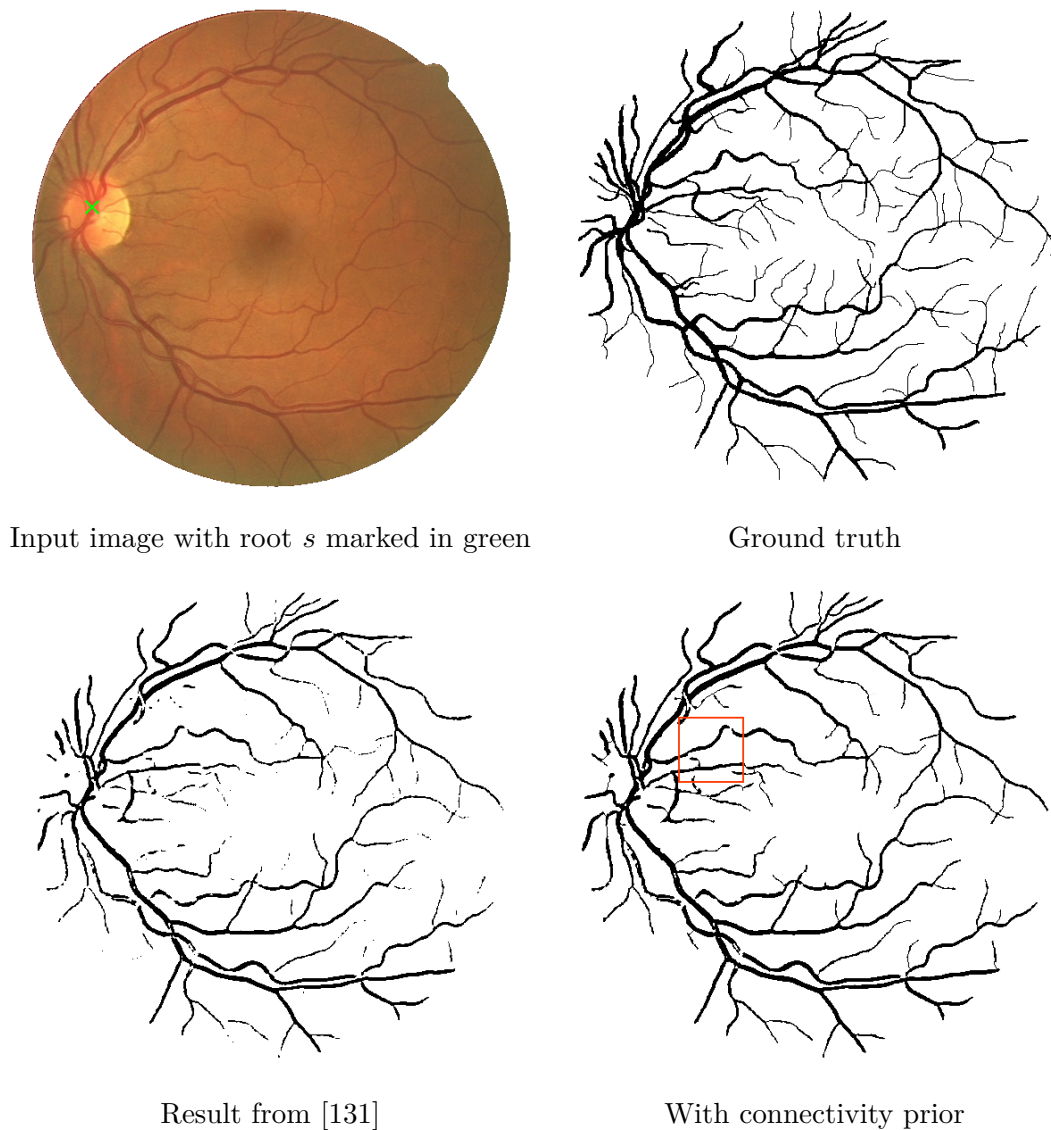


Figure 5.8.: Results on an image of the DRIVE benchmark. The connectivity prior increases the segmentation accuracy and allows to connect previously unconnected parts to the vascular network. The region denoted with the red box is shown in Fig. 5.9.

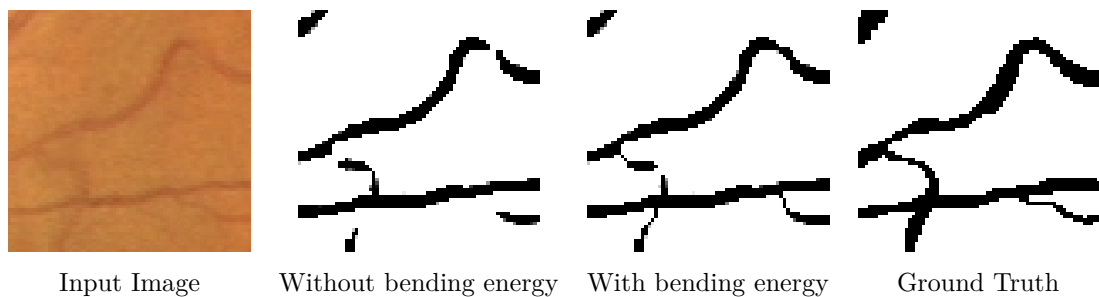


Figure 5.9.: Magnified result from the DRIVE dataset. The bending energy term helps to resolve ambiguities about the topology of the connected structure.

5.6. Conclusion

We presented a novel method for image segmentation with connectivity constraints. While solving the image segmentation problem with general connectivity constraints is NP-hard, we propose to formulate the constraint on a geodesic shortest path tree, leading to the novel tree shape prior.

We show that our method can be successfully applied to medical image segmentation problems in angiography and retinal blood vessel extraction, where thin structures otherwise would not be preserved by boundary length regularizers. Experiments on a public dataset show that combining the connectivity prior with existing image segmentation methods clearly improves the performance. To formulate the optimization problem on a discrete domain, we generalized an efficient primal dual optimization algorithm for arbitrary graphs.

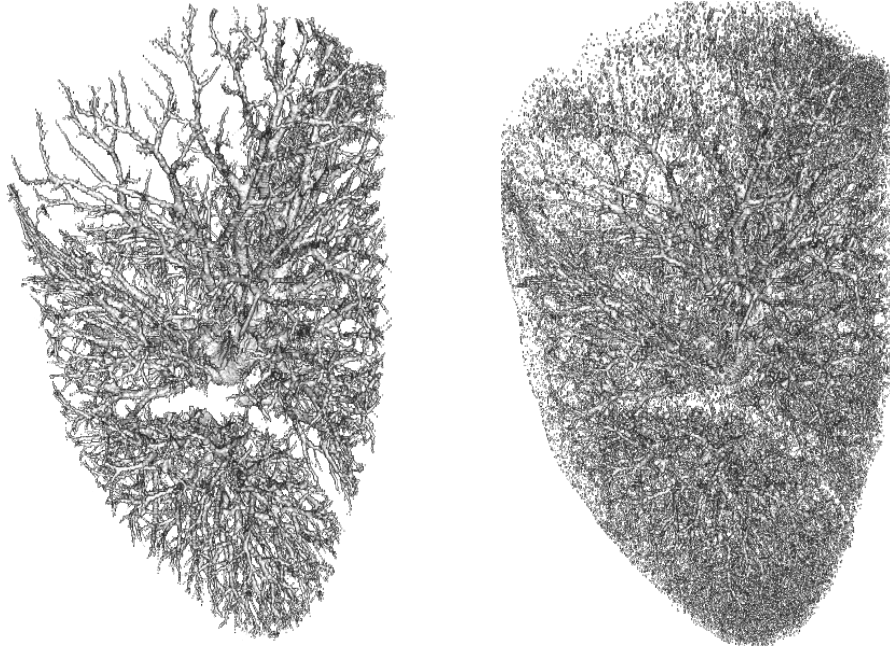
6. A Fast Projection Method for Connectivity Constraints

In this chapter we present how to efficiently project onto the feasible set of the connectivity constraints presented in the previous chapter. The constraints form a convex set and the convex image segmentation problem with a total variation regularizer can be solved to global optimality in a primal-dual framework. Efficiency is achieved by directly computing the update of the primal variable via a projection onto the constraint set, which results in a special quadratic programming problem similar to the problems studied as isotonic regression methods in statistics, which in this case can be solved with $O(n \log n)$ complexity. We show that especially for segmentation problems with long range connections this method is by orders of magnitudes more efficient, both in iteration number and runtime, than solving the dual of the constrained optimization problem. Experiments validate the usefulness of connectivity constraints for segmenting thin structures such as veins and arteries in medical image analysis. Part of the results presented in this chapter have been published in [135].

6.1. Introduction

To allow to preserve thin structures, topological constraints, and especially those that preserve connectivity [139, 150], have been introduced into image segmentation methods. These constraints have a great advantage in several application areas, including the segmentation of arteries and veins in medical imaging but also in a user interactive setting for general image segmentation. They are very useful when thin structures should be extracted from image data, allowing to extract the whole branching tree of blood vessels in the lung, as shown on the left in Fig. 6.1. For comparison, a total variation regularized segmentation of the dataset without connectivity constraints is shown on the right. In order to preserve the thin structures, only a very small weight of the regularizer can be chosen. Therefore a lot of noise is still present in the final segmentation.

In the previous chapter and in our work [139], we propose a global optimal segmentation method with reformulated connectivity constraints in a convex optimization framework. The combination of a total variation regularizer with the connectivity constraint allows to segment thin structures even in very noisy image data. In [139] we propose to solve the resulting constrained optimization problem by computing a solution of the dual optimization problem. However, another method to include the constraints is a projection onto the feasible set. In this chapter we describe an efficient projection scheme for the connectivity constraints, which allows to directly compute a solution for the update of the primal variable by a projection of the primal variable onto the feasible set. We show that the constraints form a convex set and derive a projection algorithm from isotonic regression methods in statistics. We verify in experiments that especially for segmentation problems with long range connections the projection method is by orders of magnitudes more efficient, both in iteration number and runtime, than solving the dual of the constrained optimization problem.



Result with connectivity constraint Without connectivity constraint

Figure 6.1.: Connectivity constraints allow to extract the whole branching tree of blood vessels in the lung, as shown on the left. For comparison, a total variation regularized segmentation without connectivity constraints is shown on the right. In order to preserve the thin structures, only a very small weight of the regularizer can be chosen, therefore a lot of noise is still present in the final segmentation. *CT dataset from the Vessel Segmentation in the Lung 2012 Grand Challenge*

For an overview of related work on image segmentation with topological constraints please refer to Section 5.1.1.

6.2. Connectivity Constraints in Image Segmentation

First we review the results from [139] and the previous chapter, where image segmentation with connectivity constraints is formalized as the constrained optimization problem

$$\begin{aligned} \min_{l: \Omega \rightarrow \{0,1\}} \quad & \int_{\Omega} f(x) l(x) \, dx + \lambda \operatorname{Per}(\Sigma_l, \Omega) & \text{(P1)} \\ \text{s.t.} \quad & \forall x \in \Sigma_l : \exists \bar{C}_s^x \subset \mathcal{G}_s, \bar{C}_s^x \subset \Sigma_l & \text{(C1)} \end{aligned}$$

with the domain Ω , a bounded connected subset of \mathbb{R}^m , and $BV(\Omega; [0, 1])$ is the space of functions with bounded variation. The data term $f : \Omega \rightarrow \mathbb{R}$ is chosen in such a way that it is negative for image values which are more likely to be foreground and positive in regions which should be regarded as background, e.g. the log ratio

$$f(x) = \log \frac{P(I(x)|l(x) = 0)}{P(I(x)|l(x) = 1)}, \quad (6.1)$$

with the image I and the discrete label assignment $l : \Omega \mapsto \{0, 1\}$, that describes if an image region belongs to the object of interest $l(x) = 1$ or the image background $l(x) = 0$, and $\operatorname{Per}(\Sigma_l, \Omega)$ measures the boundary length of the foreground region Σ_l in Ω , with $\Sigma_l = \{x \in \Omega : l(x) = 1\}$.

With \mathcal{G}_s we denote the set of all geodesics that pass through a given point s , for example defined by user input, defined by a metric that depends on a probabilistic model for foreground and background probabilities, and $\bar{C}_s^x \subset \mathcal{G}_s$ denotes the shortest geodesic from s to a terminal point x .

The solution of the optimization problem should satisfy the connectivity constraint **C1**:
For each $x \in \Omega$ that belongs to the foreground there must exist a connected shortest geodesic path from a given $s \in \Omega$ to x such that all $p \in \Omega$ in the path between x and s belong to the foreground.

This constraint not only ensures the connection of every labeled foreground region to s but also ensures that the whole foreground segment is connected.

6.3. Constrained Convex Optimization

On a discretized domain, the geodesics form a geodesic shortest path tree, a directed acyclic graph $\mathcal{G}_s = \{V, E\}$ with the set of vertices V with $|V| = n$ and the set of directed edges $E \subset V \times V$ with $|E| = m$. With the local variation regularizer introduced in the previous chapter the image segmentation problem Eq. (P1) can be written as the optimization problem

$$\min_{u:V \rightarrow [0,1]} \sum_{i \in V} \left\{ f_i u_i + \lambda |\nabla_i u| \right\} \quad (6.2)$$

where the discrete label assignment has been relaxed by introducing the continuous indicator function $u : V \rightarrow [0, 1]$ and the operator ∇_i is evaluated on the pixel grid. We further follow the framework we introduced in the previous chapter and in [139] and formulate the global connectivity constraint as a monotonicity constraint over each edges of this graph. To satisfy the connectivity constraint we observe that the value of the discretized value function u_i of a node i with distance to the root node d_i should always be greater or equal than the labels of its neighbors with a larger distance $d_j > d_i$ to the root node. This implies that the *directional derivative*

$$\partial_i u_j := (du)(e_{ij}) = (u(j) - u(i))$$

of u at vertex i along the edge to vertex j should always be less than or equal to zero. Thus we get the constrained optimization problem

$$\begin{aligned} \min_{u:V \rightarrow [0,1]} \quad & \sum_{i \in V} \left\{ f_i u_i + \lambda |\nabla_i u| \right\} \\ \text{s.t.} \quad & \partial_i u_j \leq 0, \quad \forall (i, j) \in E. \end{aligned} \quad (6.3)$$

This image segmentation problem can be optimized using the Primal-Dual framework of [24, 114] which can be applied to convex optimization problems with a saddle-point structure

$$\min_{u \in U} \max_{p \in P} \langle Ku, p \rangle + G(u) - F^*(p), \quad (6.4)$$

where U and P are finite-dimensional vector spaces, $K : U \rightarrow P$ is a continuous linear operator and $G : U \rightarrow [0, +\infty)$ and $F^* : P \rightarrow [0, +\infty)$ are proper convex lower semi-continuous functions. Recall from the introduction in Section 2.5 that the update steps in [24] are computed using the **prox**-operator, which is defined as

$$\mathbf{prox}_{\lambda f}(v) = \arg \min_x f(x) + \frac{1}{2\lambda} \|x - v\|_2^2. \quad (6.5)$$

Using this **prox**-operator, the updates in the primal variable u and the dual variable p are computed as

$$\begin{aligned} p^{k+1} &= \mathbf{prox}_{\sigma F^*} \left(p^k + \sigma K \bar{u}^k \right) \\ u^{k+1} &= \mathbf{prox}_{\tau G} \left(u^k - \tau K^* p^{k+1} \right) \\ \bar{u}^{k+1} &= u^{k+1} + \theta \left(u^{k+1} - u^k \right). \end{aligned} \quad (6.6)$$

To formulate the image segmentation problem Eq. (6.3) in the Primal-Dual framework we reformulate the total variation regularizer by introducing a dual variable $p : V \mapsto \mathbb{R}^2$ [114] and arrive at the saddle point problem

$$\min_{u_i \in [0,1]} \max_{|p| \leq 1} \lambda \langle \nabla u_i, p \rangle + \langle f, u \rangle + \sum_{(i,j) \in E} \delta_{\leq 0}(\partial_i u_j), \quad (6.7)$$

where the connectivity constraints are included by adding their indicator functions. Note that while the constraints are defined on the graph \mathcal{G}_s , the gradient operator ∇_i in the regularizer is computed on the image grid. We identify the function $G(u)$ in (6.4) with

$$G(u) = \langle f, u \rangle + \sum_{(i,j) \in E} \delta_{\leq 0}(\partial_i u_j). \quad (6.8)$$

While the constraints over the domains of u and p can be solved by simple projections, the optimization with respect to the connectivity constraint is more involved. In the following, we will investigate two different strategies to incorporate the connectivity constraint.

6.3.1. Optimization via Fenchel Duality

In [139] we propose to optimize the dual of the constrained optimization problem

$$\min_{u_i \in [0,1]} \max_{\substack{|p| \leq 1 \\ \alpha_{ij} \geq 0}} \lambda \langle \nabla_i u, p \rangle + \langle f, u \rangle + \sum_{(i,j) \in E} \alpha_{ij} \partial_i u_j. \quad (6.9)$$

The connectivity constraint is ensured by introducing an additional dual variable α_{ij} for each edge $(i, j) \in E$. Especially for long range connections the convergence of these multipliers is very slow as we show in our experiments in section 6.4.

6.3.2. Projection onto the Constraint Set

In this section we describe how the connectivity constraint can be included by directly computing the update of the primal variable subject to the constraint. We propose an efficient projection scheme to solve the constrained quadratic programming problem, which results from the definition of the **prox**-operator.

According to [24] the update in the primal variable u is defined as

$$u_i^{k+1} = \mathbf{prox}_{\tau G} \left(u_i^k + \tau \operatorname{div}_i p^{k+1} \right) \quad (6.10)$$

$$= \arg \min_{v \in [0,1]} \left\{ \frac{\|v - (u_i^k + \tau \operatorname{div}_i p^{k+1})\|^2}{2\tau} + \langle f_i, v \rangle + \sum_{(i,j) \in E} \delta_{\leq 0}(\partial_i u_j) \right\}, \quad (6.11)$$

where we inserted the function G from (6.8).

By completing the square and omitting terms independent of v we arrive at

$$u_i^{k+1} = \arg \min_{v \in [0,1]} \left\{ \left\| v - (u_i^k + \tau \operatorname{div}_i p^{k+1} - \tau f_i) \right\|^2 + \sum_{(i,j) \in E} \delta_{\leq 0}(\partial_i u_j) \right\} \quad (6.12)$$

which is of the general form

$$\begin{aligned} & \arg \min_{v: V \rightarrow [0,1]} \|v - \tilde{u}\|^2 \\ & \text{s.t.} \\ & v_i \geq v_j, \quad \forall (i, j) \in E, \end{aligned} \quad (6.13)$$

with $\tilde{u} = (u^k + \tau \operatorname{div} p^{k+1} - \tau f)$.

Proposition 6.3.1. *The feasible set C determined by the constraints of the optimization problem Eq. (6.13) is a closed convex set.*

Proof. Let C_1 be the feasible set determined by the inequality constraints and let C_2 denote the range of v . The feasible set of Eq. (6.13) then is $C = C_1 \cap C_2$. First we show that C_1 is convex. If for every $a, b \in C_1$ and $\alpha, \beta > 0$ it holds that $\alpha a + \beta b \in C_1$ then C_1 is a convex cone. Because $a, b \in C_1$ it holds that

$$a_i \geq a_j, \quad b_i \geq b_j, \quad \forall (i, j) \in E, \quad (6.14)$$

and because $\alpha, \beta > 0$ it follows

$$\begin{aligned} \alpha a_i &\geq \alpha a_j, \quad \beta b_i \geq \beta b_j, \quad \forall (i, j) \in E, \\ \alpha a_i + \beta b_i &\geq \alpha a_j + \beta b_j, \quad \forall (i, j) \in E. \end{aligned} \quad (6.15)$$

Hence the set C_1 is a convex cone. In addition to the inequality constraints we also have the constraint on the range of v . We call the feasible set of this constraint $C_2 = [0, 1]$. This set is closed and convex, so $C = C_1 \cap C_2$, the intersection of both sets, is closed and convex. \square

Thus the optimization problem Eq. (6.13) is strictly convex subject to convex constraints. Its solution is an Euclidean projection of \tilde{u} onto the closed convex set C and can be solved to global optimality. Furthermore the inequality constraints describe a partial order on the values of v . A quadratic programming problem with this structure is known in statistics as isotonic regression [7].

6.3.3. Isotonic Regression on a Tree

In Pardalos *et al.* [109] the authors investigate a class of algorithms for isotonic regression where the constraints define a partial order which can be represented by a directed graph. In particular the authors propose an $O(n \log n)$ algorithm for the case when the directed graph is a directed tree with n vertices. For convenience we present the algorithm IRT-BIN from [109] here as Algorithm 2.

We call the isotonic regression problem subject to partial order constraints *IRT*. This problem does not include the range constraints of Eq. (6.13). In the following, we will show that a projection of the optimal solution of *IRT* on the range constraint yields the optimal solution of Eq. (6.13).

First we follow the presentation of Pardalos *et al.* [109] and describe the algorithm for isotonic regression with partial order constraints, using the concept of *upper sets*, *lower sets* and *level sets*:

Definition [109] Let X be a nonempty finite set. Let \preceq be a partial order on X . Let Y be a nonempty subset of X . We define the *average* of Y as $Av(Y) = \frac{1}{|Y|} \sum_{i \in Y} \tilde{u}_i$. We call a subset $L \subset X$ a *lower set* of X with respect to \preceq if $i \in X, j \in L$ and $i \preceq j$ implies $i \in L$. Consequently a subset $U \subset X$ is an *upper set* if $i \in U, j \in X$ and $i \preceq j$ implies $j \in U$. We call a subset $S \subset X$ a *level set* if there are an upper set U and a lower set L such that $S = L \cup U$. A *block* B of X is a nonempty level set such that for each upper set $U \subset X$ for which $U \cap B \neq \emptyset$ it holds that $Av(B) \geq Av(U \cap B)$.

Furthermore the authors of [109] introduce the concept of a *block class*:

Definition [109] A collection Δ of blocks of X is called a *block class* of X if

1. the blocks in Δ are pairwise disjoint and their union is the set X .
2. the collection Δ can be ordered by a partial-order \preceq such that $A \preceq B$ for $A, B \in \Delta$ if there exist $i \in A$ and $j \in B$ such that $i \preceq j$.

Note that the collection of all singleton subsets $\{x\}$ with $x \in X$ is a block class.

The authors prove that the optimal solution of *IRT* on a block B is $v_i = Av(B)$ for every $i \in B$. Furthermore they show that if a block class Δ has no adjacent violators, then the optimal solution of the isotonic regression is given by $v_i^* = Av(B(i))$, where $B(i)$ is the block which contains i , for each element i of X .

Algorithm 2 IRT-BIN from Pardalos *et al.* [109]

- 1: Let Δ be the singleton block class and let \mathcal{T} be a copy of the underlying rooted tree.
 - 2: Mark each leaf node of \mathcal{T} as solved and all other nodes as unsolved.
 - 3: **for** each node x_i of \mathcal{T} **do**
 - 4: Create a block $B(x_i) = \{x_i\}$ and a binomial heap H_i .
 - 5: **end for**
 - 6: **if** all nodes of \mathcal{T} are marked as solved **then**
 - 7: output the blocks corresponding to the nodes in \mathcal{T} as the final block class and **stop**;
 - 8: **end if**
 - 9: Let x_i be an unsolved node of \mathcal{T} such that all the children nodes of x_i are solved.
 - 10: Let $B(x_i)$ (resp. H_i) be the block (resp. binomial heap) corresponding to node x_i .
 - 11: **while** $Av(B(x_i)) < Maximum(H_i)$ **do**
 - 12: $ExtractMax(H_i)$ and let $B(x_k)$ be the corresponding block
 - 13: Shrink the edge connecting x_i to x_k ▷ the new vertex is still called v_i
 - 14: Create a new block $B(x_i) \leftarrow B(x_i) \cup B(x_k)$ ▷ the new block is still called $B(x_i)$
 - 15: Calculate the $Av(B(x_i))$ for the new block $B(x_i)$
 - 16: $H_i \leftarrow Union(H_i, H_k)$ ▷ this is the binomial heap for the new block $B(x_i)$
 - 17: **end while**
 - 18: Mark the node x_i of \mathcal{T} as solved.
 - 19: Let x_p be the parent node of x_i in \mathcal{T} . Let H_p be the binomial heap corresponding to $B(x_p)$ and let a_i be the node in H_p which corresponds to $B(x_i)$. $ChangeKey(a_i, Av(B(x_i)), H_p)$.
 - 20: **go to** 6.
-

We will show with the proof of the following proposition that given a solution v^* of *IRT* the optimal solution to Eq. (6.13) is achieved by projecting v^* on C_2 . Thus, we can directly project onto the constraints of the optimization problem Eq. (6.13) by first projecting onto the isotonicity constraint and then onto the $[0, 1]$ -box constraint.

Obviously, projecting first onto the $[0, 1]$ -box constraint and then onto the isotonicity constraint will not lead to a valid projection. When the averaging step is performed after the $[0, 1]$ clipping, in case that the isotonicity constraint is violated and some values are smaller 1, only block average values well below 1 can be achieved, even when the average of the block before projection was larger than 1.

Proposition 6.3.2 (Direct Projection onto the Constraint Set). *Let B be a block of X . Let $v_i^* = Av(B)$ for every $i \in B$ be the solution of *IRT*. Let $\pi_{[0,1]} : \mathbb{R} \rightarrow [0, 1]$ be a projection that projects negative values to 0 and values larger than 1 to 1. Then $\{\pi_{[0,1]}(v_i^*) : i \in B\}$ is the optimal solution to the optimization problem (6.13) on B .*

Proof. Let us assume that B has m elements x_1, x_2, \dots, x_m . We look at the three cases $Av(B) > 1$, $Av(B) \in [0, 1]$ and $Av(B) < 0$. Obviously these three cases are exhaustive. If $Av(B) \in [0, 1]$ then the solution v^* of *IRT* also fulfills the range constraint and the solution of Eq. (6.13) for the set B is identical to the solution of *IRT* on B .

We follow a similar proof as in [109] and show that if $Av(B) > 1$ the point

$$\begin{aligned} \{\pi_{[0,1]}(v_i^*) : i \in B\} &= (\pi_{[0,1]}(Av(B)), \pi_{[0,1]}(Av(B)), \dots, \pi_{[0,1]}(Av(B))) \in \mathbb{R}^m \\ &= (1, 1, \dots, 1) \in \mathbb{R}^m \end{aligned} \quad (6.16)$$

is the optimal solution to Eq. (6.13) by showing that the inner product of the gradient of Eq. (6.13) with any feasible direction $d \in \mathbb{R}^m$ at that point is a non-negative number.

Let $d = (d_1, d_2, \dots, d_m)$ be a feasible direction of the isotonic regression problem on B . Then, in order to preserve isotonicity, feasibility of the direction d implies $d_i \leq d_j$ when $x_i \leq x_j$.

Therefore there exists a permutation $\sigma = (\sigma(1), \sigma(2), \dots, \sigma(m))$ such that

$$d_{\sigma(1)} \geq d_{\sigma(2)} \geq \dots \geq d_{\sigma(m)} \quad (6.17)$$

and

$$x_{\sigma(i)} \preceq x_{\sigma(j)} \implies i \leq j. \quad (6.18)$$

To prove that for $Av(B) > 1$ the point in (6.16) is the optimal solution of the optimization problem (6.13) on the set B it is sufficient to show that

$$\sum_{i \in B} (1 - \tilde{u}_{\sigma(i)}) \times d_{\sigma(i)} \geq 0. \quad (6.19)$$

From Eq. (6.17) and from the definition of a block it follows that

$$\frac{1}{m-k+1} \sum_{i=k}^m u_{\sigma(i)} \geq Av(B) > 1 \text{ for all } 1 < k \leq m. \quad (6.20)$$

This implies that

$$\sum_{i=k}^m (1 - u_{\sigma(i)}) \leq 0 \text{ for all } 1 < k \leq m. \quad (6.21)$$

Equations (6.21) and (6.17) imply that for all $1 < k \leq m$ that the following inequality holds

$$\sum_{i=k}^m (1 - u_{\sigma(i)}) \times d_{\sigma(k-1)} \leq \sum_{i=k}^m (1 - u_{\sigma(i)}) \times d_{\sigma(k)}. \quad (6.22)$$

Because $Av(B) > 1$ the feasibility of d implies that $d_{\sigma(i)} \leq 0$ for all $i \in \{1, \dots, m\}$. Combining everything together we get

$$\begin{aligned} & \sum_{i=1}^m (1 - u_{\sigma(i)}) \times d_{\sigma(1)} & (6.23) \\ &= \sum_{i=1}^1 (1 - u_{\sigma(i)}) \times d_{\sigma(i)} + \sum_{i=2}^m (1 - u_{\sigma(1)}) \times d_{\sigma(1)} \\ &\leq \sum_{i=1}^1 (1 - u_{\sigma(i)}) \times d_{\sigma(i)} + \sum_{i=2}^m (1 - u_{\sigma(2)}) \times d_{\sigma(2)} \\ &= \sum_{i=1}^2 (1 - u_{\sigma(i)}) \times d_{\sigma(i)} + \sum_{i=3}^m (1 - u_{\sigma(2)}) \times d_{\sigma(2)} \\ &\leq \sum_{i=1}^2 (1 - u_{\sigma(i)}) \times d_{\sigma(i)} + \sum_{i=3}^m (1 - u_{\sigma(3)}) \times d_{\sigma(3)} \\ &\dots \\ &\leq \sum_{i=1}^m (1 - u_{\sigma(i)}) \times d_{\sigma(i)} & (6.24) \end{aligned}$$

From $Av(B) > 1$ it follows that

$$\sum_{i=1}^m (1 - u_{\sigma(i)}) < 0. \quad (6.25)$$

Together with $d_{\sigma(i)} \leq 0$ for all $i \in \{1, \dots, m\}$ it follows for Eq. (6.23)

$$\sum_{i=1}^m (1 - u_{\sigma(i)}) \times d_{\sigma(1)} \geq 0. \quad (6.26)$$

Therefore from Eq. (6.23) to Eq. (6.24) we have proved that if $Av(B) > 1$

$$\sum_{i=1}^m (1 - u_{\sigma(i)}) \times d_{\sigma(i)} \geq 0. \quad (6.27)$$

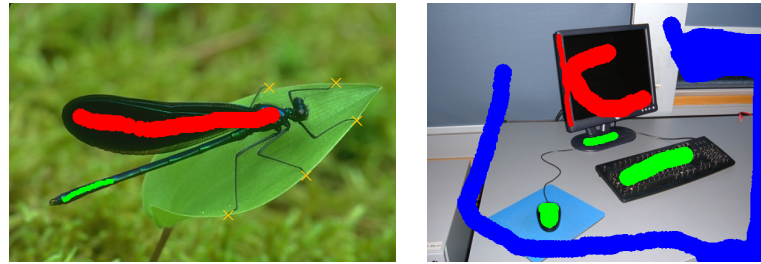
What is left show is that if $Av(B) < 0$, the inner product of the gradient of Eq. (6.13) with any feasible direction $d = (d_1, d_2, \dots, d_m) \in \mathbb{R}^m$ at the point

$$\{\pi_{[0,1]}(v_i^*) : i \in B\} = (0, 0, \dots, 0) \in \mathbb{R}^m$$

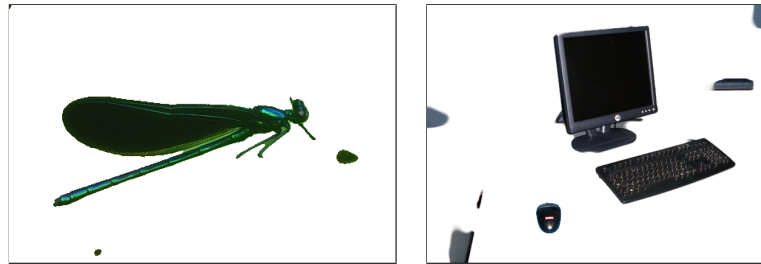
is a non-negative number. The proof is equivalent to above proof for $Av(B) > 1$. \square

6.4. Experimental Results

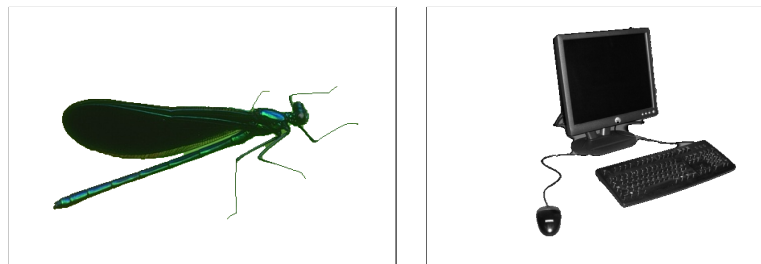
For comparison we perform experiments for interactive segmentation on images from [150] that also have been used in other publications, e.g. [38, 139]. As depicted in Fig. 6.2, the



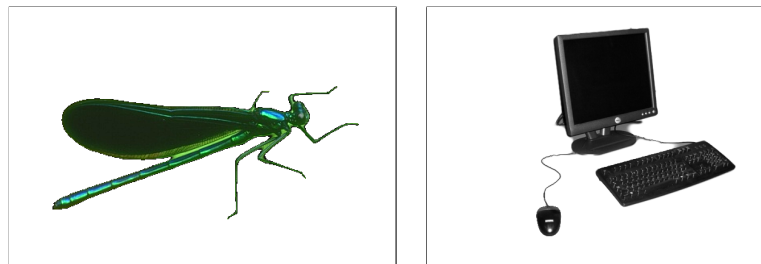
(a) Input images



(b) Image segmentation without connectivity constraints



(c) Connectivity constraints using Fenchel Duality



(d) Connectivity constraints using the projection method

Figure 6.2.: Comparison of the projection method and Fenchel duality Both methods produce the same results for interactive segmentation. (a) Input images with user scribbles. The red scribbles are the source of the geodesic shortest path tree, green scribbles are foreground regions that should be connected and blue scribbles are background regions. (b) Segmentation without connectivity constraints. (c) Segmentation with connectivity constraints by solving the dual problem. (d) Segmentation with connectivity constraints using the projection scheme.

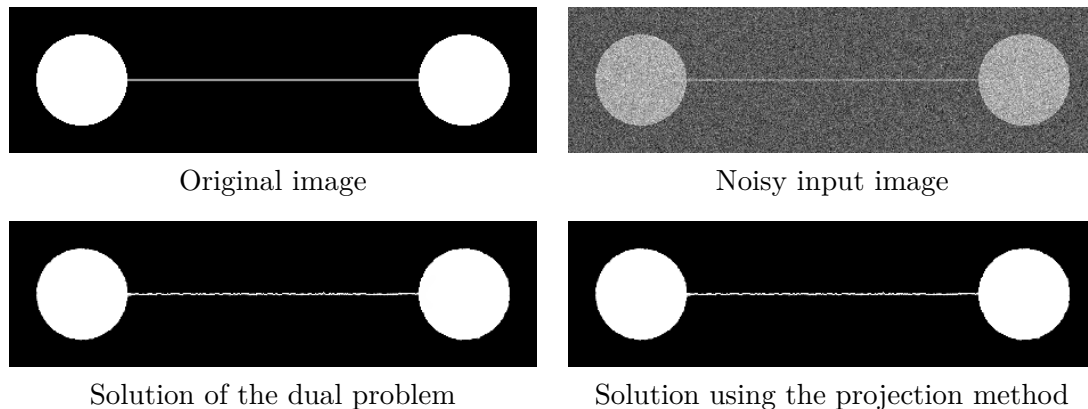


Figure 6.3.: Synthetic test image. Upper row: The input image with added Gaussian noise. Lower row: Identical results of the two different methods to include the connectivity constraint.

segmentations acquired with the projection method are not different from the results of the algorithm based on Fenchel duality [139].

We provide convergence results of the two different methods on a set of synthetic test images containing two circles that are connected by a 2 pixel wide faint path of a length of 64, 128, 256 and 512 pixels. As an example, the image for the path length of 256 pixels is depicted in Fig. 6.3.

Plots of the convergence of the two methods with respect to runtime are shown in Fig. 6.4. The projection method clearly outperforms the method based on Fenchel duality. The longer the connection, the higher the runtime difference of both methods. Convergence of the dual method takes from 10.12 seconds for the 64 pixel connection, over 41.11 seconds for 128, 251.17 seconds for 256 to 1639.15 seconds for the 512 pixel connection, whereas the projection method converges within less than 3 seconds for all different images. Although solving the isotonic regression problem results in a higher complexity of each iteration, by magnitudes fewer iterations are required for the projection method to converge. The needed runtime and number of iterations until convergence of both methods for different data sets are shown in Table 6.1. For images of the DRIVE benchmark [131], the average runtime per image on a single CPU can be decreased from 71.65 s (± 31.56 s) with the dual approach to only 2.07 s with the proposed projection scheme. Because the number of iterations needed for the projection method depends less on the length of the connections, the method depends less on the data and we observe a much smaller standard deviation of the runtime of 0.26 s. This clearly allows to use the proposed method for practical applications.

Table 6.1.: Comparison of runtime and number of iterations until convergence. Especially when the images contain long range connections, the projection method is by magnitudes more efficient than solving the dual problem. The results for the DRIVE benchmark are averaged over the whole dataset and reported together with their standard deviation.

Image	Fenchel Duality		Projection Method	
	Iterations	Runtime	Iterations	Runtime
Test Circle 64	5396	10.12 s	19	0.29 s
Test Circle 128	18318	41.11 s	20	0.52 s
Test Circle 256	81987	251.17 s	20	1.06 s
Test Circle 512	344030	1639.15 s	20	2.89 s
Fly	1226	9.13 s	54	3.66 s
Desk	3440	42.00 s	109	13.40 s
DRIVE	4192 (± 1845)	71.65 s (± 31.56 s)	12.2 (± 1.32)	2.07 s (± 0.26 s)

To measure the speed of convergence we first compute a segmentation result that is reached after a large number of iterations (*e.g.* 10.000 for the DRIVE benchmark), then restart the algorithm and stop when the absolute per pixel difference between the current result and the converged result is below 10^{-4} . All Experiments were performed on a single threaded 2.27 GHZ Intel Xeon architecture.

To get an intuition, why the projection method allows a much faster convergence than the multiplier based method, we depict the values of the labeling function u for our synthetic test image with a connection length of 256 pixels for different number of iterations in Fig. 6.5.

For the multiplier based approach, it takes a long time until the information about the disconnected part on the right has been propagated all the way along the 256 pixel wide connection. The reason for this is, that a multiplier α_{ij} is only active, if the constraint along the edge ij is not fulfilled. This however, is only the case for a limited number of edges at the far end of the missing part of the connection.

The projection method instead allows to update several values at the same time. All the values that belong to the same block class are set to the average value of that block. This allows for a much faster convergence until the connectivity constraint is fulfilled.

Further more, we observe an additional property of the connectivity constraint: missing parts of the foreground are filled not only by the regularizer, but also by the constraint. This supports the regularizer in finding a smooth segmentation and increases the convergence for regions that otherwise would have to be filled by the regularizer alone. A comparison of segmentation results achieved after a few iterations with a total variation (TV) regularized segmentation model and the same model with additional connectivity constraints is depicted in Fig. 6.6. In combination with the projection method, the connectivity constraints allow to reach a smooth segmentation result after fewer iterations than with the regularizer alone.

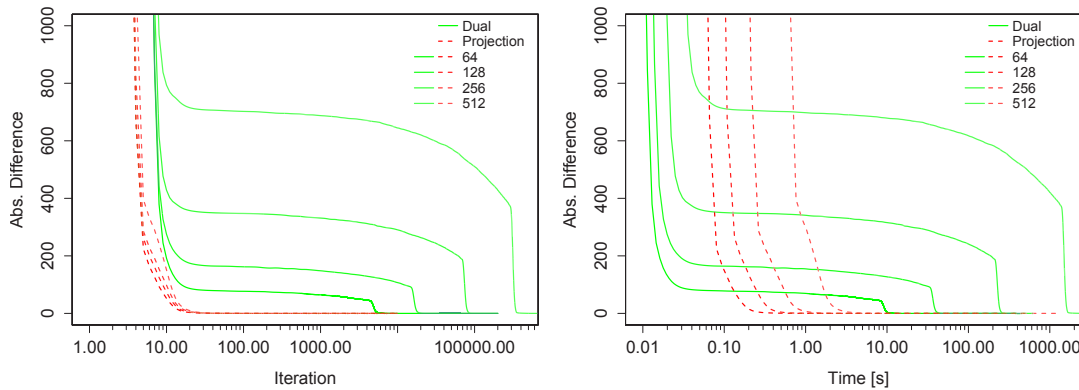


Figure 6.4.: Convergence of the two different methods to include the connectivity constraint on a set of test images as shown in Fig. 6.3. The set contains images with two circles that are connected by a 2 pixel width path of a length of 64, 128, 256 and 512 pixels. Note that the plots have a logarithmic scale at the x axes. When using the projection method (dashed line), by order of magnitudes fewer iterations are needed than for solving the dual problem (solid). This results in a by order of magnitudes better runtime performance.

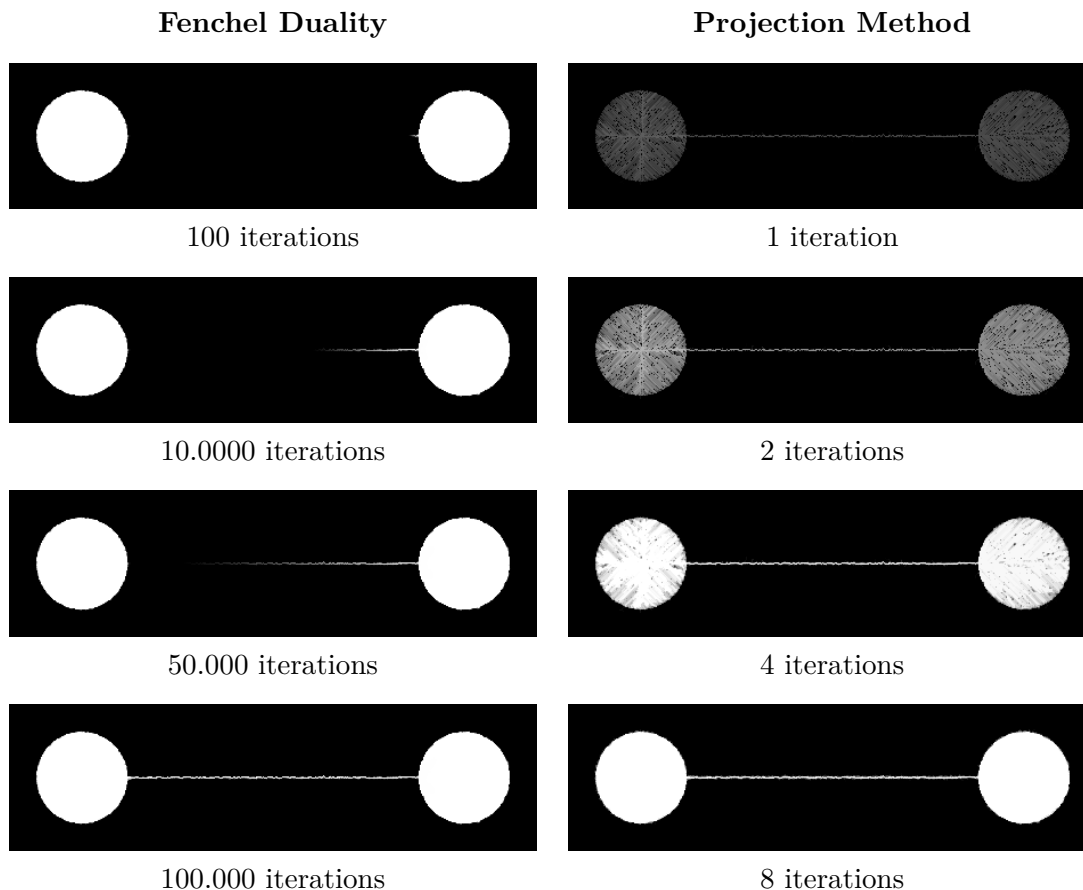


Figure 6.5.: The reason for the slow convergence of the multiplier based method is, that the multipliers are only active where the constraint is not fulfilled: at the far end of the missing part of the connection. The projection scheme instead allows to update multiple values at the same time and thus allows much faster convergence. First, the projection method updates the values of each block that contains a violated constraint. Because of the noise in the input image, some pixels inside the circles can get a background label, when they are leave nodes of the tree. Already after 8 iterations these values have been smoothed by the regularizer. In both experiments the root node s is the center of the left circle.

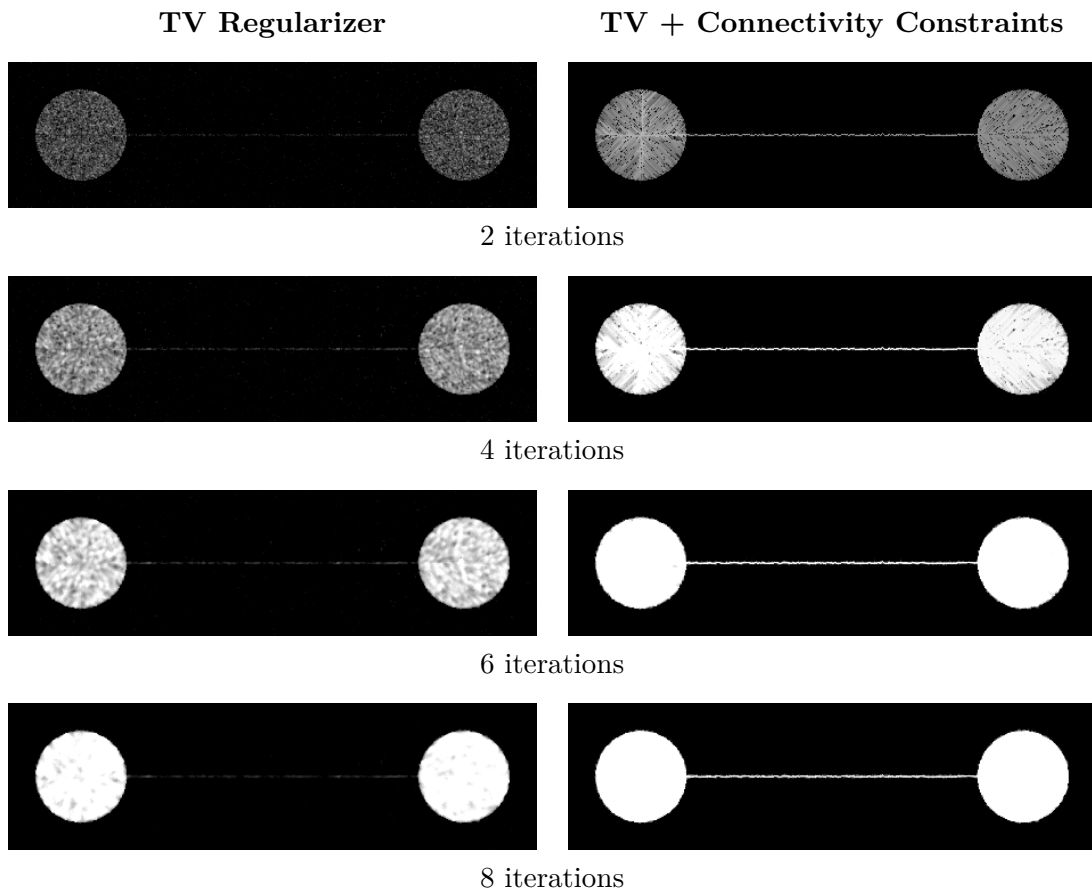


Figure 6.6.: Connectivity constraints support the regularizer in reaching a smooth segmentation result Shown are results after only a few iterations of a total variation regularized segmentation model and the same model with additional connectivity constraints. In combination with the projection method, the connectivity constraints allow to reach a smooth segmentation after fewer iterations than with the regularizer alone.

6.5. Conclusion

We presented a very efficient projection scheme to include connectivity constraints in a convex image segmentation framework. The method outperforms commonly used approaches that are based on Fenchel duality in runtime by orders of magnitudes. Instead of using the common approach to solve the dual problem of the constrained optimization problem we directly project onto the constraint set. This leads to a by order of magnitudes faster runtime performance, as significantly fewer iterations are needed until a sufficient convergence is reached. The proposed algorithm enables to use connectivity constraints for large segmentation problems as they arise for example in medical image segmentation of three dimensional CT angiography.

7. Active Online Learning for Interactive Segmentation using Sparse Gaussian Processes

The image segmentation methods presented so far, focused on the regularizer and appropriate constraints to extract a topologically connected object from the image. Another important part of an image segmentation model is the *data term*, which can be defined by a probabilistic model, that defines the probability for an image region to be part of a specific segment.

But how exactly is this probabilistic model specified? Possible choices include non-parametric models, for example a histogram or a Parzen window estimator, and parametric models, for example a mixture of Gaussian. These models are fitted to labeled data, the so called *training set*. In its most simple form, this training set is specified once and then used to fit the probabilistic model of the data term.

As an alternative and more flexible approach, we present an active learning framework to define this probabilistic model. This active learning framework allows to improve the data term in a user interactive approach. Our system uses a sparse Gaussian Process classifier (GPC) trained on manually labeled image pixels ("user scribbles") that is refined in every active learning round. To do this, our method presents a set of image regions to be labeled by the user. These regions are selected based on the *classification uncertainty* of the classifier, i.e. regions with high uncertainty are presented to the user. For small images, this seems unnecessary, when visual inspection of the segmentation result allows to quickly identify incorrectly classified regions. However, our method is well suited for large datasets. These large datasets occur for example in satellite and aerial imagery, high resolution microscopy in biology and also large image datasets such as [122].

The results presented in this chapter are joint work with Rudolph Triebel and Mohammed Souiai and have been published in [143]. Jan Stühmer and Rudolph Triebel performed the experiments and wrote the manuscript [143]. Mohammed Souiai provided code and wrote part of the manuscript [143]. The efficient online update scheme was contributed by Rudolph Triebel.

7.1. Introduction

Image segmentation is one of the most important problems in computer vision with a large range of applications, including medical imaging and robotics. However, image segmentation is an ill-posed problem in general, because the definition of a correct segmentation strongly depends on the application. In this chapter we therefore focus on *interactive* image segmentation, where the user provides information about the image to be segmented, by manually selecting regions and assigning them a specific class label. These selected regions can for example be selected with strokes drawn in the image, these strokes are also called *user scribbles*, and are used as ground truth information to infer

a good segmentation of the image. The scribbles can be used in two ways, first they can define constraints on the final segmentation, because the image labeling result should be consistent with the labels assigned manually by the user. Second, the labeled regions in the image can be used to train a probabilistic classifier to assign the correct class label to an image region. There exist many approaches for interactive image segmentation, one of the most important and central problems in computer vision, with impressive results. However, current methods reach a high classification rate only by requiring comparably many user scribbles, and the amount of user input needed usually grows rapidly when the segmentation quality should approach 100%.

Therefore, we present a method that asks for user input more intelligently, by actively querying image regions to be labeled where the classification was made with high uncertainty. This way, the amount of user input needed to obtain a high quality segmentation is significantly reduced. While this approach seems unnecessary for a single image, where the user immediately can recognize image regions that were not correctly classified, the proposed approach is well suited for large datasets, where a manual inspection of the classification result is not feasible. To obtain an accurate classification uncertainty estimate, we use a Gaussian Process classifier (GPC) to learn a background and foreground model. For increased runtime performance, we use an efficient sparse version of the GPC.

7.1.1. Related Work

Since the work of Boykov *et al.* [19], many approaches, e.g. [94, 120], have been proposed to compute a segmentation based on the graph cut framework. Another line of research [102, 147] formulates the image segmentation problem on a continuous domain and uses the convex relaxation of Chan *et al.* [25]. In both approaches, the solution is regularized by a boundary length regularizer, that favors a spatially smooth solution.

This work is related to the approach of [102], where the data term that describes the pixel-wise probability distribution for foreground and background includes both information about the color distribution and in addition spatial information by using a Parzen window estimator. Here we instead propose to use an Informative Vector Machine (IVM) [88], a sparse version of the Gaussian Process Classifier, and propose to use active learning to improve the classifier in an interactive segmentation setup.

The Informative Vector Machine achieves a sparsification of the GP classifier by selecting only a sub-set of the training data based on an information theoretic criterion. The sparse training set is iteratively constructed from the larger training set, by selecting samples that are most informative with respect to the expected information gain. Csató and Oppér [30] also proposed a sparse GP algorithm. However, they form the sparse subset by minimizing the KL-divergence between the approximate posterior defined by the full training set and the posterior achieved by the sparse representation. We choose the IVM, due to its information-theoretic selection criterion that can be directly leveraged for active learning [142].

Active learning methods have been proposed for other classification tasks, *e.g.* Kapoor *et al.* [75] propose to use a Gaussian process classifier (GPC) for object categorization and improve the classifier by querying labels for data points with large classification uncertainty. Here we use a similar approach to the work of Triebel *et al.* [142], who uses an IVM in an active learning framework for traffic light detection in urban traffic images.

Recently, Vezhnevets *et al.* [149], as well as Wang *et al.* [151], also propose to use active learning for interactive image segmentation. However they use either a conditional

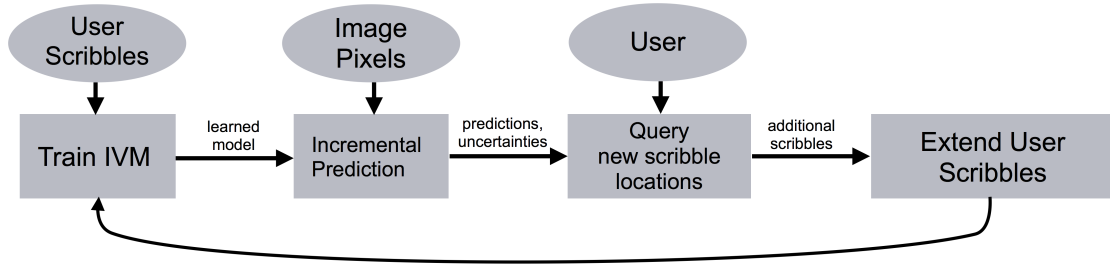


Figure 7.1.: Flowchart of our active learning framework. Starting from an initial set of user scribbles, a sparse GP classifier is trained and the remaining image pixels are classified. The obtained class predictions are analyzed with respect to their uncertainty estimates. Then, new user scribbles are queried at locations that are randomly sampled, with probabilities proportional to the classification uncertainties. The newly added user scribbles are added to the training data, and the next training round begins. *Figure used with kind permission of Rudolph Triebel.*

random field model with a naive Bayes classifier [149], or a Gaussian Mixture Model (GMM) [151]. Instead, we favor to use a Gaussian process classifier which provides very accurate uncertainty estimates [111], and use these uncertainty estimates for actively querying additional training data, which allows to quickly improve the classification result.

7.2. Algorithm Overview

A typical sequence of our active learning framework for interactive segmentation is depicted in Fig. 7.2. From the initial user input, a set of labeled pixels (Fig 7.2a) of both foreground and background, the Gaussian process classifier is trained. Then this classifier is used to estimate foreground and background probabilities for the remaining pixels of the image. The resulting segmentation of the image using this initial training set for classification is shown in Fig. 7.2b.

To improve the segmentation, first an uncertainty measure is computed from the predictive variance returned by the Gaussian process classifier. The benefit of the Gaussian process classifier is, that its uncertainty estimates are more reliable than those produced by other classifiers such as Support Vector Machines, where reliability of uncertainty estimates corresponds to a strong correlation between uncertain and incorrectly classified samples (see, e.g., [111]). To be able to present meaningful parts of the image to the user, we compute a partition of the image into larger regions, called "super pixels", using the method of [44]. For each segment, we compute the average classification uncertainty (see Fig. 7.2c) and select the segment with the highest uncertainty to query a ground truth label from the user. After the user has assigned a label to this image region, a set of pixels is uniformly sampled from the region and, together with the obtained label, added to the training data set (see Fig. 7.2d). In some cases, a segment can contain both foreground and background of the scene. In that case, the user can select a "don't know" option. Then the next segment with the next highest classification uncertainty is selected. However, this occurs only rarely in practice and can be avoided by computing a super pixel segmentation with sufficiently small regions. As last step of the active learning cycle the classifier is updated with the extended training set.

Above active learning round is iterated, either for a fixed number of iterations or until the classification uncertainty has become sufficiently small (Fig. 7.2e and 7.2f).

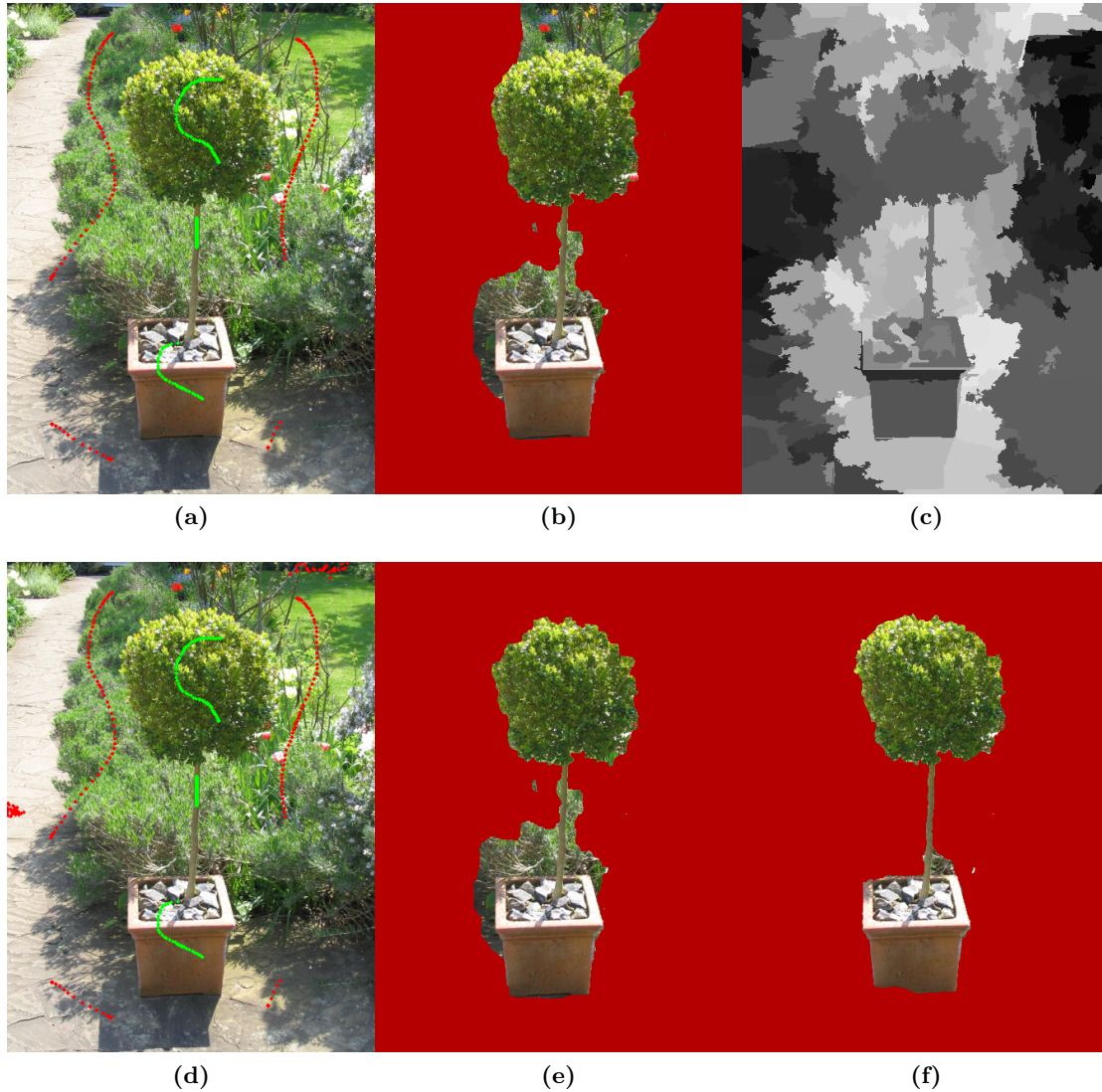


Figure 7.2.: Example sequence of our proposed active learning framework. The algorithm starts with initial user input as shown in (a). A sparse GP classifier is trained and the image is segmented using the GP prediction and a total variation spatial smoothness prior (b). Then, candidate regions for new, informative labels are computed (c). These are based on the normalized entropy of the GP prediction, where bright regions represent a higher classification uncertainty than darker regions. In this case, the segment with highest uncertainty at the upper right border is chosen. A label is queried for this region, here it is background, and a sub-set of uniformly sampled pixels in this region is added to the training data (d). In the next round, the classification is improved and the result is refined (e). After a few rounds, here 4 in total, the final segmentation is obtained (f).

7.3. Gaussian Process Classification

In every round of the active learning algorithm, the Gaussian Process Classifier (GPC) is trained on the current training set. This set consists of user scribbles, these are user defined pixel locations in the image and their respective labels. We represent the training set as pairs $(\mathbf{x}_1, y_1), \dots, (\mathbf{x}_N, y_N)$, where \mathbf{x}_i are feature vectors and $y_i \in \{-1, 1\}$ are binary labels denoting background or foreground. In our implementation, we use a combination of image coordinates and RGB color values of the pixels as feature vector \mathbf{x}_i , but our active learning method can easily extend to higher level features, for example the output of special feature detectors. The use of image coordinated is motivated by the work of Nieuwenhuis and Cremers [102], to which we compare our method in the experimental section.

Once the classifier is trained we can compute $p(y_* = 1 \mid \mathcal{X}, \mathbf{y}, \mathbf{x}_*)$, the *predictive distribution* of an unseen pixel/label pair (\mathbf{x}_*, y_*) , where \mathcal{X} are the feature vectors in the training set and \mathbf{y} are the labels in the training set. In a Gaussian Process Classifier, the predictive distribution is computed by first estimating a distribution $p(\mathbf{f} \mid \mathcal{X}, \mathbf{y})$ over the *latent variables* $\mathbf{f} \in \mathbb{R}^N$. This distribution is approximated by a multivariate normal distribution with mean $\vec{\mu}$ and covariance matrix Σ , i.e.: $p(\mathbf{f} \mid \mathcal{X}, \mathbf{y}) \approx \mathcal{N}(\mathbf{f} \mid \vec{\mu}, \Sigma)$ using Bayes' rule:

$$p(\mathbf{f} \mid \mathcal{X}, \mathbf{y}) = \frac{p(\mathbf{y} \mid \mathbf{f})p(\mathbf{f} \mid \mathcal{X})}{\int p(\mathbf{y} \mid \mathbf{f})p(\mathbf{f} \mid \mathcal{X})d\mathbf{f}}, \quad (7.1)$$

where $p(\mathbf{f} \mid \mathcal{X}) = \mathcal{N}(\mathbf{f} \mid \vec{0}, K)$ is the prior of the latent variables, and

$$p(\mathbf{y} \mid \mathbf{f}) = \prod_i p(y_i \mid f_i) \quad (7.2)$$

are the likelihoods, which are conditionally independent. These likelihoods are given by *sigmoid function* Φ , i.e. $p(y_i \mid f_i) = \Phi(y_i f_i)$, from which it follows that Eq. (7.1) cannot be computed in closed form. Instead, these likelihoods are commonly approximated with Expectation Propagation (EP). This approximation yields a Gaussian distribution $q(y_i \mid f_i)$ that minimizes the Kullback-Leibler (KL) divergence between $q(\mathbf{y} \mid \mathbf{f})p(\mathbf{f} \mid \mathcal{X})$ and the numerator of Eq. (7.1).

At test time, the GP classifier computes for a given new data point \mathbf{x}_* the mean μ_* and the variance σ_*^2 of the latent variable distribution

$$p(f_* \mid \mathcal{X}, \mathbf{y}, \mathbf{x}_*) = \int p(f_* \mid \mathcal{X}, \mathbf{x}_*, \mathbf{f})p(\mathbf{f} \mid \mathcal{X}, \mathbf{y})d\mathbf{f}. \quad (7.3)$$

Given the distribution of the latent variables, the predictive distribution can be modeled as

$$p(y_* = 1 \mid \mathcal{X}, \mathbf{y}, \mathbf{x}_*) = \int \Phi(f_*)p(f_* \mid \mathcal{X}, \mathbf{y}, \mathbf{x}_*)df_*. \quad (7.4)$$

When choosing Φ as the cumulative Gaussian function, the prediction can be computed in closed form using

$$p(y_* = 1 \mid \mathcal{X}, \mathbf{y}, \mathbf{x}_*) = \Phi\left(\frac{\mu_*}{\sqrt{1 + \sigma_*^2}}\right). \quad (7.5)$$

7.3.1. Information-theoretic Sparsification

A drawback that limits the practical applicability of Gaussian Process Classifiers is their huge demand of memory and runtime. The high computational complexity of the method

is due to the $N \times N$ covariance matrix that has to be maintained, where N is the number of samples in the training set that can be very large in practice. Therefore, we use a sparse version of the Gaussian Process Classifier, the Informative Vector Machine (IVM) [89]. This sparsification is achieved by only using a sub-set of the training data, the so called *active set* \mathcal{I}_D , which is used to compute an approximation q of the posterior. As in the original Gaussian Process Classifier, q is Gaussian, i.e. $q(\mathbf{f} | \mathcal{X}, \mathbf{y}) = \mathcal{N}(\mathbf{f} | \vec{\mu}, \Sigma)$. The IVM computes the vector $\vec{\mu}$ and the covariance matrix Σ incrementally, i.e. in every step j a new $\vec{\mu}_j$ and Σ_j are computed:

$$\vec{\mu}_j = \vec{\mu}_{j-1} + \Sigma_{j-1} \mathbf{g}_j \quad (7.6)$$

$$\Sigma_j = \Sigma_{j-1} - \Sigma_{j-1} (\mathbf{g}_j \mathbf{g}_j^T - 2\Gamma_j) \Sigma_{j-1} \quad (7.7)$$

where

$$\mathbf{g}_j = \frac{\partial \log Z_j}{\partial \vec{\mu}_{j-1}}, \quad \Gamma_j = \frac{\partial \log Z_j}{\partial \Sigma_{j-1}}, \quad (7.8)$$

and Z_j is an approximation to the denominator in Eq. (7.1) using the estimate q_j . Initially, we set $\vec{\mu}_0 = \vec{0}$, and $\Sigma_0 = K$, where K is the prior GP covariance matrix.

At every iteration, a new training point (\mathbf{x}_k, y_k) that maximizes the entropy difference between q_{j-1} and q_j is added to the active set, until the active set has reached a desired size D . In our experiments, we defined this size as a fixed fraction of the size of the training set N .

Because both \mathcal{I}_D and the kernel hyper parameters θ depend on each other, the training algorithm of the IVM iterates several times over two steps: estimation of the active set \mathcal{I}_D from θ and, for this given active set \mathcal{I}_D , minimizing the *marginal likelihood* Z_D using $\partial Z_D / \partial \theta$. Although there is no guaranteed convergence, in practice only a few iterations are needed to find good kernel hyper-parameters.

7.4. Online Update of the IVM

The IVM differs from the standard GP not only in its sparsity, it also allows to compute an efficient update of the posterior distribution $p(\mathbf{f} | \mathcal{X}, \mathbf{y})$ *incrementally*. In every iteration of the IVM, new elements are added to the active set and thus the size of the mean vector $\boldsymbol{\mu}$ and covariance matrix Σ increases in every iteration. In the IVM, the covariance matrix Σ is efficiently represented by a lower triangular matrix L of a Cholesky decomposition. Further details of this approach are given in Algorithm 1 of Lawrence *et al.* [89].

For our user interactive approach this incremental scheme is particularly useful, as it avoids the computation of the complete covariance matrix. In contrast to the standard GP, we do not need to update the whole covariance matrix when adding new elements to the active set, instead in every training round only a fixed number of rows and columns is added to the lower triangular matrix L . This reduces the amount of time needed in each subsequent training round substantially, as we show in our experiments (Fig. 7.4b). Furthermore, we propose an efficient update rule for *class prediction*.

7.4.1. Efficient Online Computation of the Class Prediction

In every active learning round, the super pixel with the highest classification uncertainty given the current active set of the IVM has to be found. To estimate this classification

uncertainty, we need to compute the class probabilities of each candidate pixel \mathbf{x}_* contained in a super pixel. This step we call *prediction step*, in contrast to the training of the classifier described above. Therefore, one seeks to predict the class label y_* with highest probability for a given test data point \mathbf{x}_* . In the framework of the IVM, this prediction amounts to compute the mean μ_* and the covariance σ_* of the approximation (Eq. (7.5)) to the latent variable distribution (Eq. (7.3)).

Using the notation of Rasmussen and Williams [116] the computation of μ_* and σ_* for a new candidate data point \mathbf{x}_* is given by

$$\mu_* = \mathbf{k}_*^T (K + \tilde{\Sigma})^{-1} \tilde{\boldsymbol{\mu}} \quad (7.9)$$

$$\sigma_* = k(\mathbf{x}_*, \mathbf{x}_*) - \mathbf{k}_*^T (K + \tilde{\Sigma})^{-1} \mathbf{k}_*, \quad (7.10)$$

where $\mathbf{x}_1, \dots, \mathbf{x}_N$ denote the set of points in the training set, $\tilde{\boldsymbol{\mu}}$ and $\tilde{\Sigma}$ are the *site parameters* of the approximate Gaussian likelihood $q(\mathbf{y} | \mathbf{f})$, and the matrix K is the prior covariance matrix, i.e. the kernel function k applied to all pairs of $\mathbf{x}_1, \dots, \mathbf{x}_N$, and $\mathbf{k}_* = (k(\mathbf{x}_*, \mathbf{x}_1) \dots, k(\mathbf{x}_*, \mathbf{x}_N))$. Because we use the sparse representation above quantities are only computed for the active set of $D < N$ points.

In the following, we describe an efficient online prediction scheme, which allows for a significant speedup when computing above quantities. In a naive implementation, Eqs. (7.9) and (7.10) would have to be recomputed completely anew for every candidate data point \mathbf{x}_* . However, the matrix $B := K + \tilde{\Sigma}$ increases in every round and thus the computational complexity of computing the prediction step scales quadratically with the size of the active set.

To speed up the computation of the prediction step, we utilize the following two redundancies in the computation: First, the active set of subsequent active learning rounds always contains the active set of any previous round, and second, the set of test pixels \mathbf{x}_* is a subset of the test pixels in the previous round. Thus the vector $\mathbf{k}_{*,t}$ from round t can be computed by taking the vector $\mathbf{k}_{*,t-1}$ of the previous round and appending the covariances $k(\mathbf{x}_*, \mathbf{x}_{D_{t-1}+1}) \dots, k(\mathbf{x}_*, \mathbf{x}_{D_t})$ between \mathbf{x}_* and the newly added data points in the active set, where D_t is the total number of active points in round t .

We will now show how this iterative structure can be used to compute $\mu_{*,t}$ and $\sigma_{*,t}$ incrementally from $\mu_{*,t-1}$ and $\sigma_{*,t-1}$. First note that in the IVM approach, the matrix $B_t := K_t + \tilde{\Sigma}_t$ is characterized by its Cholesky decomposition $L_t L_t^T$, and

$$L_t := \begin{pmatrix} L_{t-1} & 0 \\ A & L_+ \end{pmatrix}, \quad (7.11)$$

where L_{t-1} is the lower-triangular Cholesky factor from the previous iterate, and L_+ is a lower-triangular matrix, with as many rows and columns as the number of points that have been added to the active set in the current active learning round t . For the parameters of the approximate prediction Eqs. (7.9) and (7.10), we have to compute the inverse matrix B_t^{-1} . We use the Cholesky decomposition of $B_t = L_t L_t^T$ and write the inverse matrix as

$$B_t^{-1} = \begin{pmatrix} L_{t-1} L_{t-1}^T & L_{t-1} A^T \\ A L_{t-1}^T & A A^T + L_+ L_+^T \end{pmatrix}^{-1}. \quad (7.12)$$

Given this block-wise Cholesky decomposition, we compute the Schur complement as

$$S = A A^T + L_+ L_+^T - A L_{t-1}^T (L_{t-1} L_{t-1}^T)^{-1} L_{t-1} A^T = L_+ L_+^T.$$

With the Schur complement, we can express the inverse matrix B_t^{-1} as

$$B_t^{-1} = \begin{pmatrix} C & -L_{t-1}^{-T}A^T S^{-1} \\ -S^{-1}AL_{t-1}^{-1} & S^{-1} \end{pmatrix}, \quad (7.13)$$

where $C = (L_{t-1}L_{t-1}^T)^{-1} + L_{t-1}^{-T}A^T S^{-1}AL_{t-1}^{-1}$.

The covariance of the approximate prediction Eq. (7.10) can be expressed as

$$\sigma_* = k(\mathbf{x}_*, \mathbf{x}_*) - \begin{pmatrix} \mathbf{k}_{*,t-1} & \mathbf{k}_{*,+} \end{pmatrix} B_t^{-1} \begin{pmatrix} \mathbf{k}_{*,t-1} \\ \mathbf{k}_{*,+} \end{pmatrix}, \quad (7.14)$$

where $\mathbf{k}_{*,+}$ is the vector of covariances of newly added points in the active set. We insert Eq. (7.13) into Eq. (7.14) and get for the rightmost term r of Eq. (7.14)

$$r = \hat{\mathbf{k}}_{t-1}^T \hat{\mathbf{k}}_{t-1} + \hat{\mathbf{k}}_{t-1}^T A^T S^{-1} A \hat{\mathbf{k}}_{t-1} - 2\hat{\mathbf{k}}_{t-1}^T A^T S^{-1} \mathbf{k}_{*,+} + \mathbf{k}_{*,+}^T S^{-1} \mathbf{k}_{*,+}, \quad (7.15)$$

where $\hat{\mathbf{k}}_{t-1} = L_{t-1}^{-1} \mathbf{k}_{*,t-1}$.

We observe that the first term of r in Eq. (7.15) and the first term in Eq. (7.14) define the predictive variance of the previous round $\sigma_{*,t-1}$

$$\sigma_{*,t-1} = k(\mathbf{x}_*, \mathbf{x}_*) - \hat{\mathbf{k}}_{t-1}^T \hat{\mathbf{k}}_{t-1}, \quad (7.16)$$

whereas the remaining terms of r can be subsumed into

$$(L_+^{-1} \mathbf{k}_{*,+} - L_+^{-1} A \hat{\mathbf{k}}_{t-1})^T (L_+^{-1} \mathbf{k}_{*,+} - L_+^{-1} A \hat{\mathbf{k}}_{t-1}), \quad (7.17)$$

which we simplify to

$$(L_+^{-1} \Delta \mathbf{k})^T (L_+^{-1} \Delta \mathbf{k}), \quad (7.18)$$

with $\Delta \mathbf{k} = \mathbf{k}_{*,+} - A \hat{\mathbf{k}}_{t-1}$.

By this decomposition, we achieved an efficient way to compute $\sigma_{*,t}$ iteratively: We store $\hat{\mathbf{k}}_{t-1}$ from the previous round and compute $\Delta \mathbf{k}$ and $L_+^{-1} \Delta \mathbf{k}$ for the newly added points. Then we multiply the result with itself (Eq. (7.18)) and subtract it from $\sigma_{*,t-1}$. Similarly, $\mu_{*,t}$ can be computed from $\mu_{*,t-1}$ of the previous round using the difference vector $\Delta \boldsymbol{\mu} := \boldsymbol{\mu}_{*,+} - A \hat{\boldsymbol{\mu}}_{t-1}$, where $\hat{\boldsymbol{\mu}}_{t-1} = L_{t-1}^{-1} \tilde{\boldsymbol{\mu}}_{t-1}$.

To summarize, the online update scheme for the prediction step becomes

$$\mu_{*,t} = \mu_{*,t-1} + (L_+^{-1} \Delta \boldsymbol{\mu})^T (L_+^{-1} \Delta \mathbf{k}) \quad (7.19)$$

$$\sigma_{*,t} = \sigma_{*,t-1} - (L_+^{-1} \Delta \mathbf{k})^T (L_+^{-1} \Delta \mathbf{k}). \quad (7.20)$$

With this we can efficiently compute the approximate class prediction Eq. (7.5) for a candidate data point \mathbf{x}_* .

7.5. Segmentation Model

The IVM allows to infer predictions for the foreground and background class probabilities for a given image location. However, these estimates are only based on the local feature vector. To allow a consistent segmentation of the image with smooth object boundaries, we use the boundary length regularized image segmentation model from the previous chapters. We formulate the image segmentation problem according to(3.9) as

$$\min_{S \subseteq \Omega} \int_S f(x) dx + \lambda \text{Per}_\alpha(S, \Omega), \quad (7.21)$$

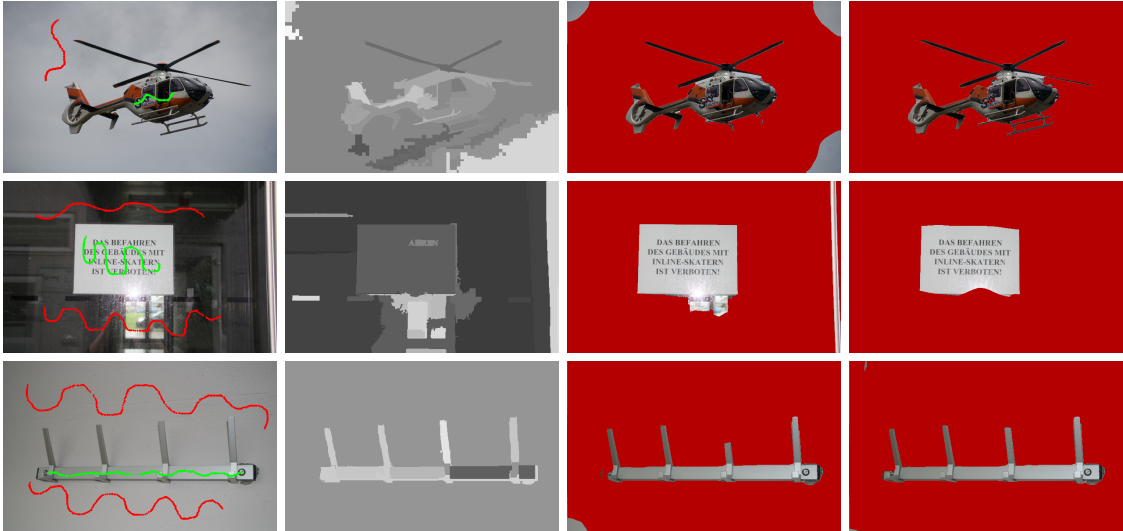


Figure 7.3.: Evaluation of our algorithm on the Graz benchmark. **Left column:** input image with initial user scribbles. **Second column:** classification uncertainties after the first learning round. **Third column:** resulting segmentation after the first round. Note that some small areas are misclassified, but the classification in those same areas is often very uncertain (see, e.g., the third peg on the wardrobe). Thus, the errors can be corrected by querying more useful, i.e. informative user scribbles. **Right column:** final segmentation results, obtained after a few further active learning rounds (betw. 1 - 5). Here, a segmentation of high-quality is obtained.

where $Per_\alpha(S, \Omega)$ measures the perimeter of S in Ω weighted by a local metric $\alpha(x) = e^{-\gamma|\nabla I|}$ that depends on the image gradient.

The probabilistic model of the IVM is included with

$$f(x) = \log \frac{p(y_* = -1 \mid \mathcal{X}, \mathbf{y}, \mathbf{x}_*)}{p(y_* = 1 \mid \mathcal{X}, \mathbf{y}, \mathbf{x}_*)}. \quad (7.22)$$

As in the previous chapters, we use the convex representation of Chan *et al.* [25] and define a continuous indicator function $u : \Omega \mapsto [0, 1]$ and get the convex optimization problem

$$\min_{u: \Omega \rightarrow [0,1]} \int_{\Omega} f(x) u(x) \, dx + \lambda \int_{\Omega} \alpha(x) |\nabla u(x)| \, dx, \quad (7.23)$$

which can be minimized with the primal-dual hybrid gradient method, see [23, 24, 113, 114] and Section 2.5.

7.6. Experimental Results

To allow a comparison to the most related work of Nieuwenhuis and Cremers [102], we also use the benchmark data set from the University of Graz [123] for evaluation. The data set consists of images with predefined user scribbles and a ground truth segmentation for every image. Because we implemented our method for two class image segmentation we chose a subset of 44 images from the dataset which contain only two object classes.

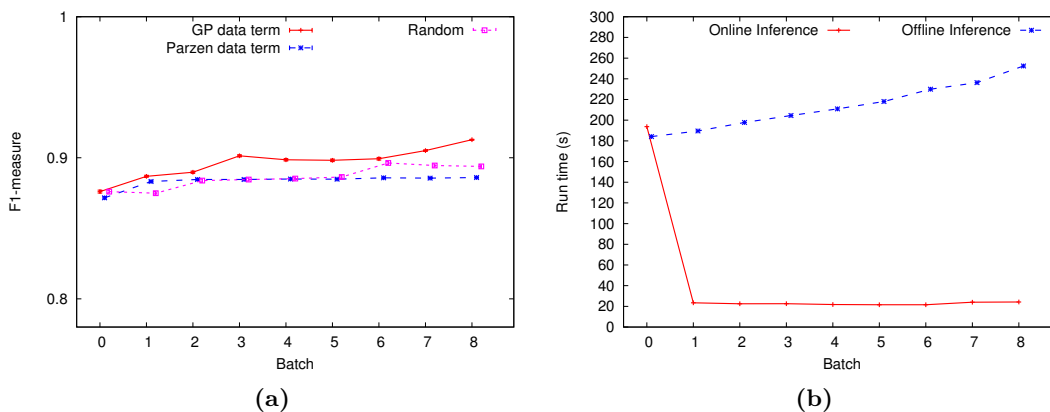


Figure 7.4.: (a) Average f-measure over 8 active learning rounds. The GPC steadily improves the segmentation, because its label queries are more informative for classification. In contrast, the Parzen window estimator only improves slightly and then remains at a lower performance level. As a baseline comparison, we also show GPC results where new user scribbles are chosen randomly and not based on the classification uncertainty. This also improves the segmentation, as it increases the amount of training data, but it does not improve the result as quickly as the GPC with uncertainty based sampling. (b) Run time of online and offline inference, averaged over all images. Note that in the beginning, the online and the offline method take the same time, because they both need to compute the initial covariance matrix. However, in later steps the online computation time drops down significantly.

7.6.1. Benefits of the GP classifier

In the work of Nieuwenhuis and Cremers [102] the data term is computed using a Parzen window (PW) estimator, and the feature vector consists of the RGB color channel and the position of a scribbles. We use the same idea and also use the RGB-color value and the image coordinates as feature vector. In contrast to [102], we employ a Gaussian Process Classifier instead of the Parzen window estimator, with the benefit that misclassifications can be detected using the predictive uncertainty, which is more strongly correlated to incorrect classifications than for the Parzen windows estimator. We validate this assumption by performing the active learning approach on the Graz data set (Fig. 7.4). As a result, in active learning the GPC generates more informed questions.

Both approaches, the Gaussian Process Classifier (GPC) and the Parzen window estimator (PW), perform equally well in the first active learning rounds, but then the GPC (red curve) outperforms the PW (blue curve), because it asks more informed label queries. As a baseline comparison, we also show the result for randomly selected scribbles (magenta curve) instead of those with the highest uncertainty. We see that random sampling also improves the classification, as it provides more training data in every round, but the improvement is smaller compared to selecting the most uncertain image region.

Representative results from the Graz data set are shown in Fig. 7.3. The left column shows the images with the initial user scribbles. Columns two and three show the uncertainties of the GPC, where brighter is more uncertain, and the segmentation after the first learning round. The general segmentation quality is good, already after the first learning round, but some small misclassifications occur. However, these often correspond to locations of high uncertainty, e.g. the lower right corner of the helicopter image or the third peg on the wardrobe: here the classification is incorrect, but the uncertainty is also high. This allows to correct for these misclassified regions in subsequent training rounds.

Table 7.1.: Dice and F-Measures on the Graz benchmark. Already after 4 active learning rounds our method produces as accurate results as the segmentation method of [102].

Batch	Dice	F-Measure			
1	0.890	0.845	5	0.923	0.898
2	0.910	0.875	6	0.928	0.904
3	0.917	0.887	7	0.932	0.908
4	0.920	0.894	8	0.936	0.913
[102]	0.920	0.882			

We quantitatively compare our method to the method of Santner *et al.* [123] and Nieuwenhuis and Cremers [102], and report the dice-score in Table 7.1. The dice score is the relation between the overlap of each segmented region with the ground truth and the sum of their areas. In addition we present the f-measure of our results, which is defined as the harmonic mean of precision and recall.

7.6.2. Advantage of the Online Inference Algorithm

As described in Section 7.4.1, we use a very efficient online class prediction step. In Fig. 7.4b we show its benefit in comparison to the standard offline technique. While in the first learning round, both methods have to compute the full covariance matrix for the initial training set, and thus show comparable run time, the online prediction approach is much more efficient and has a constant run time over subsequent batches while the run time of the offline prediction method increases with the amount of training data (as discussed in Section 7.4.1). Both methods are implemented on the CPU in 8 concurrent threads.

7.7. Conclusion

The presented active learning approach for user interactive image segmentation is able to significantly improve the classification performance over several active learning rounds. The method adaptively improves the classifier by informed questions based on the classification uncertainty.

We believe that this approach is particularly useful for the classification of large image data sets, where a manual inspection of the segmentation result is infeasible. Instead, our active learning approach identifies exactly those regions in the image, which have a high classification uncertainty and which are likely to be misclassified. This enables a user interactive validation and improvement of image segmentation of large image data sets.

Part III.

3D Reconstruction and Tracking

8. Connectivity Constraints for Image Based 3D Reconstruction

This chapter describes how to introduce connectivity constraints into spatio-temporal multiview reconstruction. In the previous part of the thesis, the connectivity constraint was introduced for the task of image segmentation: the labeling of an image into two different parts, the object and the background. Here we will use a very similar mathematical framework for spatio-temporal multiview reconstruction, which is based on a labeling of a volume into the interior and exterior of the object to reconstruct. The use of this framework allows to adapt the connectivity constraints for image segmentation easily to the task of multiview reconstruction.

We also present an extension of the connectivity constraints: Previously, only connectivity of the object was required. We extend this framework to preserve loops as distinct topological features of the object. This has practical applications in volumetric multiview reconstruction. Starting from the so called visual hull of the object, the intersection of the interior of the silhouettes of the object from all perspectives, in a first step we detect loops in this visual hull and in the subsequent reconstruction step guarantee that these loops stay connected in the final segmentation. The combination of the connectivity constraint with the spatio-temporal multiview reconstruction method of Oswald and Cremers [107] allows a significant improvement in comparison to the state-of-the-art especially for scenes with fine structured details.

The chapter is organized as follows: First, we give an introduction to the spatio-temporal multiview reconstruction method, then we describe the modifications necessary to extend the connectivity prior to allow to preserve loops.

Part of the results presented in this chapter have been published in [108] and [106]. Martin Oswald contributed the implementation of the spatio-temporal reconstruction algorithm. Jan Stühmer developed the theory and methods to include the connectivity constraint and extend it to preserve loops. The final integration of both methods and necessary implementations for analyzing the topology of the visual hull were performed by both authors.

Here, the work presented in [108] is extended by introducing the mathematically more precise notion of *k-connectedness* of the graph spanned by the edges of the constraints. We will see that loop connectivity constraints correspond to *2-connectedness* in comparison to the tree shape priors presented in the previous part of this thesis, which correspond to *1-connectedness* of the constraint graph.

8.1. Introduction

Multi-view 3D reconstruction is one of the classical topics in computer vision research. Given a set of images from different viewpoints the goal is to reconstruct the three dimensional geometry of the scene. Often, the scene consists of a single object one wishes to reconstruct, another application domain is 3D reconstruction from aerial photographs.

State-of-the-art reconstruction algorithms make use of a priori information about the scene, such as smoothness of the surface or shape priors for the object to reconstruct. We will see in the following, how higher level features about the topology of the object can be incorporated into the reconstruction process. To demonstrate the effectiveness of topological constraints for 3D reconstruction we combine our framework for connectivity constraints with a state-of-the-art algorithm for dynamic scene reconstruction: the spatio-temporal reconstruction method of Oswald and Cremers [107].

8.1.1. Contributions

We propose a framework for connectivity constraints in spatio-temporal multi-view reconstruction. Whereas the connectivity constraints developed in the previous part of this thesis allowed to preserve *1-connectedness* on the directed graph defining the constraints, here we extend this framework to allow to preserve loops as topological features, resulting in a *2-connected* constraint graph¹. Because the underlying spatio-temporal multi-view reconstruction approach of [107] is formulated in a convex optimization framework, and the connectivity constraint preserves the convexity, our method allows image based globally optimal 3D reconstruction while preserving connectivity.

8.1.2. Related Work

In their pioneering work for spatio-temporal multi-view reconstruction on dense occupancy grids Goldlücke et al. [56, 57] represent the dynamic scene as a space-time surface using a level set representation. The main drawback of their method is that level set representations only allow for local optimality of the solution, thus their method depends on a good initialization. Another local optimal approach was proposed by Aganj et al. [1]. The scene is also represented as a space-time surface, which is computed as a spatio-temporal Delaunay mesh.

¹Refer to Section 4.2.1 for details on 1- and 2-connectedness.

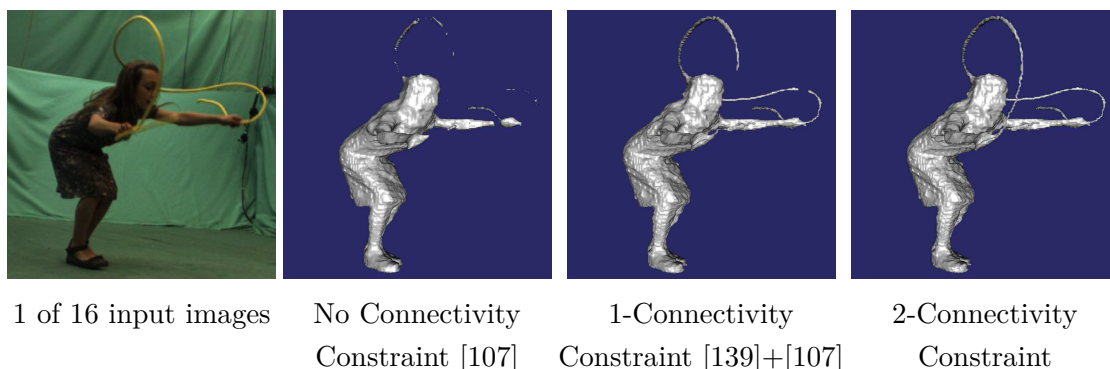


Figure 8.1.: Comparison of reconstruction results with and without connectivity constraints. Connectivity constraints clearly improve state-of-the-art multi-view reconstruction methods and allow to recover fine structures like the rope in this example. The tree-shaped connectivity prior introduced in the previous chapter only enforces connectedness of the object on the tree, thus it is allowed that the rope is disconnected into multiple parts when it touches the head. In the following we will modify the connectivity constraints to allow to preserve loops of the object, which results in a 2-connectivity constraint on the constraint graph. Dataset: 'jumping rope' sequence from the INRIA 4D repository [69].

Starck and Hilton [132] propose to first estimate shapes from silhouettes and in a second step to refine the reconstruction with photometrically matched features together with temporal coherence. Guillemaut and Hilton [60] perform spatio-temporal reconstruction by first computing a multi-layer segmentation of the scene and then assigning a depth value to each layer based on confidence-weighted optical flow.

The spatio-temporal reconstruction method from Oswald & Cremers [107], on which the method presented in this chapter is based on, generalizes the 3D reconstruction framework of Kolev *et al.* [82] to the temporal domain. Similar to the image segmentation methods studied in the first part of this thesis, Kolev *et al.* and Oswald & Cremers represent the scene as the surface of a labeling function and optimize it using a convex optimization framework. This readily enables us to combine their framework with the connectivity constraints for image segmentation and build on top the results from the previous chapters.

To the best of our knowledge there is only one previous work on connectivity in 3D reconstruction, the work of Bleyer *et al.* [13]. They propose to solve for the stereo matching problem by concurrently computing a segmentation of the scene and impose connectivity on each segment of the scene. While we aim for a full 3D reconstruction in the spatial domain, Bleyer's method only computes a stereo matching: the scene is represented by assigning a depth value for every pixel in one of the images. In contrast to full 3D reconstruction, such approaches are also called 2.5D stereo reconstruction methods.

8.2. 3D Reconstruction with Connectivity Constraints

Before we describe our extension of the connectivity constraint, we first give an introduction to spatio-temporal 3D reconstruction. We choose the method of [107], as it encodes the spatio-temporal surface by an implicit indicator function, and is thus very similar to the image segmentation problem studied in the previous chapters. Then we describe how to include the connectivity constraint can be included in their reconstruction framework and verify with experiments on real world data that the constraints help to reconstruct fine-scale details of the scene.

8.2.1. Spatio-temporal Multi-view Reconstruction

This section gives an introduction to the spatio-temporal 3D reconstruction approach of [107]. The task of spatio-temporal 3D reconstruction is formulated as convex optimization problem, which allows to include the connectivity constraints without difficulty. The dynamically changing scene is represented by a hypersurface $\Sigma \subset \mathbb{V} \times \mathbb{T}$ that is embedded in the spatio-temporal product space of the three-dimensional Euclidean space $\mathbb{V} \subset \mathbb{R}^3$ with the time dimension $\mathbb{T} \subset \mathbb{R}_{\geq 0}$. The scene is observed by N static calibrated cameras with projection matrices $\{\pi_i\}_{i=1}^N$. Furthermore, for every image at every time point t we have the approximate silhouettes $\{S_i(t)\}_{i=1}^N$. The method does not need exact silhouettes, which allows to extract the silhouettes automatically, for example by 2D image segmentation or, in case of a controlled background, even simpler methods. Recordings in front of a green or blue screen allow to extract the silhouettes with a method called chroma keying, which is broadly used in television broadcasting. These silhouettes from different perspectives allow to impose geometric and topological constraints on the reconstruction process. The geometric constraint is given by the visual hull $\mathcal{VH}(t) = \bigcap_{i=1}^N \pi_i^{-1}(S_i(t))$ and states that the projections of the reconstructed object into the viewpoint of every camera have to stay within the silhouette $S_i(t)$ of this viewpoint. In the following section

we will also see, how constraints on the topology of the object can be derived from the visual hull.

The hypersurface Σ is represented as the 1-level-set of the binary label function $u : \mathbb{V} \times \mathbb{T} \mapsto \{0, 1\}$, indicating either interior or exterior for every point in space-time. This implicit representation ensures that the surface is a closed, not necessarily connected, manifold without a boundary while allowing arbitrary topologies.

Furthermore, we are given a photoconsistency measure $\rho : \mathbb{V} \times \mathbb{T} \mapsto \mathbb{R}_{\geq 0}$, that describes a measure for a point in space-time for being on the surface of the object, as well as a data term $f : \mathbb{V} \times \mathbb{T} \mapsto \mathbb{R}$ that expresses an affinity to an interior ($f < 0$) or an exterior ($f > 0$) labeling.

We are now able to formulate the space-time reconstruction problem as an energy minimization problem which amounts to finding a surface of minimum area, where this area is weighted by the local photo-consistency, such that a smaller weight corresponds to higher agreement with the image data. We combine this problem of finding a minimum surface with the region based data term and get the energy minimization problem

$$E(u) = \int_{\mathbb{V} \times \mathbb{T}} f u \, dx \, dt + \lambda \int_{\mathbb{V} \times \mathbb{T}} \left(\rho |\nabla_x u| + g_t |\nabla_t u| \right) \, dx \, dt, \quad (8.1)$$

where $\lambda > 0$ is the weight for a regularizer that measures the smoothness of the reconstructed hypersurface and the function $g_t(x, t) = \exp(-|\nabla f(x, t)|)$ weights the temporal smoothness based on f to allow fast motions.

Following [107], we restrict the solution space of the energy minimization in (8.1) to the visual hull such that the object's outline from every camera viewpoint has to remain inside the visual hull. As a consequence, the visual hull completely contains the interior of the scene.

The photo-consistency measure $\rho(x)$ is a voting scheme that is based on truncated normalized cross-correlation matching scores C_i between neighboring camera pairs:

$$\rho(x) = \exp \left[- \mu \sum_{i \in \mathcal{C}} \underbrace{\delta(d_i^{\max} = \text{depth}_i(x)) \cdot C_i(x, d_i^{\max})}_{\text{VOTE}_i(x)} \right], \quad (8.2)$$

with scaling parameter μ . Together with $d_i^{\max} = \arg \max_d C_i(x, d)$ the delta function δ performs a ray-based denoising of the photo-consistency measures and represents the voting scheme proposed by Hernández and Schmitt [42].

To avoid the empty set as trivial solution of Eq. (8.1), we define a data term based on above voting scheme, and propagate the photometric information from Eq. (8.2) into the volume:

$$f(x, t) = - \ln \left(\frac{1 - P(x \in \text{int}(\Sigma))}{P(x \in \text{int}(\Sigma))} \right), \quad (8.3)$$

where the probability $P(x \in \text{int}(\Sigma))$ for a point x to belong to the interior $\text{int}(\Sigma)$ of the surface Σ depends on the votes along the camera rays $r_i(x, \cdot)$ through the point x :

$$P(x \in \text{int}(\Sigma)) = \prod_{i=1}^N \prod_{j=1}^N \prod_{\text{depth}_i(x) < d \leq d_i^{\max}} \frac{1}{Z_j} \exp \left[-\eta \cdot \text{VOTE}_j(r_i(x, d)) \right]. \quad (8.4)$$

To limit the memory consumption we follow the approach in [107] and solve for a time point t by computing a solution of (8.1) with respect to $t - 1$, t and $t + 1$, thus limiting the number of time points used to estimate a surface to $|\mathbb{T}| = 3$. For each time point a mesh is extracted with the Marching Cubes algorithm [95] at an iso-level of 0.5.

8.2.2. Connectivity Constraints for 3D Reconstruction

In this section we describe how to include the connectivity constraints from the previous part of this thesis in above reconstruction method. We assume that the visual hull is connected. In case it consists of multiple connected components, we apply the proposed approach to each component independently. In spatio-temporal reconstruction, we define the connectivity constraints separately for each time step, which allows topological changes to occur over time. To simplify notation, we omit the temporal dependency in the following.

Connectivity Graph. Following the approach from the previous part of this thesis, we define a geodesic shortest path tree G_s with root s on the interior \mathbb{I} of the visual hull. For each $x \in \mathbb{I}$ inside the visual hull, the tree G_s contains the shortest geodesic paths $\bar{C}_s^x : [0, 1] \mapsto \mathbb{R}^3$, with $\bar{C}_s^x(0) = s$ and $\bar{C}_s^x(1) = x$ that minimizes the geodesic distance \mathcal{D}_s to the root, defined as

$$\mathcal{D}_s(x) = \int_0^1 e^{f(\bar{C}_s^x(t))} dt, \quad (8.5)$$

which integrates over a positive measure that depends on the data term. Obviously, this results in a lower cost for paths through areas with strong support of the data term.

Automated Selection of the Root. To enable an automated processing of large video sequences, we propose an automated selection of the root s . Because the position of the root defines the origin of the star-shaped topology of the reconstructed object, it is desirable to choose a position which is 'central' to the reconstructed object. Thus, we propose to find a position for the root by computing the point which minimizes a spatio-temporal convolution of the data term f with a sufficiently large Gaussian kernel \mathcal{G} :

$$s(t) = \operatorname{argmin}_x \int_{t-1}^{t+1} (f * \mathcal{G})(x, \tau) d\tau \quad (8.6)$$

Minimization of above term ensures that we select a position which has a high probability of being interior. Furthermore, the spatio-temporal convolution allows a smooth change of the position of the root over time while at the same time maximizing the distance to the surface of the object. We depict an example of a shortest path between the automatically selected root node and a leaf node of the tree in Fig. 8.4a.

Constrained Optimization. As we have seen in the previous chapters, the connectivity constraints can be included in the reconstruction process as monotonicity constraints on the labeling function u with respect to the edges E in G_s .

Thus, we include the monotonicity constraints as inequality constraints on the directional derivative $\partial_i u(x, t)_j$ of u along every edge $ij \in E$ and formulate our model for spatio-temporal 3D reconstruction with connectivity constraints as

$$\begin{aligned} \min_{u \in \mathcal{BV}(\mathbb{W}\mathbb{T}; \{0,1\})} \quad & E(u) \\ \text{s.t.} \quad & \partial_i u_j \leq 0, \quad \forall (i, j) \in E \end{aligned} \quad (8.7)$$

where $\mathcal{BV}(\cdot)$ denotes the space of functions with bounded variation [2].

8.3. Loop Connectivity

In the following we will see how a topological analysis of the visual hull allows to derive suitable topological constraints in a fully automated process. Therefore, we first describe how to extend the connectivity constraints introduced in the previous part of this thesis to allow to preserve loops. So far, the proposed connectivity constraint only guarantees that the object is path connected, which means that it is 1-connected on the underlying graph, in the following we will show how the framework can be extended to allow to preserve 2-connectedness on the underlying graph for specific parts of the object. This section is organized as follows: First we describe how the framework is extended to formulate 2-connectivity constraints which allow to require connected cycles in the underlying graph. Then we describe how the topology of the visual hull can be automatically analyzed to identify topological features of the object which should be preserved.

8.3.1. Loop Connectivity Constraints

So far, the connectivity constraint requires that the vertices in the foreground segment induce a 1-connected subgraph on the tree defined by the connectivity constraints: Let $T = (V, E_T)$ denote the tree of the connectivity constraints that are defined along the edge set E_T . Let $u : V \mapsto \{0, 1\}$ be a feasible labeling with respect to the connectivity constraints defined by E_T . The vertices $v \in V$ with label $u(v) = 1$ form the set of vertices inside the foreground segment $\Sigma_u \subseteq V$, thus $\Sigma_u = \{v \in V : u(v) = 1\}$. As shown in Section 5.2.3, Σ_u is connected on T , thus the subgraph $T_\Sigma = T[\Sigma_u]$ induced by Σ_u is connected. However, because T_Σ is a tree, there is only one possible path from the source vertex s to each vertex $v \in T_\Sigma$. This leads us to the following statement about the connectivity of a connected tree.

Proposition 8.3.1. *Let $T = (V_T, E_T)$ be a connected tree with $|V_T| > 2$, then the connectivity of T is exactly 1.*

Proof. Let $v \in V_T$ be an internal vertex of T . We denote all paths through v with the set $\mathcal{P} : \{P \ni v\}$. Because there is only one single path that connects the end vertices of each $P \in \mathcal{P}$, these end vertices are not connected when v is removed. Thus the graph $T \setminus v$ is not connected which concludes the proof. \square

If the object to reconstruct has a more complex topology of a higher genus, and we would like to preserve this topology, this connectivity constraint is not sufficient, as it does not allow to formulate the requirement of connected loops of the object. However, we will see in the following how to extend the constraint to formulate a connectivity constraint for loops, while still using the shortest geodesic path topology.

Proposition 8.3.2. *Let $T = (V_T, E_T)$ be a connected undirected tree and $e = ab$ an edge with $a \in V_T$, $b \in V_T$, and $a \neq b$, that is not in E_T , i.e. $e \notin E_T$. The graph $G = (V_T, E_T \cup \{e\})$ that we get by adding the edge e to T , has a cycle which contains e .*

Proof. The tree T contains the unique connected path P from the root vertex s to a , which we denote with sPa , and the unique path Q from s to b , which we denote with sQb . Because both P and Q originate in s it holds that $V(P) \cap V(Q) \ni s$ and therefore $V(P) \cap V(Q) \neq \emptyset$. There exists a vertex x_i , which is both in $V(P)$ and in $V(Q)$, and for which the adjacent vertex in P , $x_{i+1}^P \in P$, is not in Q , likewise it holds for the adjacent

vertex in Q , $x_{i+1}^Q \in Q$, and $x_{i+1}^Q \notin P$. Then it holds that $x_iPa \cap x_iQb = \{x_i\}$. We form the cycle $x_iPa \cup ab \cup bQx_i$. \square

Thus by adding an additional edge to the tree that connects two vertices which were previously not connected we get a graph which contains a cycle. We will describe in the following, how to define the connectivity constraint on a cycle. For the 1-connectivity constraint on the directed tree, the connectivity constraint was defined as monotonicity constraint of the label function along each path of the tree. The label should not increase when traversing along a directed edge, with each edge pointing into the direction of increasing distance from the root vertex. To get a graph with a cycle from a directed tree, we first discard the directions of the edges and add a cycle to the resulting undirected tree as shown above. Then we assign an arbitrary, but consistent direction to the cycle, that allows to traverse the cycle along the directed edges, we call this an *oriented cycle*.

Proposition 8.3.3. *Introducing a monotonicity constraint of the label function along an oriented cycle results in an equality constraint along the cycle.*

Proof. Let $x_iPa \cup ab \cup bQx_i$ be a directed cycle. We use the definitions of the paths P and Q and the vertices $x_i, x_{i+1}^P \in P$ and $x_{i+1}^Q \in Q$ of the previous proof. Then there is a directed edge from x_i to x_{i+1}^P and a directed edge from x_{i+1}^Q to x_i . The monotonicity along the edge from x_i to x_{i+1}^P implies that $u(x_i) \geq u(x_{i+1}^P)$. The monotonicity along $x_{i+1}^P Pa \cup ab \cup bQx_{i+1}^Q$ implies that $u(x_{i+1}^P) \geq u(x_{i+1}^Q)$, together with the remaining constraint $u(x_{i+1}^Q) \geq u(x_i)$ we get

$$u(x_i) \geq u(x_{i+1}^P) \geq u(x_{i+1}^Q) \geq u(x_i) \quad (8.8)$$

which only holds when all the values of the label function along the cycle are equal. \square

We will now see that above connectivity constraint along a cycle ensures that a cycle is either completely included in the final reconstruction or completely excluded.

Proposition 8.3.4. *Let G denote a directed graph that contains a single undirected cycle. We define the connectivity constraints on G and compute a feasible reconstruction. Either the cycle is preserved in the reconstruction or the cycle is completely excluded. In case the cycle is preserved the connectivity of the reconstruction on G is exactly 2.*

Proof. Let u denote a feasible solution of (8.7) with respect to above constraints. By Proposition 8.3.3 the connectivity constraint results in equality constraints along the cycle P , thus $u_i = c$ for all $i \in V_P$ for some constant c , and monotonicity constraints along the remaining edges. The final reconstruction is achieved by thresholding the solution u with some threshold μ . Either $c \leq \mu$ and the cycle is completely excluded, or $c > \mu$, thus $u_i > \mu$ for all $i \in V_P$ and $P[\Sigma_{\{u > \mu\}}]$ is connected if P is connected, i.e. the cycle is completely included.

What remains to be shown is that $\Sigma_{\{u > \mu\}}$ is 2-connected on G if $c > \mu$. We choose an interior vertex of the cycle $a \in V_P$. By construction, removing a from G results in the cycle free graph $G \setminus \{a\}$, i.e. a tree that is 1-connected, thus G is 2-connected. From Theorem 5.4.1 it follows that $G[\Sigma_{\{u > \mu\}}]$ is connected and because of $c > \mu$ it follows that $P[\Sigma_{\{u > \mu\}}]$ is 2-connected. Taking both statements together it follows that $\Sigma_{\{u > \mu\}}$ is 2-connected on G . \square

Therefore we call the connectivity constraint along a cycle *2-connectivity constraint*.

8.3.2. Handle and Tunnel Loops

In [32], Dey et al. describe a method to automatically analyze the topology of a two-dimensional surface embedded in three dimensional space that allows to extract topological features, specifically the *handles* and *tunnels* of the surface. The surface is embedded in a simplicial complex, a hierarchy of p -simplicies. The surface \mathbb{M} separates the simplicial complex into an interior part \mathbb{I} and an exterior part \mathbb{E} . Both the interior and the exterior part are closed and bounded by the surface, therefore $\mathbb{I} \cap \mathbb{E} = \mathbb{M}$. In the following we will denote the surface of the visual hull with $\mathbb{M} = \partial\mathcal{VH}$, the interior of the visual hull with $\mathbb{I} = \mathcal{VH}$ and the exterior with $\mathbb{E} = (\mathbb{V} \setminus \mathcal{VH}) \cup \partial\mathcal{VH}$.

In [32] the authors study cycles of edges on the surface which form equivalence classes with respect to contraction of the cycle - like a rubber band which can be moved on the surface but not through holes in the surface. We call this equivalence relation $\sim_{\mathbb{M}}$ 'contractible' on the set \mathbb{M} , for example, we denote the relation that a loop $l_1 \subset \mathbb{M}$ is contractible to a loop $l_2 \subset \mathbb{M}$ on the set \mathbb{M} as $l_1 \sim_{\mathbb{M}} l_2$. We use the following definition from [108], which allows to describe topological features of the visual hull:

Handle and tunnel loops [108] A **handle loop** $h \subset \mathbb{M}$ is a cycle of edges on the surface that is contractible in the interior ($h \sim_{\mathbb{I}} 0$) and not contractible on the surface ($h \not\sim_{\mathbb{M}} 0$). A **tunnel loop** $t \subset \mathbb{M}$ is a cycle of edges on the surface that is contractible in the exterior ($h \sim_{\mathbb{E}} 0$) and not contractible on the surface ($h \not\sim_{\mathbb{M}} 0$).

Handle and tunnel loops have the following two important properties: First, both definitions form equivalence classes of loops. Two loops are in the same equivalence class if there exists a continuous transformation between them. Second, the classes of *handle* and *tunnel* loops are dual to each other, for each handle loop there exists a corresponding tunnel loop. Furthermore, a closed surface of genus g has exactly g classes of handle loops and g classes of tunnel loops. We consider one representative loop with approximate minimal geometric length per class and denote them as the set of handle loops $\{h_i\}_{i=1}^g$ and the set of tunnel loops $\{t_i\}_{i=1}^g$. For each hole i of the surface we have a corresponding pair (h_i, t_i) of representative handle and tunnel loops which intersect in at least one point, i.e. $h_i \cap t_i \neq \emptyset$. Figs. 8.2, 8.3, 8.4c show examples of handle and tunnel loops which clearly shows their duality.

Dey et al. propose different algorithms for computing these handle and tunnel loops: In [32] they present a method that is able to process geometries defined by implicit functions, perfectly suited to process the geometry defined by the volumetric labeling function we use here for 3D reconstruction. Also their algorithm allows to compute handle and tunnel loops with approximate minimal length, which is desirable for our purpose of segmenting the handles from the rest of the object. However this method is considerably slower than a recently published algorithm by Dey et al. [31] for meshes. The faster runtime is achieved by using the concept of Reeb graphs to estimate an initial set of handle and tunnel loops and their geometric length is shortened in a subsequent refinement step. Also the method does not require to compute a full 3D tessellation of the scene. Therefore, we extract an iso-surface mesh of the visual hull and use the more efficient method [31] to extract handle and tunnel loops.

Handle Segmentation. In the following, we describe how to segment those parts of the visual hull, called *handles*, which enclose a hole in the surface, a *tunnel*. Once the handles are segmented, we can specify a connectivity constraint for the detected handle, which allows for topological constraints that adapt to the topology of the visual hull.

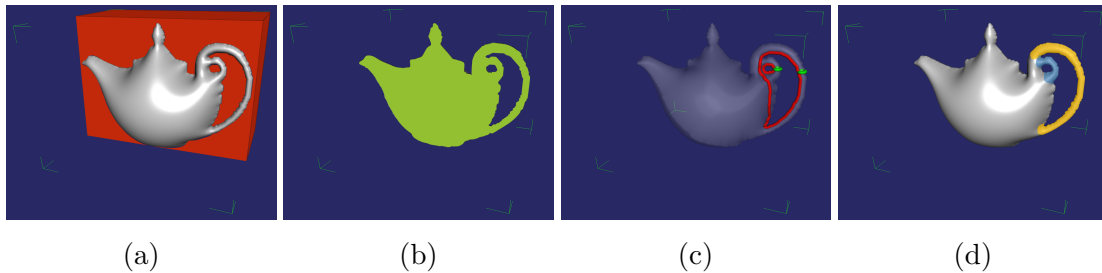


Figure 8.2.: The sets defined in this section are visualized for the surface of a teapot of genus 2. (a) Exterior \mathbb{E} (red), (b) Interior \mathbb{I} (green), (c) Handle and tunnel loops $\{h_1, h_2\}, \{t_1, t_2\}$ (green+red), (d) Handle segments H_1, H_2 (yellow+blue).

To describe the handle segmentation process, we first reproduce the following definitions from [108]:

Handle Segment Surface [108] We define the handle segment surface as the connected subset of all points $x \in \mathbb{M}$ for which a handle loop $h_x \ni x$ exists which is contractible to h_i subject to the additional constraint that the ratio of the lengths of h_x and h_i does not exceed a given threshold σ :

$$\mathbb{M}_{H_i} = \left\{ x \in \mathbb{M} \mid \exists h_x \subset \mathbb{M} : h_x \sim_{\mathbb{I}}^{\sigma} h_i \right\} \quad (8.9)$$

where $h_x \subseteq \mathbb{M}$ with $h_x \ni x$ denotes a handle loop through the surface point x and $h_x \sim_{\mathbb{I}}^{\sigma} h_i$ means that handle loop h_x is contractible to h_i subject to the length ratio constraint $\ell(h_x) < \sigma \ell(h_i)$.

Handle Segment [108] Given the handle segment surface \mathbb{M}_{H_i} from the previous definition, we define the corresponding volumetric handle segment $H_i \subseteq \mathbb{I}$ as the set of all points in the visual hull for which the closest point on the visual hull boundary is on the handle segment surface \mathbb{M}_{H_i} .

$$H_i = \left\{ x \in \mathbb{I} \mid \operatorname{argmin}_{y \in \mathbb{M}} \operatorname{dist}(x, y) \in \mathbb{M}_{H_i} \right\} \quad (8.10)$$

where $\operatorname{dist}(x, y)$ denotes the Euclidean distance between point $x \in \mathbb{I}$ in the interior and point $y \in \mathbb{M}$ on the surface.

To segment the handle H_i , we implement a breadth first search on the visual hull. Beginning at the position where the handle loop h_i takes on its minimum length, a wavefront is propagated on the surface of the visual hull via a breadth first search algorithm. While the wavefront is propagated further on the surface of the handle, eventually the wavefront splits into two parts that move along the handle in opposite directions. Independently for each of the two parts of the wavefront we stop the breadth first search if the ratio between the current length of the wavefront and the length of the minimum handle loop exceeds above threshold σ . Finally, we define the handle segment surface as that part of the surface between the two final positions of the wavefronts, which were reached by the breadth first search. Together with above definition of a handle segment, this procedure yields a segmented handle $H_i \subseteq \mathcal{VH}$ for each handle loop h_i .

With the definition of the handle and tunnel segments of the visual hull we are now able to formulate connectivity constraints to preserve these topological features. Therefore,

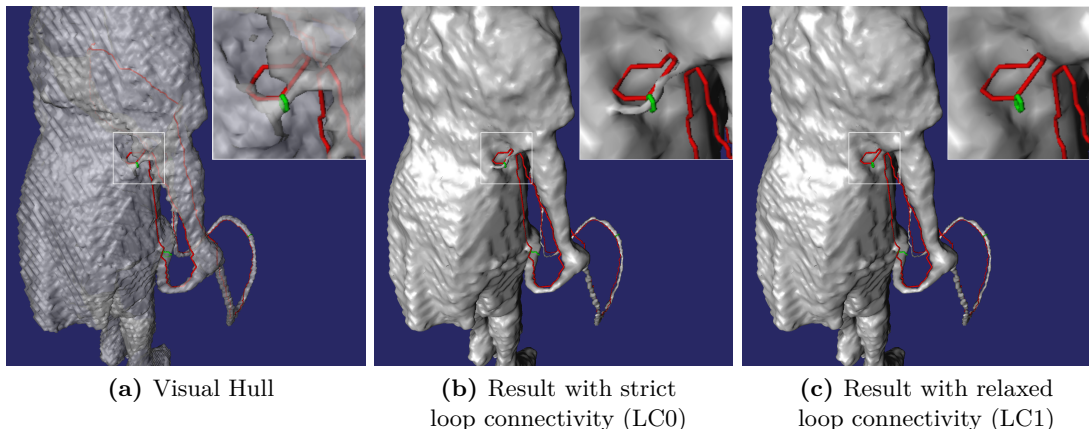


Figure 8.3.: (a) In some cases artifacts of the visual hull can lead to spurious handle loops which should not be preserved in the final reconstruction. (b) The constraint (LC0) strictly preserves all loops in the solution. (c) Relaxing the topology preserving constraint to an equality constraint allows to suppress handles where the photo-consistency is not strong enough. The rope, for which the support of the photo-consistency is sufficient, is still completely preserved. Handle loops are depicted in green and tunnel loops in red.

we define a cycle through the interior of each handle segment as follows: In order to add a minimum amount of cost to the energy (8.7) when enforcing loop connectivity, we need to form a cycle in the graph with minimum cost with respect to the data term. We solve for these geodesic shortest cycles by computing cycles $t_i^{G_s} \subset \mathbb{I}$ using the precomputed geodesic shortest path tree G_s . These cycles need to be *path homotopic* to the original tunnel loop on the surface, i.e. $t_i^{G_s} \sim_{\mathbb{I}} t_i$. For an introduction to path homotopy please refer to the introductory material in section Section 4.1.2. The computation of the minimum cost cycle $t_i^{G_s}$ is discussed later in this section. First we discuss possible definitions of constraints to preserve the topology of the visual hull. For each tunnel loop t_i of the visual hull we define a path homotopic cycle $t_i^{G_s} \sim_{\mathbb{I}} t_i$ and introduce a *loop preserving* constraint along this cycle as

$$\forall i \in [1, \dots, g] : \quad \left\{ \forall x \in t_i^{G_s} : u(x) = 1 \right\}. \quad (\text{LC0})$$

Proposition 8.3.5. [108] *The constraint (LC0) preserves the handle and tunnel loops and thus all holes of the visual hull in the reconstructed object. The topological genus of the reconstructed object is larger or equal to the one of the visual hull.*

Proof. [108] Let us assume that the proposition does not hold. To let the genus of the reconstructed object decrease, either (i) at least one hole of the visual hull needs to be filled or (ii) at least one tunnel loop has to be disconnected in the reconstructed object. Because the domain of the reconstructed object is restricted to the visual hull (i) cannot be fulfilled. By construction (ii) is fulfilled if (LC0) is fulfilled. Therefore the genus of the reconstructed object has to be larger or equal to the genus of the visual hull. \square

However, in some cases it might not be desirable that the reconstruction preserves all handles of the visual hull. An example is depicted in Fig. 8.3 where artifacts in the visual hull lead to a spurious handle loop. For being able to remove such artifacts, for example due to low photometric support by the data term along the handle, we relax the strict loop preservation constraint (LC0) to an equality constraint (LC1) of the labels along the cycle through the handle. As we have seen in Proposition 8.3.3, this corresponds

to the connectivity constraints from the previous chapter, now defined along a cycle. Accordingly, either the handle is preserved in case of sufficient photometric support, or if the support by the data term is not strong enough, the entire handle segment H_i is suppressed. We define this equality constraint as

$$\forall i \in [1, \dots, g] : \left\{ \forall x \in t_i^{G_s} \cap H_i : \frac{d}{ds} u(x) = 0 \right\} \quad (\text{LC1})$$

where $\frac{d}{ds}$ is the directional derivative along the loop $t_i^{G_s}$.

Finding the optimal connected loop $t_i^{G_s}$. For the 1-connectivity constraint we motivated the cost function of the geodesic shortest path tree by looking for a connecting path that adds a low cost to the final segmentation result. For the loop preserving constraints described here, we therefore look for a loop through the handle that adds the minimum cost to the final segmentation. However, to compute this minimum cost path, we don't have to solve another shortest path problem, but instead can utilize the already computed shortest path tree G_s . The shortest loop $t_i^{G_s}$ with respect to G_s can be computed for each handle i by the following steps: Starting from the boundary of a handle segment H_i , we perform a depth first search on G_s and compute the partitions $H_i^1 \cup H_i^2 = H_i, H_i^1 \cap H_i^2 = \emptyset$, which are disconnected on the shortest path tree G_s . We illustrate these partitions in Fig. 8.4d. If one of these partitions is empty, then all points in the handle segment H_i are connected on G_s and no further constraints need to be added in order to preserve the handle segment H_i . Otherwise, there exists an optimal pair of points

$$(p, q) = \underset{(x \in H_i^1, y \in H_i^2, y \in \mathcal{N}(x))}{\operatorname{argmin}} \mathcal{D}_s(x) + \mathcal{D}_s(y) \quad (8.11)$$

which are leaf-nodes in G_s . The set $\mathcal{N}(x)$ denotes the local spatial neighborhood of a point $x \in \mathbb{V}$ in the voxel grid. We add an edge between p and q and form a cycle $t_i^{G_s}$ in G_s , that by construction is in the interior of the handle segment H_i , is path homotopic to the corresponding tunnel loop t_i , and is of minimum cost of all such cycles. We define the set

$$E_{=} := \bigcup_i E(t_i^{G_s}) \quad (8.12)$$

as the set of edges of all minimum cost cycles $t_i^{G_s}$ and define the loop preserving 2-connectivity constraint as

$$\partial_i u_j = 0, \quad \forall (i, j) \in E_{=} \quad (8.13)$$

While the 1-connectivity constraint resulted in a monotonicity constraint, the 2-connectivity constraint corresponds to an equality constraint of the labeling function along the cycle, as shown in Proposition 8.3.3.

8.4. Numerical Optimization

We follow a similar approach as in image segmentation and minimize (8.7) using convex optimization. Therefore we introduce a continuous indicator function $u : \mathbb{V} \times \mathbb{T} \mapsto [0, 1]$ to represent the space-time surface. As in image segmentation, the connectivity constraints are equivalent for the relaxed case.

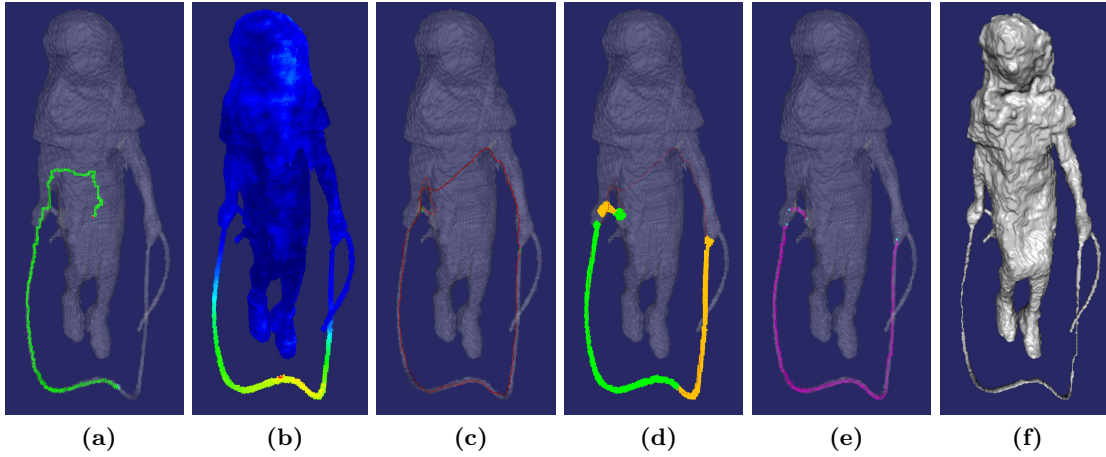


Figure 8.4.: Visualization of different quantities computed from the data term and visual hull. (a) Example shortest path from the source node to a leaf node in the rope (green). (b) Color encoded geodesic distance \mathcal{D}_s with respect to the source node s . (c) Tunnel loop (red), and handle loop (green). (d) Handle segments $H_i = H_i^1 \cup H_i^2$ (green and orange), the color shows the two parts of each handle which are disconnected on the geodesic path tree G_s . (e) Cycle of minimum cost through the handle for which the equality constraints (LC1) are imposed. (f) Final reconstruction result.

Further, we introduce a dual variable $p : \mathbb{V} \times \mathbb{T} \mapsto \mathbb{R}^4$ and write the multiview reconstruction problem Eq. (8.7) as saddle-point problem

$$\begin{aligned} \min_{u: \mathbb{V} \times \mathbb{T} \rightarrow [0,1]} \quad & \max_{\|p\| \leq 1} \int_{\mathbb{V} \times \mathbb{T}} \langle u, -\operatorname{div} p \rangle \, dx \, dt + \lambda \int_{\mathbb{V} \times \mathbb{T}} f u \, dx \, dt. \\ \text{s.t.} \quad & \partial_i u_j \leq 0, \quad \forall (i, j) \in E_T \\ & \partial_i u_j = 0, \quad \forall (i, j) \in E_- \end{aligned} \quad (8.14)$$

The optimization problem is convex in u and concave in p and the constraints on u over the edge sets E_T and E_- are linear. Furthermore, the feasible set defined by the constraints is non-empty, *e.g.* a trivial feasible solution is $u(x, t) = 0$ for all $x \in V$ and $t \in T$, thus Slater's condition holds and we have strong duality (see Section 2.4.1). The constraints can be included in the optimization using Lagrangian multipliers β and γ . The Lagrangian dual associated to problem (8.14) becomes

$$\begin{aligned} \min_{u: \mathbb{V} \times \mathbb{T} \rightarrow [0,1]} \quad & \max_{\substack{\|p\| \leq 1, \\ \beta \geq 0, \\ \gamma}} \int_{\mathbb{V} \times \mathbb{T}} \langle u, -\operatorname{div} p \rangle \, dx \, dt + \lambda \int_{\mathbb{V} \times \mathbb{T}} f u \, dx \, dt \\ & + \int_T \left\{ \sum_{ij \in E_T} \beta_{ij} \partial_i u_j + \sum_{ij \in E_-} \gamma_{ij} \partial_i u_j \right\} dt. \end{aligned} \quad (8.15)$$

We optimize this saddle point problem with the primal-dual hybrid gradient method,

see [23, 24, 113, 114] and Section 2.5, and get the update equations

$$\begin{aligned}
 p^{n+1} &= \Pi_C [p^n + \sigma \nabla \bar{u}^n] \\
 \beta_{ij}^{n+1} &= \Pi_{\geq 0} (\beta_{ij}^n + \mu \partial_i \bar{u}_j^n) \\
 \gamma_{ij}^{n+1} &= \gamma_{ij}^n + \nu \partial_i \bar{u}_j^n \\
 u^{n+1} &= \Pi_{[0,1]} \left[u^n + \tau \left(\operatorname{div} p^{n+1} + \operatorname{div} \beta^{n+1} + \operatorname{div} \gamma^{n+1} - \lambda f \right) \right] \\
 \bar{u}^{n+1} &= 2u^{n+1} - u^n
 \end{aligned} \tag{8.16}$$

where $\Pi_{[0,1]}$ is the projection of u onto the unit interval $[0, 1]$ and $\Pi_{\geq 0}$ projects onto positive values. With Π_C we denote the projection onto the set $C = \{q = (q_x, q_t)^T : \mathbb{V} \times \mathbb{T} \mapsto \mathbb{R}^4 \mid \|q_x\| \leq 1, |q_t| \leq 1\}$, that projects the iterate of the dual variable p on a four dimensional hyperball:

$$\Pi_C(q) = \left(\frac{q_x}{\max(1, \|q_x\|)}, \max(-g_t, \min(g_t, q_t)) \right)^T. \tag{8.17}$$

The step sizes τ , σ , μ and ν are chosen by the preconditioning scheme described in [112]. Because the optimization problem is convex in u , concave in p , and the constraints are linear, above update equations (8.16) converge to a global minimum of the relaxed energy (8.14). It is easy to see that Theorem 5.2.2 also holds for equality constraints. Thus the thresholding theorem also holds in this case and an optimal solution to the binary labeling problem (8.7) can be found by thresholding the minimizer of above relaxed energy ([25, 107] and Theorem 5.2.2).

Implementation. The iterative scheme allows a high degree of parallelization and is implemented on a GPU using the CUDA programming framework. The analysis of the visual hull and the search algorithms for defining the connectivity graph are more difficult to parallelize and therefore are implemented on the CPU.

8.5. Experiments

For evaluation, we performed experiments on several spatio-temporal multi-view data sets of the INRIA 4D repository [69], each consisting of synchronized video recordings of 16 video cameras in a green room environment.

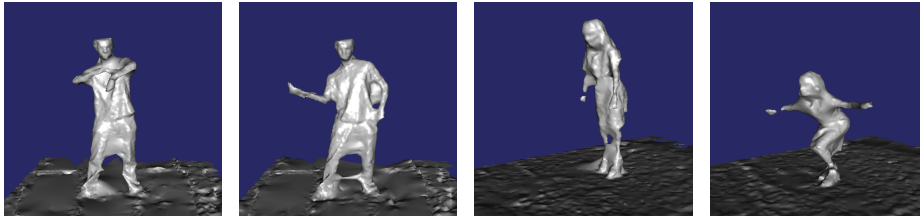
Since there is no ground-truth available, we perform a qualitative comparison of the proposed approach in comparison to the state-of-the-art, however, to the best of our knowledge there is no other 4D reconstruction method publicly available. Thus we compare our results with two state-of-the-art 3D reconstruction methods by evaluating them on the same dataset. The reconstruction methods chosen for comparison are the method by Jancosek and Pajdla [72], and a combination of Furukawa et al. [49] (PMVS) with Poisson surface reconstruction [77]. We use the same approximate silhouettes for the different reconstruction methods, except of the method by Jancosek and Pajdla [72] which does not include any silhouette information. For computing the geodesic shortest path tree G_s we use a regular 6-neighborhood.

Runtime and Memory Resource Evaluation. To encode the connectivity constraint, the memory requirement of the suggested implementation increases only by $|\mathbb{V} \times \mathbb{T}|$

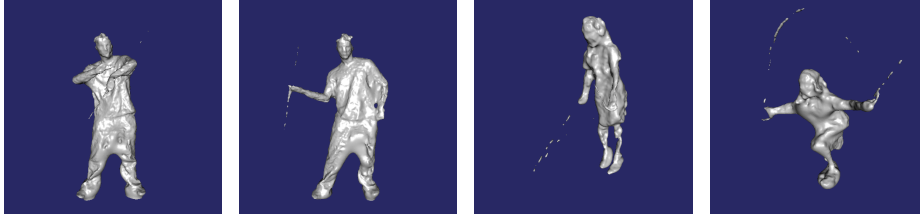
1 of 16 Input Images



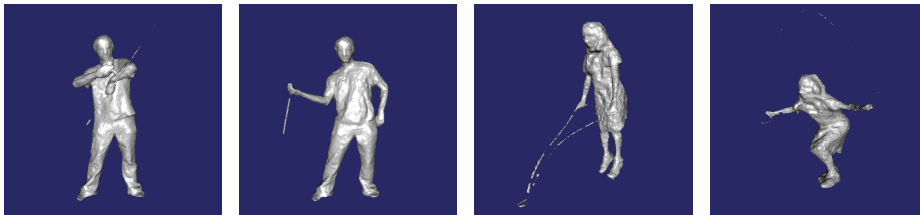
Jancosek and Pajdla [72]



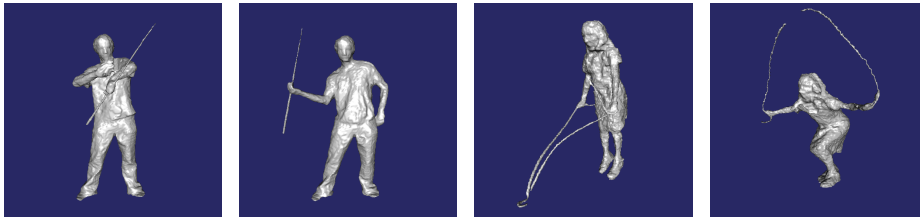
Furukawa et al. (PMVS) [49] + Poisson surface reconstruction [77]



Without Connectivity Constraint [107]



With 1-Connectivity Constraint [139]+[107]



Proposed 2-Connectivity Constraint

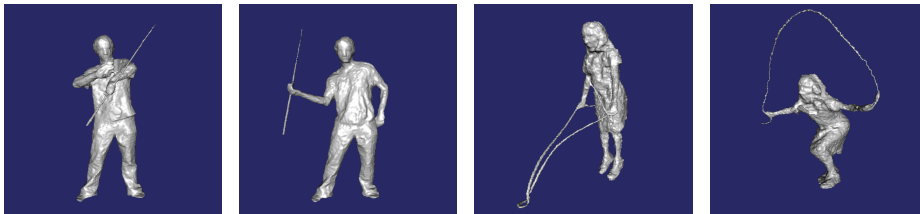


Figure 8.5.: Comparison of the proposed reconstruction method with the state-of-the-art. Existing approaches [49, 72, 77] fail to recover thin structures, in this example the stick and the rope. The 1-connectivity constraint allows to preserve the stick, but for the rope-jump scene, it does not completely preserve the connection of the rope. Our proposed 2-connectivity constraint allows to correctly reconstruct the connected rope (volume resolution $|V| = 384^3$).

bytes in comparison to the original approach. The required runtime per iteration remains almost unchanged, but depending on the length of the connections and the photometric support along the connections, more iterations can be required for sufficient convergence of long connections. However, this can be solved by using a projection scheme similar to the one presented in Chapter 6. Because of the higher memory requirements of the projection method and the large size of the space-time volume used for reconstruction, here we prefer the Lagrange multiplier based approach. All experiments were performed on an Intel Xeon architecture with 24GB RAM and a NVidia GTX Titan graphics card. For the 1-connectivity constraint [139] the amount of time needed per frame for computing the tree was about 20 sec. For the 2-connectivity constraints the precomputation time for handle and tunnel loop detection, handle segmentation and computation of the minimum cost connecting cycle was about 1 min. Minimization of the convex optimization problem needs about 3 min per frame, which results in a total runtime of about 4 minutes per frame when using the 2-connectivity constraints.

8.6. Conclusion

In this chapter we showed how to include connectivity constraints in spatio-temporal multi-view 3D reconstruction. Because the method used for 3D reconstruction is based on a volumetric labeling by convex optimization, the connectivity constraints for image segmentation described in the first part of this thesis can be directly applied in this new context of 3D reconstruction. Furthermore, we showed how to reformulate the constraints to allow to preserve loops of the object. Therefore, we first showed that the connectivity constraints defined on a tree induce a 1-connectedness of the tree, then we extended these constraints to allow to preserve 2-connectedness of cycles in the constraint graph. By analyzing the visual hull of the scene, we can automatically deduce suitable constraints for a scene in a fully automated way. We demonstrate in several experiments on real world data that the connectivity constraints significantly improve the reconstruction in the presence of thin structures. To the best of our knowledge, apart from the work of Bleyer et al. [13], a simplification of connectivity for depthmap estimation, this is the first time that connectivity constraints are described in the context of multi-view 3D reconstruction.

9. The Direct Geometry Approach for Real-Time 3D Reconstruction

In our earlier work [136, 137], we presented a variational approach for online estimation of dense depth maps with a handheld camera. We show that by combining the information from multiple images using the robust ℓ^1 norm in the data term, geometry reconstructions of high quality and detail can be achieved. Here we review this approach and propose several improvements: First, we show that the resulting optimization problem can be solved by introducing dual variables in the data term. In contrast to our previous approach, based on half-quadratic splitting [51], this approach is numerically more stable and the fine tuning of the weight of the quadratic penalty term, the parameter θ in [137], can be avoided. Furthermore the dual variable approach results in a much better runtime performance and allows high quality geometry reconstructions with up to 41.1 frames per second.

Second, we show that minimization of the reconstruction problem by using the dual variable approach leads to staircasing artifacts, a well known drawback of total variation regularizers. However, the previous method that was based on half quadratic splitting never produced these artifacts. We describe the connection between half quadratic splitting, infimal convolution with a quadratic function, and the Huber loss and propose to avoid the staircasing effect by using the robust Huber loss instead of the absolute value function in the regularizer. Experimental results confirm that this allows to achieve 3D reconstructions of a quality that is en par with the earlier results, but with improved numerical stability and better runtime performance.

Early results on the research topic presented in this chapter have been published in [137] and [136]. These early results were also part of the author's Diploma thesis [134]. As extension to the Diploma thesis here we present the dualization of the data term, the connection to infimal convolution, and the Huber loss as robust penalty function in the regularizer.

9.1. Introduction

The three-dimensional reconstruction of the world is one of the classical research topics in computer vision. Several methods have been proposed for offline reconstruction, that even allow to reconstruct full three-dimensional models, *e.g.* [42, 82]. However, real-time capable methods usually only allow to reconstruct a sparse point-cloud [73, 103]. More recent real-time approaches reconstruct a "semi-dense" point cloud [41], but still these methods do not allow a detailed reconstruction of the scene.

In [137] we published our seminal work on real-time dense reconstruction from multiple views. It has inspired a lot of following work, including the online dense 3D reconstruction method *DTAM* [101] of Newcombe et al., who published their earlier work on online reconstruction [99] the same year as our seminal paper for real-time reconstruction. Further methods include the online depth fusion method *Kinectfusion* [100] and

its extension to larger environments *Kintinuous* [154], the semi-dense visual odometry method *LSD-slam* [41], odometry for RGBD cameras [78, 153], and 3D reconstruction on mobile devices [141].

Here we extend our previous work and propose to use the Huber loss instead of the absolute value function for the regularizer. This modified regularizer has already been proposed in the computer vision literature, *e.g.* for semi-automatic terrain model generation from elevation data by Unger *et al.* [146], where the goal is to reconstruct a terrain model where vegetation and man made objects like houses have been removed. Another work using this modified regularizer is the work of Werlberger *et al.* on optical flow estimation [152].

9.2. Dense Depth Map Estimation from Multiple Images

In this section we review the results from [137], where we describe the first method for real-time dense geometry estimation with a handheld camera.

Input to the algorithm is a set of images I_0, \dots, I_m from different viewpoints, in this case single channel radiance images $I_i : \Omega_i \mapsto \mathbb{R}$ but the method should easily extend to color and multi spectral images. Furthermore the camera poses ξ_1, \dots, ξ_m relative to the camera pose of I_0 are assumed to be known. These camera poses can be estimated for example by using a real-time camera tracking method, here we use the feature based method *PTAM* by Klein and Murray [79].

The goal of the algorithm is to robustly estimate a dense depthmap $h : \Omega_0 \mapsto \mathbb{R}$, that assigns a depth value to every pixel of the image I_0 . Robust estimation is achieved by combining the observations from the additional viewpoints and jointly estimating a single depth map that is consistent with all observations. This is achieved by minimizing the following functional, that is inspired by variational optical flow methods, such as the seminal work by Horn and Schunk [67] and the TV-L1 method of Zach *et al.* [159]

$$E(h) = \lambda \int_{\Omega_0} \sum_{i \in \mathcal{I}(x)} |I_i(\pi(\xi_i \circ X(x, h))) - I_0(\pi(x))| dx + \int_{\Omega_0} |\nabla h| dx. \quad (9.1)$$

The term $|I_i(\pi(\xi_i \circ X(x, h))) - I_0(\pi(x))|$ measures the absolute difference of the observed brightness between a pixel in the reference image I_0 and its projected position in an additional view I_i . By taking the sum of absolute differences we achieve robustness of the data term. A reference pixel position $x \in \Omega_0$ is projected from Ω_0 to Ω_i by $\pi(\xi_i \circ X(x, h))$, where $X(x, h) \in \mathbb{R}^3$ is a point in three dimensional space that corresponds to x with depth $h(x)$. In an ideal pin-hole camera model the coordinates of the point $X(x, h)$ are achieved by a multiplication of the homogeneous coordinates of x with $h(x)$. In the following we will use the simplified notation

$$I_i(x, h) = I_i(\pi(\xi_i \circ X(x, h))) \quad (9.2)$$

for this "depth-warped" image.

z-Buffer The sum in (9.1) is taken over all image indices $i \in \mathcal{I}(x)$, for which the projection of $I_i(x, h)$ is visible from the reference frame. The simplest approach is to take only those images for which the projection is inside the reference frame Ω_0 . In our implementation we make use of a z-buffer into which we render the warped image $I_i(x, h)$. This allows to test for occlusions by comparing the depth of $I_i(x, h)$ with the value stored in the z-buffer.

Linearization We linearize $I_i(x, h)$ by using a first order Taylor expansion

$$I_i(x, h) = I_i(x, h_0) + (h - h_0) \left. \frac{d}{dh} I_i(x, h) \right|_{h_0} \quad (9.3)$$

where h_0 is a given depth map and $\frac{d}{dh} I_i(x, h)$ is the directional derivative on the image plane of Ω_0 , that results from a variation of h . This derivative can be expressed as the scalar product of the gradient of $I_i(x, h)$ with the derivative of the projection, that has to be calculated with respect to the chosen camera model. Thus we get

$$\frac{d}{dh} I_i(x, h) = \nabla I_i(x, h) \cdot \frac{d}{dh} \pi(\xi \circ X(x, h)). \quad (9.4)$$

Using this linear approximation for $I_i(x, h)$ we write the functional as

$$E(h) = \lambda \int_{\Omega} \sum_{i \in \mathcal{I}(x)} |\rho_i(x, h)| \, dx + \int_{\Omega} |\nabla h| \, dx \quad (9.5)$$

where $\rho_i(x, h)$ denotes the residual of the linearized data term

$$\rho_i(x, h) = I_i(x, h_0) + (h - h_0) \left. \frac{d}{dh} I_i(x, h) \right|_{h_0} - I_0(x), \quad (9.6)$$

where we omitted the dependency on h_0 . In the following, we present two different strategies to find a minimizer of (9.5).

9.2.1. Half Quadratic Splitting

In [137] we minimized (9.5) by using a quadratic decoupling method proposed in [159], which is also known as half quadratic splitting [51]. The regularizer and data term are decoupled by introducing an auxiliary function $u : \Omega_0 \mapsto \mathbb{R}$. We get the following convex approximation of (9.5):

$$E_{\theta} = \int_{\Omega} \left\{ |\nabla u| + \frac{1}{2\theta} (u - h)^2 + \lambda \sum_{i \in \mathcal{I}(x)} |\rho_i(x, h)| \right\} \, dx, \quad (9.7)$$

where θ is a small constant and $\rho_i(x, h)$ denotes the current residual of the data term i . For $\theta \rightarrow 0$ the minimization of the above functional results in both h and u being a close approximation of each other.

Because the functional is convex both in h and u , it can be minimized by alternating the following steps [137]

1. For h being fixed, solve

$$\min_u \int_{\Omega} \left\{ |\nabla u| + \frac{1}{2\theta} (u - h)^2 \right\} \, dx \quad (9.8)$$

2. For u being fixed, solve

$$\min_h \int_{\Omega} \left\{ \frac{1}{2\theta} (u - h)^2 + \lambda \sum_{i \in \mathcal{I}(x)} |\rho_i(x, h)| \right\} \, dx \quad (9.9)$$

In our earlier work [137] we proposed to minimize the first sub problem (9.8), which is basically the ROF denoising model [121], with the algorithm of Chambolle from 2004 [21]. However, because this problem is strongly convex, it can also be minimized using Algorithm 2 from [24].

The second sub problem can be solved point wise and in [137] we presented a thresholding scheme to find a minimizer of (9.9) in closed form. In [136] we described how to implement this thresholding scheme on the GPU.

9.3. Dualization of the Data Term

Instead of using the half quadratic splitting method discussed above, here we propose to introduce a dual variable for the data term in (9.5). To simplify the notation, we write each summand of the linearized data term as general linear function $\rho_i(x, h) = a_i h - b_i$, with $a_i := I_i^h(x)$ and $b_i := a_i h_0 - I_i(x, h_0) + I_0(x)$. We write (9.5) as

$$E(h) = \lambda \int_{\Omega} \sum_{i \in \mathcal{I}(x)} \{|a_i h - b_i|\} \, dx + \int_{\Omega} |\nabla h| \, dx \quad (9.10)$$

We define the column vector $a := a_1, \dots, a_m$, with $m := |\mathcal{I}(x)|$, and the column vector $b := b_1, \dots, b_m$ and write above energy functional as

$$E(h) = \lambda \int_{\Omega} |a h - b|_1 \, dx + \int_{\Omega} |\nabla h| \, dx, \quad (9.11)$$

with $|\cdot|_1$ we denote the ℓ^1 norm, the sum of the absolute value of each component of a vector.

We introduce a dual variable $p : \Omega \mapsto \mathbb{R}^m$, where m is the number of summands in (9.5), i.e. with one component p_i for each summand of the data term, and $|p_i| \leq 1$, thus $|p|_{\infty} \leq 1$. We also introduce a dual variable $q : \Omega \mapsto \mathbb{R}^2$ for the total variation regularizer.

With these dual variables, we write (9.5) as the saddle point problem

$$\min_{h: \Omega \rightarrow \mathbb{R}_{\geq 0}} \max_{\substack{|p|_{\infty} \leq 1, \\ |q| \leq 1}} \langle p, \lambda a h - \lambda b \rangle + \langle q, \nabla h \rangle, \quad (9.12)$$

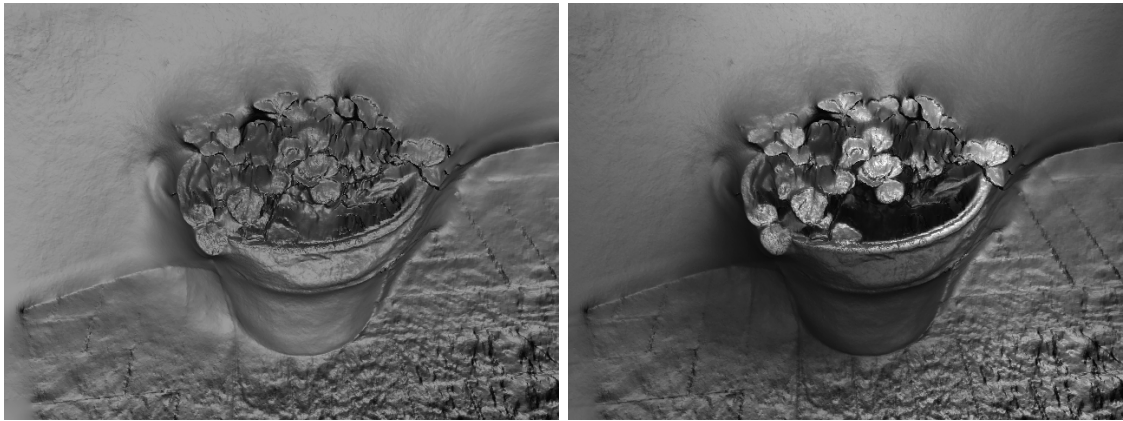
with the ℓ^{∞} norm for the dual variable of the data term and the ℓ^2 norm for the dual variable of the total variation regularizer. With the positivity constraint on h we avoid a mirrored solution that is point symmetric to the focal point.

By rearranging the terms we get

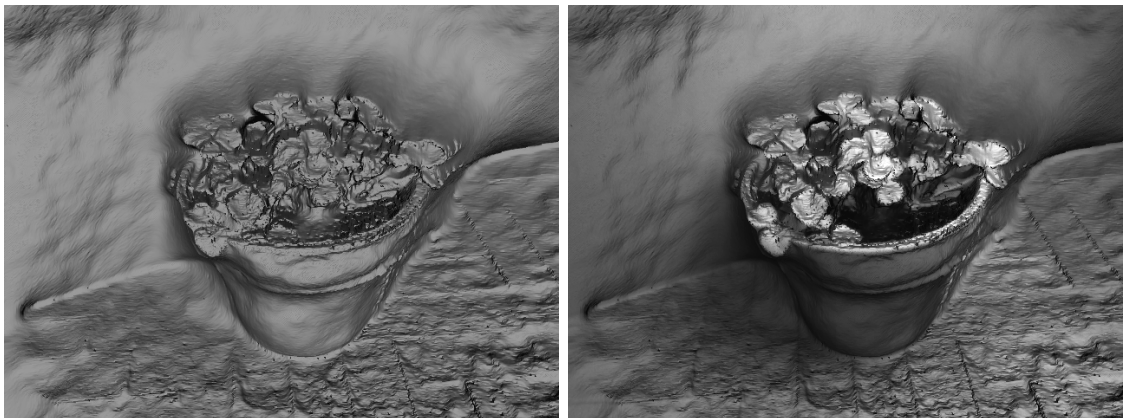
$$\min_{h: \Omega \rightarrow \mathbb{R}_{\geq 0}} \max_{\substack{|p|_{\infty} \leq 1, \\ |q| \leq 1}} \langle p, \lambda a h \rangle + \langle q, \nabla h \rangle - \lambda b p. \quad (9.13)$$

Now we have brought the optimization problem into a standard form that allows to apply Algorithm 1 of [24]. The update equations are defined by the **prox**-operator

$$\begin{aligned} p^{k+1} &= \mathbf{prox}_{\sigma F^*} \left(p^k + \sigma \lambda a \bar{h}^k \right) - \lambda b p \\ q^{k+1} &= \mathbf{prox}_{\nu H^*} \left(q^k + \nu \nabla \bar{h}^k \right) \\ h^{k+1} &= \mathbf{prox}_{\tau G} \left(h^k + \tau \operatorname{div} q^{k+1} - \tau \lambda a^T p^{k+1} \right) \\ \bar{h}^{k+1} &= h^{k+1} + \theta \left(h^{k+1} - h^k \right), \end{aligned} \quad (9.14)$$



(a) Dualized data term



(b) Half quadratic splitting



(c) Reference View (d) Keyframe 1 (e) Keyframe 2 (f) Keyframe 3 (g) Keyframe 4

Figure 9.1.: Comparison of the proposed dualized data term method (a) with the half quadratic splitting method (b). For both methods the weight of the data term is $\lambda = 0.17$, the parameter for the Huber loss for (b) is $\varepsilon = 0.025$. (c-g) The bottom row shows the images used to achieve above reconstructions.

where we choose the step sizes τ , σ , and ν following the diagonal precondition method described in [112].

We evaluate the **prox**-operators with $F^*(p) = \lambda b p$, $H^*(q) = \delta_{|\cdot| \leq 1}$, and $G(h) = \delta_{\geq 0}$ and get as update equations

$$\begin{aligned} p^{k+1} &= p^k + \sigma \lambda \left(a \bar{h}^k - b \right) \\ q^{k+1} &= \pi_{|\cdot| \leq 1} \left(q^k + \nu \nabla \bar{h}^k \right) \\ h^{k+1} &= \pi_{\geq 0} \left(h^k + \tau \operatorname{div} q^{k+1} - \tau \lambda a^T p^{k+1} \right) \\ \bar{h}^{k+1} &= \pi_{\geq 0} \left(h^{k+1} + \theta \left(h^{k+1} - h^k \right) \right). \end{aligned} \tag{9.15}$$

In contrast to the thresholding scheme we described in [136] that requires to sort the critical points, these update equations consist of simple arithmetic expressions and can be efficiently parallelized on the GPU.

9.3.1. Infimal Convolution and the Huber loss

When computing the minimizer of the total variation using the dual variable approach, we discovered stair-casing artifacts in the resulting depth map, a well known effect when minimizing the total variation of a function. In our former approach, where we used the only approximative half quadratic splitting approach, these effects did not appear. A possible explanation is that the half quadratic splitting results in a smoothing of the functional, similar to an infimal convolution with a quadratic function [51].

We provide the definition of the infimal convolution from [110]:

The *infimal convolution* of two closed proper convex functions f and g on \mathbb{R}^n , denoted $f \square g$, is defined as

$$(f \square g)(v) = \inf_x (f(x) + g(v - x)), \tag{9.16}$$

with $\mathbf{dom}(f \square g) = \mathbf{dom} f + \mathbf{dom} g$.

The infimal convolution of a function f with a quadratic function is also known as the *Moreau-Yosida regularization* [97, 158] defined as

$$M_{\lambda f} = \lambda f \square \frac{1}{2} \|\cdot\|_2^2, \tag{9.17}$$

with $\lambda > 0$. With above definition of the infimal convolution we get

$$M_{\lambda f}(v) = \inf_x \left(f(x) + \frac{1}{2\lambda} \|x - v\|_2^2 \right). \tag{9.18}$$

As described in [96, 97, 110], we will now see that the Moreau-Yosida regularization of the absolute value function results in the Huber loss [68].

First we give an intuition for the Moreau-Yosida regularization. Note that the infimal convolution is dual to addition [110, 118]

$$(f \square g)^* = f^* + g^*. \tag{9.19}$$

For $\lambda = 1$, the quadratic term $\frac{1}{2} \|\cdot\|_2^2$ is self-dual and for the bi-conjugate of the infimal convolution it holds that $M_f^{**} = M_f$. It follows that

$$M_f = \left(f^* + \frac{1}{2} \|\cdot\|_2^2 \right)^*, \tag{9.20}$$

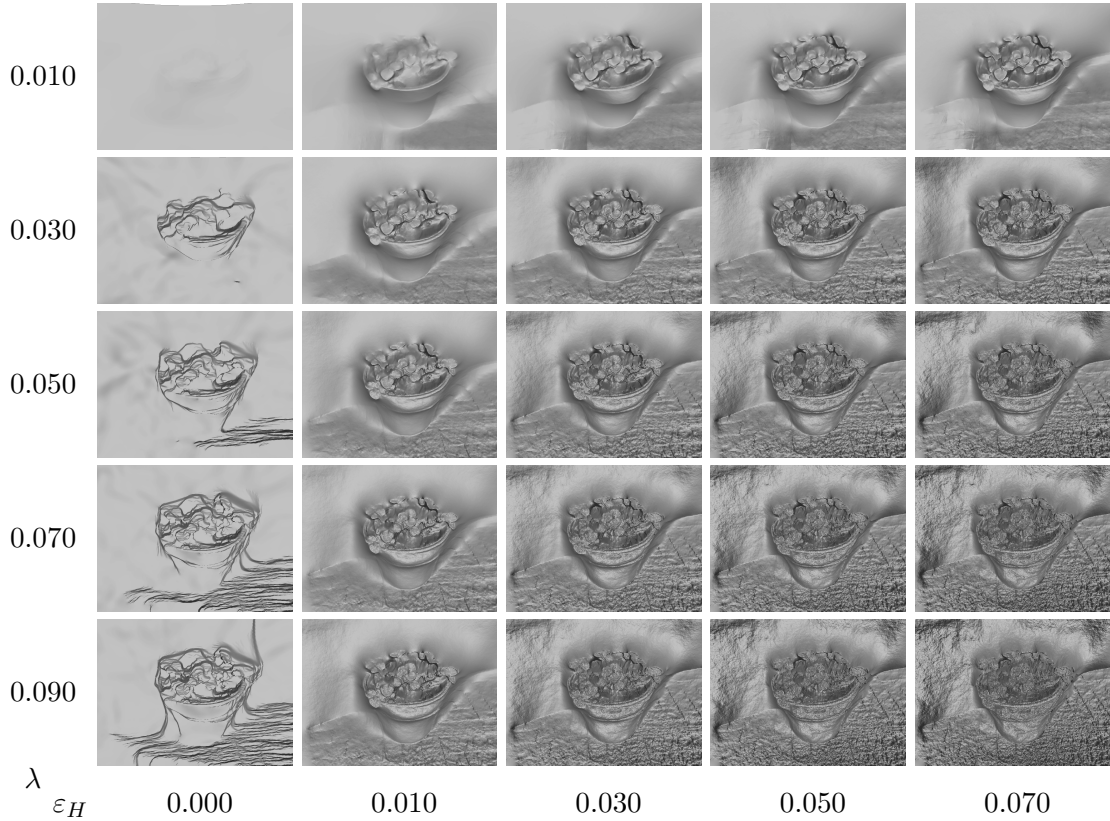


Figure 9.2.: Reconstruction results with Huber loss regularization using the dual variable approach for the data term. Shown are reconstruction results for different parameters for the weight of the data term λ and the Huber loss parameter ε_H .

thus the Moreau-Yosida regularization results is a smooth approximation of a function by quadratic regularization of its conjugate.

When we apply Moreau-Yosida regularization to the absolute value function we get

$$\inf_x \left\{ |x| + \frac{1}{2\varepsilon} \|x\|_2^2 \right\} = \begin{cases} \frac{x^2}{2\varepsilon} & \text{for } |x| \leq \varepsilon \\ |x| - \frac{\varepsilon}{2} & \text{else,} \end{cases} \quad (9.21)$$

which is the *Huber loss* [68], for which we also write $|\cdot|_\varepsilon$ in the following.

9.3.2. Huber-TV for Depth Map Estimation

As we will see in the experiments, using the Huber loss instead of the absolute value function in the regularizer avoids the stair casing artifacts in the depth map. This modified regularizer has already been successfully applied to computer vision tasks such as terrain model generation [146] and optical flow estimation [152]. The functional for depth map estimation from multiple images using the Huber loss function for the regularizer becomes

$$E(h) = \lambda \int_{\Omega} |ah - b|_1 \, dx + \int_{\Omega} |\nabla h|_\varepsilon \, dx, \quad (9.22)$$

with the ℓ^1 norm $|\cdot|_1$ that sums up over the absolute values of the data terms of multiple images and the Huber loss $|\cdot|_\varepsilon$ for the regularizer.

To minimize above functional in the primal dual optimization framework, we need to evaluate the **prox**-operator of the Huber loss. With $H(x) = |x|_\varepsilon$ the conjugate of the Huber loss is

$$H^*(y) = \frac{\varepsilon}{2}|y|^2 + \delta_{|\cdot| \leq 1}(y), \quad (9.23)$$

and the **prox**-operator for the Huber loss becomes

$$\mathbf{prox}_{\nu H^*}(\tilde{y}) = \arg \min_y \frac{1}{2\nu}|y - \tilde{y}|_2^2 + \frac{\varepsilon}{2}|y|_2^2 + \delta_{|\cdot| \leq 1}(y) \quad (9.24)$$

$$= \pi_{|\cdot| \leq 1} \left(\frac{1}{1 + \nu \varepsilon} \tilde{y} \right). \quad (9.25)$$

Thus the update in the dual variable q is given by the projection

$$q^{k+1} = \mathbf{prox}_{\nu H^*} \left(q^k + \nu \nabla \bar{h}^k \right) \quad (9.26)$$

$$= \pi_{|\cdot| \leq 1} \left(\frac{1}{1 + \nu \varepsilon} \left(q^k + \nu \nabla \bar{h}^k \right) \right). \quad (9.27)$$

An experimental comparison of the Huber loss applied to the regularizer with the total variation regularizer is described in the experimental section below.

9.4. Implementation

The linearization of the data term in (9.3) only holds for small variations of h . Inspired by methods that compute the optical flow, we therefore embed the reconstruction method in a multi-resolution framework. Beginning on the coarsest scale a solution for h is computed and propagated to the next higher resolution where it is used as new point h_0 for the Taylor expansion. To initialize the coarsest scale of subsequent frames, we use a transformed and scaled version of the solution for the previous time frame. The first frame is initialized with a constant depth value.

For camera tracking we use the real-time feature based approach of [79], but in principal also other camera tracking methods can be used, *e.g.* the semi-dense tracking approach of [41]. A benefit of both camera tracking methods is, that they are keyframe based: the camera pose for a subset of keyframes is iteratively improved. While the pose for the current camera image needs to be estimated very quickly, and thus is expected to be not very accurate, the keyframe poses are iteratively improved and thus are much more stable.

We utilize the higher accuracy of the camera poses of the keyframes, and choose the images from such keyframes as additional views I_1, \dots, I_m . The depth map is computed for the current camera frame with respect to the closest keyframes which have a sufficient baseline. This approach yields dense reconstructions for the current view of the camera in real-time.

9.5. Experimental Results

We compare the proposed dual variable approach with the previous approach that used half quadratic splitting. Fig. 9.1 depicts reconstruction results of both methods to allow a direct comparison. We use the highest quality parameter in Table 9.1, with a multi-resolution pyramid of 24 levels. As depicted in the figure, the reconstruction results are

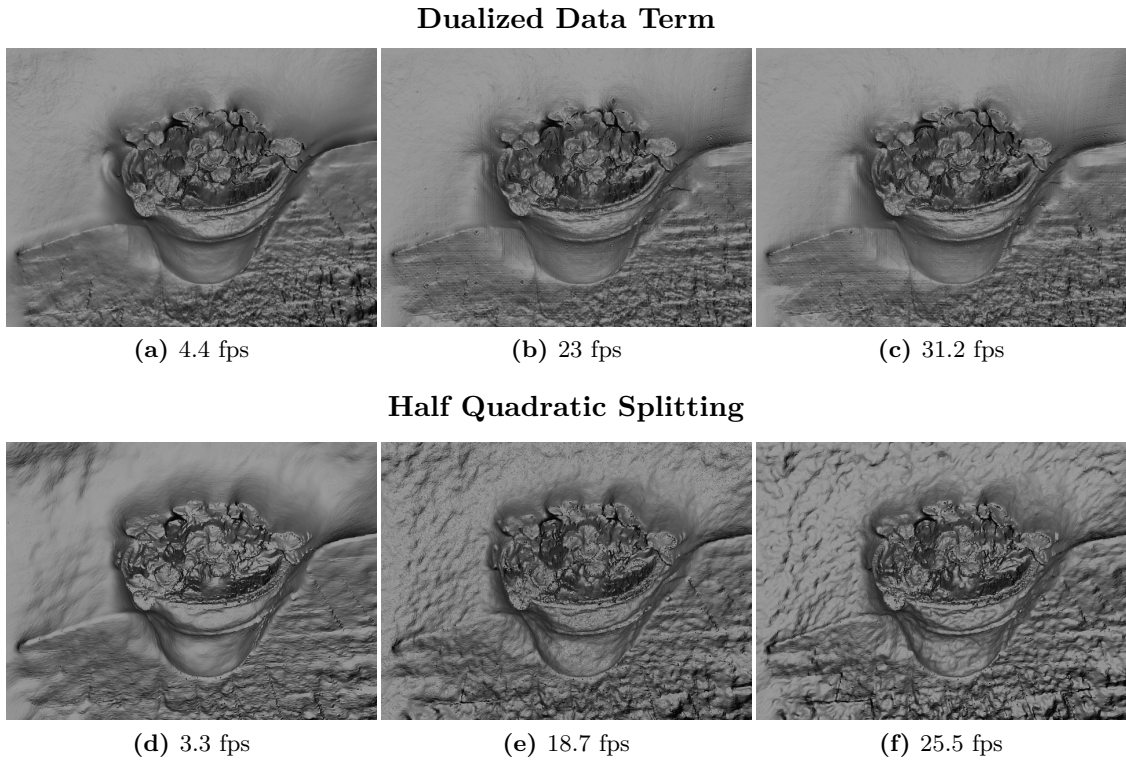


Figure 9.3.: Runtime comparison between both approaches. For comparison we use the same parameters as in [137].

Table 9.1.: Runtime comparison between both approaches. Parameter settings of the experiments depicted in Fig. 9.3. The first two parameters describe the multi-resolution pyramid. The next parameter is the number of iterations per scale level. Inner iterations refer to the number of iterations performed on a block before the values on the boundary of the block are synchronized. The speedup factors are in comparison the values reported in [137]

Parameter Setting	(a)+(d)	(b)+(e)	(c)+(f)
Multi-Scale Levels	24	10	7
Scale Factor	0.94	0.8	0.7
Iterations per Level	120	70	70
Inner Iterations	1	4	4
Frames per Second			
Values reported in [137]	1.8	11.3	24
Half Quadratic Splitting	3.3 (1.8×)	18.7 (1.7×)	25.5 (1.1×)
Dualized Data Term	4.4 (2.4×)	23.0 (2.0×)	31.2 (1.3×)

Table 9.2.: Detailed Dense Reconstructions in Real-Time. Parameter settings of the experiments depicted in Fig. 9.4. The proposed dual variable approach allows to solve each linearized sub-problem with higher precision while the half-quadratic splitting method only allows to compute an approximative solution. As a result, only very few scale levels are needed for the dual variable approach. This allows to reach real-time performance without the need of additional speedup by inner iterations.

Parameter Setting	(a)+(b)	(c)+(d)	(e)+(f)
Multi-Scale Levels	10	7	4
Scale Factor	0.8	0.7	0.5
Iterations per Level	70	70	70
Inner Iterations	1	1	1
Frames per Second			
Half Quadratic Splitting	12.9	17.9	34.5
Dualized Data Term	16.0 (1.24 \times)	22.0 (1.23 \times)	41.1 (1.19 \times)

almost the same, clearly the dual variable approach allows reconstructions which are en-par with the quadratic splitting approach. In some areas the dual variable approach even allows more detailed reconstructions, as visible for example at the leaves of the plant.

Huber loss Fig. 9.2 depicts the parameter space of the Huber loss regularized approach for different values of the weight of the data term λ and the Huber loss parameter ε . Both parameters influence the detail and noise level of the reconstruction, but once a parameter setting has been selected, the reconstruction result is very stable over different time frames and also for different parameters, *e.g.* iteration number or different multi-resolution settings. In the quadratic splitting approach, the weight θ of the quadratic penalty had to be tuned to allow a stable reconstruction. Furthermore a common approach is to reduce the weight θ exponentially during the optimization. This scheme however needs to be carefully adjusted and depends on the number of iterations.

Runtime Comparison Both methods are implemented for the GPU using the CUDA programming framework and we report runtime results on an *nVidia GeForce GTX Titan X* GPU. First, we perform an experiment with the same parameters as in [137]. Due to the modern hardware, a speedup between 1.1 \times and 1.8 \times is achieved for the half quadratic splitting approach in comparison to the runtime results reported in [137]. The dual variable approach however allows an even larger speedup of 1.3 \times to 2.4 \times compared to [137], which corresponds to a relative speedup of 1.2 \times to 1.3 \times in comparison to the half quadratic splitting approach.

Detailed Dense Reconstructions in Real-Time The proposed dual variable approach has a huge benefit over the half quadratic splitting method. On each scale level of the multi-resolution pyramid, the linearized problem can be solved with higher precision while the half-quadratic splitting method only allows to compute an approximative solution. As a result, only very few scale levels are needed. As depicted in Fig. 9.4 this allows to compute detailed dense reconstructions at 41.1 frames per second with only

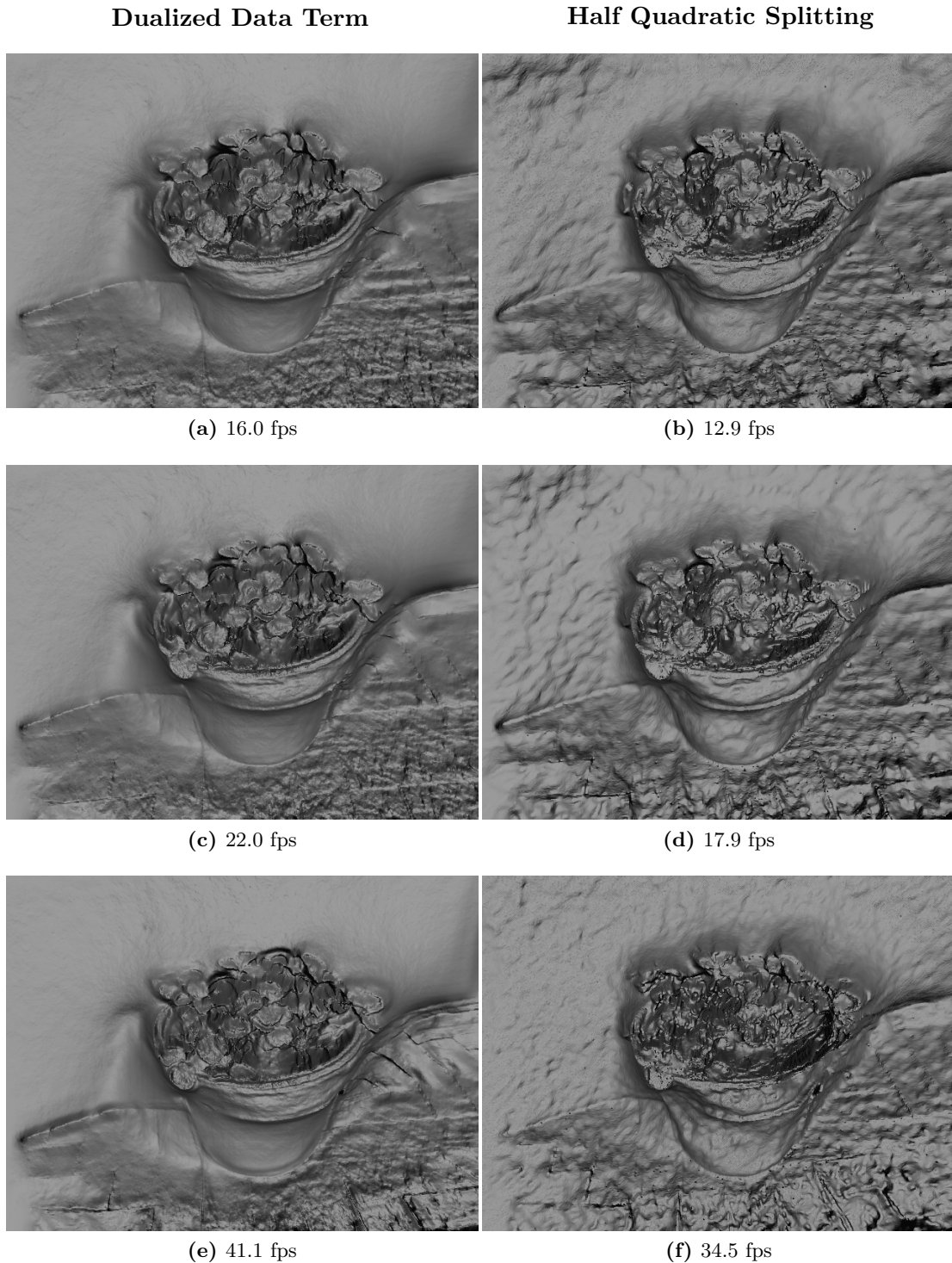


Figure 9.4.: Detailed Dense Reconstructions in Real-Time. The proposed method with dual variables in the data term allows very detailed reconstructions in real-time. In comparison to the half quadratic splitting approach the proposed method is much more stable which allows to use a coarser multi-resolution pyramid. Real-time performance is reached without the need for approximative accelerations by performing several iterations before the values on the boundary of each block, that is processed in parallel, are synchronized. This value is called *inner iterations* in Table 9.1. Results that were acquired using this acceleration are depicted in Fig. 9.3. There is only a very small trade-off between accuracy and speed and in comparison to the half quadratic splitting method, the quality does not degrade as quickly (also compare to Fig. 9.3 d-f). Depicted are renderings of reconstructions and their respective runtime performance in frames per second (fps) using the parameters shown in Table 9.2.

4 levels of the multi-resolution pyramid and a scale factor of 0.5. In contrast to our previous approach in [137] no additional approximative techniques such as inner iterations on every block are needed to achieve (more than) real-time performance. The parameter settings used for the reconstructions depicted in Fig. 9.4 are shown in Table 9.2.

9.6. Conclusion

We described a primal-dual optimization method for real-time dense geometry reconstruction with a single camera, which extends our earlier work [137] by using dual variables in the data term. Furthermore, we derived the Huber loss in the total variation regularizer by interpreting the half quadratic splitting method as infimal convolution of the absolute value function with a quadratic term. We observed that the Huber loss in the regularizer prevents the staircasing artifacts of the total variation and thus greatly improves the segmentation results, leading to reconstructions which are qualitatively comparable to those achieved with half quadratic splitting. However, the dual variable approach for the data term leads to a large benefit: in contrast to the only approximative half-quadratic splitting, the dual variable approach allows to minimize each linearized subproblem with higher precision. This allows to use much fewer levels of the multi-resolution pyramid and leads to reconstructions of much higher quality at high frame rates.

10. 3D Tracking from Raw ToF data

The 3D reconstruction methods described so far are *image based* reconstruction methods, which reconstruct the geometry from images of traditional video and photo cameras. Because digital color images are encoded using a red, green and blue color channel, these image modalities are also referred to as *RGB* data. In this chapter, we will present a novel approach for object tracking for a special type of sensor, that in addition to the red, green, and blue color channel also measures the depth of the scene for every pixel. These sensors are commonly referred to as depth cameras or *RGBD* cameras, to emphasize that in addition to a red, green and blue channel these sensors also measure the depth of the scene for every pixel. This additional information greatly improves segmentation and tracking of rigid, articulated, and even deformable 3D objects in real-time. However, these depth cameras typically have a limited temporal resolution (frame-rate) that restricts the accuracy and robustness of tracking, especially for fast or unpredictable motion. In the following, we show how to perform model-based object tracking at an order of magnitude higher frame-rate. This is achieved through simple modifications to an off-the-shelf depth camera. We focus on phase-based time-of-flight (ToF) sensing, which reconstructs each low frame-rate depth image from a set of short exposure ‘raw’ infrared captures. These raw captures are taken in quick succession near the beginning of each depth frame, and differ in the modulation of their active illumination. Instead of computing a depth frame for this set of raw captures, we propose a model-based tracking approach that allows to infer the depth of the object for each individual measurement. We make two main contributions. First, we detail how to perform model-based tracking against these raw captures. Second, we show that by reprogramming the camera to space the raw captures uniformly in time, we obtain a 10× higher frame-rate, and thereby improve the ability to track fast-moving objects. The proposed approach has the side-benefit of avoiding the depth reconstruction step that may be costly for mobile applications.

The results presented in this chapter are joint work with Sebastian Nowozin and Jamie Shotton and have been previously published in [138]. The research was conducted in cooperation with Microsoft Research Cambridge and partly funded by the Microsoft Research internship program.

10.1. Introduction

Tracking objects that move is one of the fundamental research topics in computer vision, that enables higher-level reasoning about the world and allows to build systems that interact with the environment. Real-time tracking and especially tracking of the articulated human body enable applications in human computer interaction which allow a very intuitive user interface. One way to enable interaction is by tracking the full body pose [130], more recent approaches allow real-time tracking of the articulated hand [129]. These methods allow the user to interact with the computer in an intuitive way without the need of an additional input device, e.g. by pointing with the finger at objects on a screen or even in the scene itself [148].

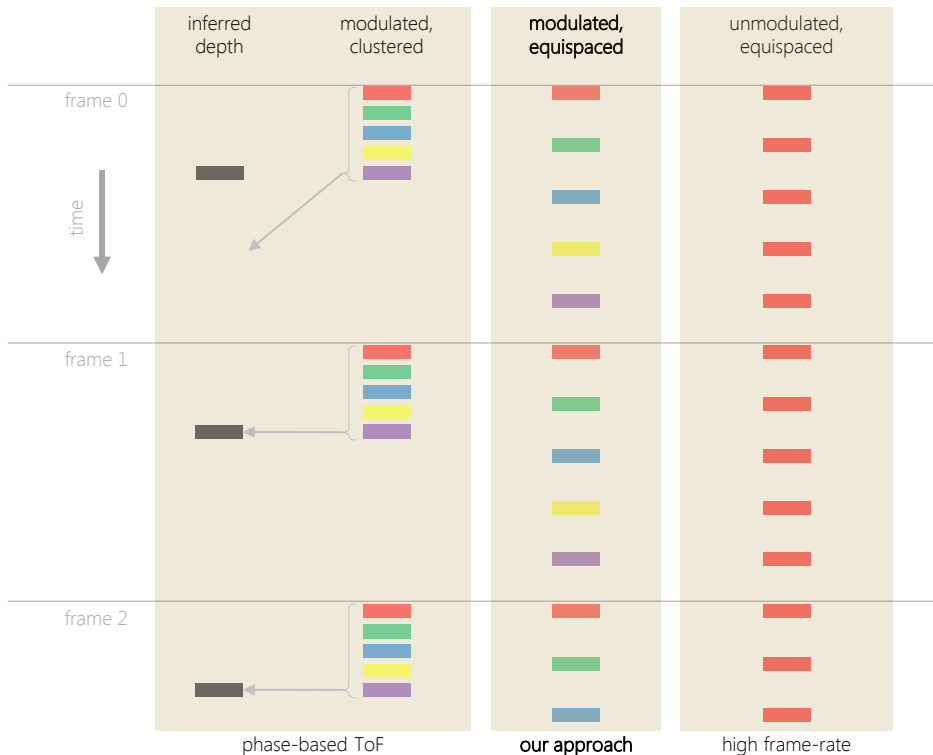


Figure 10.1.: Overview. Phase-based time-of-flight (ToF) sensors infer a low frame-rate stream of depth images from a set of short-exposure ‘raw’ captures that are clustered closely in time to reduce motion artifacts. For illustration purposes, we use five colors here to indicate different frequencies and phase modulations of the illuminant and sensor; see text. For the application of model-based tracking, we propose to forego the depth reconstruction step, and instead track directly from *equispaced* raw captures, resulting in a signal at much higher frame-rate.

However, the visual object tracking problem itself bears several key challenges that limit the accuracy of current systems. One of the main difficulties in tracking is the change of the object’s appearance due to object translation, rotation, deformation, and lighting variation. Further difficulty stems from object occlusion, and objects leaving the viewing volume. Another key challenge is the simultaneous tracking of multiple objects whose number may vary over time, and tracking fast moving objects. These challenges make it hard to build robust tracking algorithms that can achieve human level accuracy and robustness.

Modeling these effects is very challenging, thus general purpose tracking approaches employ non-parametric models, *e.g.* in mean-shift tracking [28], or estimate the object representation during tracking by using online learning [119]. Tracking of multiple objects with similar appearance usually requires to integrate observations over a longer period of time [4, 105]. After all, general purpose tracking remains a challenging problem, as demonstrated in the recent VOT 2014 tracking challenge [85]. For a review on object tracking approaches, see [156, 157].

Here, we want to focus on tracking *fast-moving* rigid objects, and in particular on tracking the object in three dimensional space from a single viewpoint. An established approach to address this problem is to use high speed sensors from multiple viewpoints [86, 98], however this approach usually requires custom hardware. Instead of increasing the time resolution, an alternative is to increase the resolution of the sensor to allow for an improved angular resolution, as described in an extensive synthetic SLAM study [64]

However, using multiple sensors and increasing the frame rate by using a high speed camera or even custom built hardware is expensive. Also multiple camera systems usually require a tedious and time consuming calibration step before they can be used for tracking. Therefore, we instead propose to use a single time-of-flight (ToF) sensor, the Kinect V2 [6], for high speed object tracking. In the following we will show how the sensor can be re-purposed for this application. Furthermore, we validate in experiments that the proposed approach allows to accurately infer the depth of the object from observations from a single viewpoint. The method is very general and should easily extend to other commercially available ToF sensors.

The proposed method is based on the working principles of phase-based ToF sensors, which is illustrated in Fig. 10.1. To infer a single depth image (each gray bar on the left), the sensor captures a set of actively illuminated infrared frames (the colored bars in the left column). A frame rate of 30Hz for the depth images is achieved by capturing the infrared frames at an average frequency of 300Hz. To minimize movement of the object during the capture period, which is required for a consistent depth reconstruction of the scene, the infrared frames are captured in a short burst at the beginning of each 30Hz cycle. The active illumination of the infrared frames is modulated with one of three different frequencies and one of three different phases. Each infrared frame is recorded with a particular combination of frequency and phase shift, resulting in nine differently illuminated infrared frames per depth frame. The camera also captures an additional tenth frame without active illumination, to allow to correct for ambient brightness in the infrared frames.

In the following, we will show how this phase-based ToF sensor can be re-purposed for fast object tracking. Our method consists of two contributions: First, we describe an observation model that allows to perform model-based object tracking directly in the raw infrared ToF captures. The main advantage of this approach is, that it does not require a reconstruction of a depth frame prior to tracking. As we will show in the following, this allows to track objects with much faster motion, for which the usual depth reconstruction would fail. Second, we propose an exposure timing better suited for tracking, that is different to the burst mode used for depth reconstruction. We show that when equally spacing the frames out in a 30Hz interval, we achieve a more stable tracking output and are able to track much faster moving objects at approximately 300Hz (see Fig. 10.2).

We implement the above ideas in a model-based tracking framework, that consists of a probabilistic state space model and a temporal prior. While this probabilistic tracking approach is a standard approach for object tracking, our contribution is a generative model of the observation likelihood, that allows to compare the raw infrared captures to a rendered simulation of an object with known shape and albedo. We validate in experiments that we can accurately track a fast moving rigid object in three dimensions, even for object speeds for which the depth reconstruction fails.

In contrast to a depth-based tracking method, that would fail completely in case of fast motions, we do not need to first infer a depth image but instead directly track the object in the raw ToF frames. Compared to constant illumination high frame-rate tracking, the benefit of the proposed method is that we not only achieve a high frame rate but that each frame contains a distinctive active illumination response that contains additional depth information.

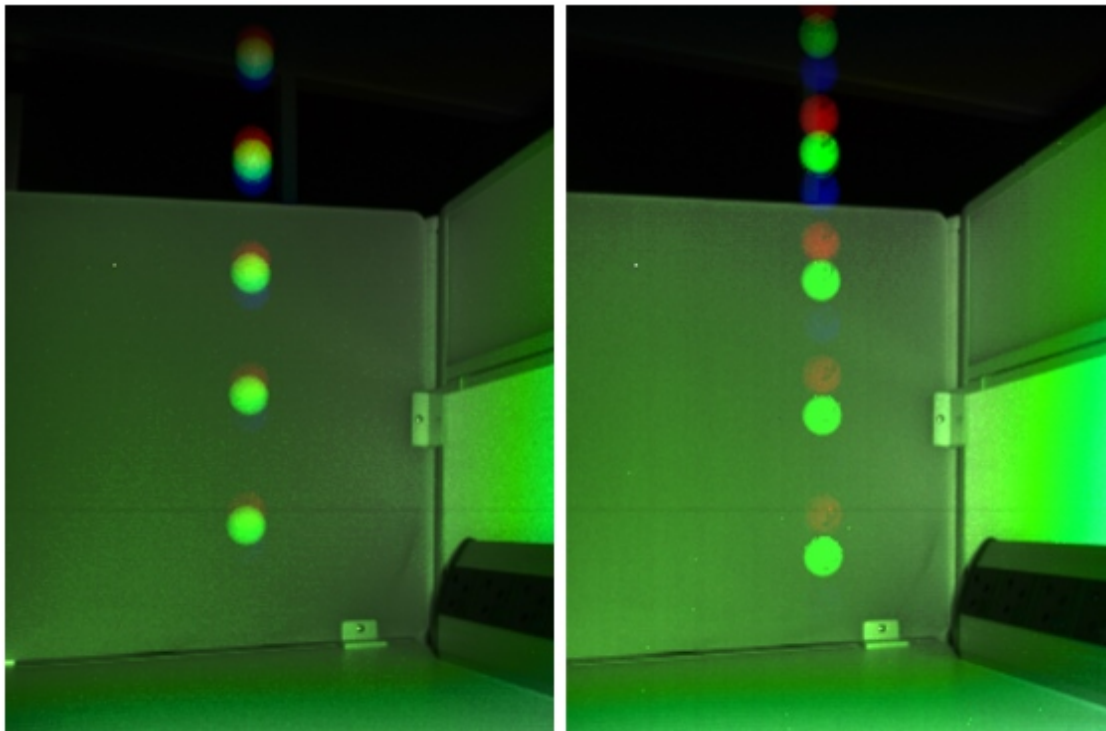


Figure 10.2.: Time-of-flight captures and fast motion. A table tennis ball is dropped, and three raw captures are superimposed for visualization using the red, green, and blue color channels. **Left:** The standard timing used for phase-based ToF clusters the captures temporally to minimize motion artifacts in the depth reconstruction. **Right:** We propose to evenly space out the ToF captures in time. We demonstrate that this allows for more stable tracking of fast moving objects without previous reconstruction of a depth image.

10.2. Background

Before we describe our main contributions, we provide some background material on phase-based time-of-flight sensors and model-based tracking.

10.2.1. Phase-Modulation Time-of-Flight

State-of-the art ToF cameras perform depth measurements by phase modulated active illumination: The camera contains an active light source, that is amplitude modulated with a specific frequency. The scene is recorded by the sensor, which is gain-modulated with the same frequency [87, 127]. During the frame exposure, the sensor integrates over a large number of oscillation periods and the recorded image intensities contain information about the phase shift between emitted light and incoming light. This phase shift depends linearly on the time it took for the emitted light to travel from the light source to the object, where it is reflected back to the sensor. Usually, the phase shift wraps around several times for depth ranges in typical scenes. To disambiguate between multiple possible depth values that correspond to the same phase shift, a set of frames with different modulation frequencies and phase delays is recorded. The information that is contained in the set of recorded frames then allows a unique disambiguation of the distance via phase unwrapping algorithms [62, 65, 91]. To allow for a stable phase unwrapping, it is important that the depth of the object does not change between the independent measurements of a set of frames. Thus the frames are recorded in a short

time span at the beginning of each depth reconstruction cycle, to reduce the motion of the object between the different captures. This standard operation mode is illustrated in the leftmost column in Fig. 10.1.

Formally, we obtain a sequence of nine measurements R_1, \dots, R_9 (3 frequencies \times 3 phases) for each pixel with

$$R_i = \frac{\rho}{d^2} S_i(d) + \epsilon_i, \quad (10.1)$$

where $d > 0$ is the depth of the imaged surface at that pixel and $\rho > 0$ is the surface *albedo*. The responses S_i depend on the specific modulation frequency and phase delay and are given by an idealized calibrated response curve [6],

$$S_i : [d_{\min}, d_{\max}] \rightarrow \{-I_{\max}, \dots, -1, 0, 1, \dots, I_{\max}\},$$

where d_{\min} and d_{\max} denote the range of valid depths that are mapped to signed image intensities between $-I_{\max}$ and I_{\max} . We simply assume zero mean Gaussian noise as noise model ϵ_i with a fixed standard deviation.¹

The standard approach to reconstruct a depth frame is to use a phase-unwrapping method which infers the depth from the nine measurements as

$$\hat{d} = f(R_1, \dots, R_9). \quad (10.2)$$

The proposed approach instead directly performs tracking in the raw measurements, without the need to first infer a depth frame.

10.2.2. Model-Based Tracking

We use model-based object tracking [83, 155], with a generative observation model to relate the estimated position to the observations. To allow for stable tracking we use a temporal model that relates measurements over time and follow the work by Isard and Blake [70] by performing *particle filtering* [58] in a state space model. For a state space model we first need to specify a state space and additionally both a probabilistic transition model and a probabilistic observation model [37].

As state vector we use

$$X_t = (x_t, v_t), \quad (10.3)$$

which encodes a 3D location $x_t \in \mathbb{R}^3$ in some reference frame (also called world coordinate) and a 3D velocity vector $v_t \in \mathbb{R}^3$. To track general rigid objects we could include rotation parameters, i.e. by extending the state space to $X_t = (x_t, r_t, v_t)$. To demonstrate our key contribution, how to perform object tracking in the phase encoded infrared frame, here we instead use a setup as simple as possible and use a rotationally invariant object (a table tennis ball) in the experiments and thus do not need to include rotational parameters in the state space.

Temporal coherence is achieved with a stochastic transition model which is specified via a distribution $P(X_{t+1}|X_t)$ that encodes the assumed laws of motion (see below for further details). For the observation model we implement an analysis-by-synthesis approach: an observation Y_t corresponds to an entire raw ToF frame. We assume that we are given a 3D model of the object together with a model for the object's reflectivity. This allows to synthesize a rendering of the object as it would appear in the phase-encoded raw

¹Because the phase shift is measured in the Kinect sensor by computing the difference of two accumulation buffers [6], a more accurate noise model would be an intensity-dependent Skellam noise. Here we choose the Gaussian approach for simplicity.

ToF frame. Then the observation likelihood is computed by comparing this synthesized rendering with the observed raw ToF frame (further details are given below).

Combining the transition and observation model yields a joint distribution over the entire sequence of states $X_{1:T}$ and observations $Y_{1:T}$ as

$$P(X_{1:T}, Y_{1:T}) = \prod_{t=1}^T P(X_t|X_{t-1}) P(Y_t|X_t), \quad (10.4)$$

where $P(X_1|X_0) = P(X_1)$ is the initial distribution over the state space of the first frame that is assumed to be given.

When the transition model and the observation model are defined, inference about the object's state for given observations can be done either by *filtering* or by *smoothing* [37]. In *filtering* the distribution over the current position and velocity is estimated depending on all past observations. Because filtering allows to infer a distribution about the current object state it is suitable for an interactive setup. At each time step t , filtering provides the marginal distribution $P(X_t|Y_{1:t})$ over the current state X_t . In *smoothing*, observations both from the past and the future are used, thus inference is performed offline after the entire sequence $Y_{1:T}$ of T frames has been observed. This approach significantly improves tracking accuracy [71] as the inference result $P(X_{1:T}|Y_{1:T})$ integrates over all observations. However, the approach only allows for offline tracking and thus is not suitable for interactive tracking. A suitable intermediate strategy for online tracking is *fixed-lag smoothing* [35]: inference is delayed by a small number of K frames and inference is performed by smoothing over a truncated sequence, i.e. only the distribution over a partial sequence $P(X_{(t-K+1):t}|Y_{1:t})$ is inferred. Fixed-lag smoothing allows a trade-off between the low latency of filtering and the high accuracy of smoothing: for $K = 1$ the approach results in filtering, and for $K = T$ it results in smoothing. This allows for improved accuracy for interactive tracking at the expense of a fixed latency.

For the results reported in this work we found that filtering, implemented using the bootstrap particle filter [58], offered sufficient accuracy and stability.

10.3. Method

In this section we describe the model for tracking a fast moving object directly in the phase encoded raw ToF captures. While we use a standard motion model, the observation model for raw ToF captures is a novel contribution.

10.3.1. Motion model $P(X_{t+1}|X_t)$

We use the state representation (10.3) and define a linear motion model as a multivariate Gaussian distribution

$$P(X_{t+1}|X_t) \sim \mathcal{N} \left(\begin{bmatrix} x_t + \Delta v_t \\ v_t \end{bmatrix}, \begin{bmatrix} \sigma_x^2 I_3 & 0 \\ 0 & \sigma_v^2 I_3 \end{bmatrix} \right), \quad (10.5)$$

where Δ is the time difference between the frames captured at step t and $t + 1$, and $\sigma_x > 0$ and $\sigma_v > 0$ are the noise parameters for the position and velocity vectors respectively. Above model (10.5) predicts the position x_{t+1} by linear extrapolation in time of the currently estimated position x_t with the current estimate of the velocity vector v_t . Any change to the velocity is modeled with the noise term σ_v , but more complicated

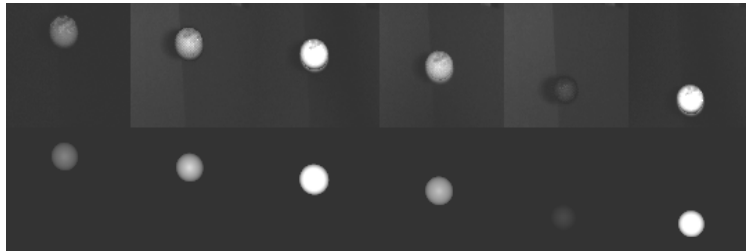


Figure 10.3.: Model Based Tracking. Depending on the frequency and phase configuration of the individual exposures, the object appears with different illuminations in the raw ToF captures. The generative forward model allows to synthesize the appearance of the object for these different illuminations. First row: Observed raw ToF image. Second row: Rendered image of the best hypothesis. Columns correspond to individual exposures.

motion models are possible, for example by including gravity or modeling changes of the movement direction, *e.g.* by explicitly modeling deflection off the ground. Here we chose (10.5) as probably the simplest possible motion model to demonstrate our main contribution: an observation model that allows for raw ToF-based tracking.

10.3.2. Observation model $P(Y_t|X_t)$ for raw ToF

Now we describe our main contribution: the observation model that allows to compute observation likelihoods directly against the raw ToF captures without the need to first compute a depth map.

The observation model describes the conditional distribution $P(Y_t|X_t)$, where Y_t is an observed raw ToF frame of size 512×424 together with its timestamp, and X_t is the hypothesis about the current state of the object. The raw ToF frame consists of phase-encoded responses (10.1) for each sensor element (sensel). With $\bar{R}_i(r)$ we denote the observed response at sensel location r and shutter type i , a specific configuration of frequency and phase shift of the active illumination of this frame. An observation is then encoded as $Y_t = (i, \bar{\mathbf{R}}_i)$, where i is the shutter type, and $\bar{\mathbf{R}}_i$ is the vector of all responses at all sensel locations. When recording a sequence of images, the shutter type i changes in a predefined cyclic order, and thus does not need to be modeled probabilistically. Therefore, we only have to specify a probabilistic model for the observed frame $\bar{\mathbf{R}}_i$.

The probabilistic model for the raw ToF observation $\bar{\mathbf{R}}_i$ is based on an analysis-by-synthesis approach: given the hypothesis for the current state X_t we first render a distance map $d(r)$ and reflectivity $\rho(r)$ of the object for every sensel r . The reflectivity of the object is modeled by a Blinn-Phong model [14], whose parameters are fitted empirically to the object appearance in a calibration step prior to tracking. We use the ideal response curve from equation (10.1) with the rendered distance $d(r)$, the reflectivity $\rho(r)$, and the known shutter type i and compute the expected response $R_i^{\text{obj}}(r)$ for each location r . Fig. 10.3 shows pairs of observed and rendered responses side by side. The whole pipeline of rendering the depth and reflectivity of the object and finally computing the ideal response is implemented efficiently on the GPU using the HLSL shader language.

To compute the likelihood of the current hypothesis X_T , the synthesized response $R_i(r)$ is compared to the observed response $\bar{R}_i(r)$. Here, a difficulty arises: so far the rendering model only provided a synthesized response for the object, and does not contain an explicit model for the background. A possible strategy is to compare only sensels that belong to the object for an assumed location X_t . However, this does not provide a valid distribution $P(Y_t|X_t)$ for the entire observed frame and is biased by the amount of sensels in the frame that are covered by the object.

To solve for this bias, we explicitly model the background. A common approach for RGB images is to model the background via mixture models, *e.g.* in the seminal publications [48, 133, 161]. For simplicity, we assume a static camera and a static background, and use a simpler Gaussian model as described below. Prior to tracking, we record a few seconds of static background video. Then, for every shutter type i and every location r , we compute the empirical mean $\hat{\mu}_i(r)$ of the observed responses $\bar{R}_i(r)$. In case the video contains moving objects, those can be removed by computing the more robust median of a sufficiently long sequence instead of taking the mean. We assume the background to be distributed by a Gaussian distribution

$$R_i^{\text{bg}}(r) \sim \mathcal{N}(\hat{\mu}_i(r), \sigma_{\text{bg}}^2), \quad (10.6)$$

where σ_{bg} is the standard deviation of the background noise in raw ToF units, typically in the range of a few hundred units.

We get the full model $P(Y_t|X_t)$ by a composition of the object responses R_i^{obj} for sensel locations which are occupied by the rendered object hypothesis X_t , and the background responses R_i^{bg} for the remaining part of the frame. To compute this composition, the renderer computes a mask of occupied sensel locations during rendering. Let us denote the mask by $M(r) \in \{0, 1\}$ where $M(r) = 1$ denotes a location inside the object. The full model then is obtained as

$$R_i(r) \sim \begin{cases} \mathcal{N}(R_i^{\text{obj}}(r), \sigma_{\text{obj}}^2), & \text{if } M(r) = 1, \\ \mathcal{N}(\hat{\mu}_i(r), \sigma_{\text{bg}}^2), & \text{otherwise.} \end{cases} \quad (10.7)$$

Here σ_{obj} is a parameter that specifies the assumed noise in the object responses. We assume the noise to be independently distributed among the sensel locations, thus the joint model for the full raw ToF frame is modeled by a product of Gaussian distributions (10.7) and itself is a multivariate Gaussian. We compute the log-likelihood function as

$$\begin{aligned} \log P(Y_t|X_t) = & - \sum_{r:M(r)=1} \left[\frac{(\bar{R}_i(r) - R_{\text{obj}}(r))^2}{2\sigma_{\text{obj}}^2} + \log \sigma_{\text{obj}} \right] \\ & - \sum_{r:M(r)=0} \left[\frac{(\bar{R}_i(r) - \hat{\mu}_i(r))^2}{2\sigma_{\text{bg}}^2} + \log \sigma_{\text{bg}} \right] + C, \end{aligned} \quad (10.8)$$

where $C = -\frac{n}{2} \log(2\pi)$ is a constant independent of the observation (with $n = 512 \cdot 424$ the number of sensels per frame) that can be omitted.

Above observation model is evaluated for several thousand object hypotheses against the same observation. Therefore it would be very expensive to evaluate above equation for every sensel location of the frame. Instead we use simple arithmetic to achieve a significant speedup. We use the following identity:

$$\begin{aligned} \log P(Y_t|X_t) = & - \sum_{r:M(r)=1} \left[\frac{(\bar{R}_i(r) - R_{\text{obj}}(r))^2}{2\sigma_{\text{obj}}^2} + \log \sigma_{\text{obj}} \right. \\ & \left. - \frac{(\bar{R}_i(r) - \hat{\mu}_i(r))^2}{2\sigma_{\text{bg}}^2} - \log \sigma_{\text{bg}} \right] \\ & - \sum_r \left[\frac{(\bar{R}_i(r) - \hat{\mu}_i(r))^2}{2\sigma_{\text{bg}}^2} + \log \sigma_{\text{bg}} \right] + C, \end{aligned} \quad (10.9)$$

where the last sum of the log-likelihood of the background model is taken over the whole frame. It is independent of the hypothesis and thus needs to be computed only once for

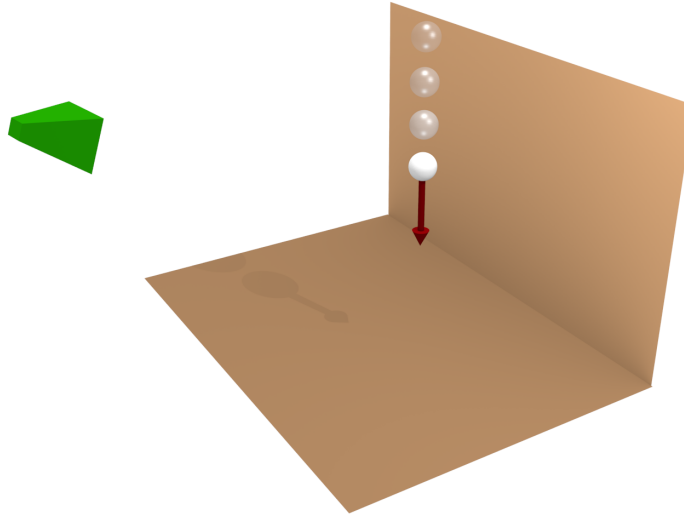


Figure 10.4.: Experimental setup A. A table tennis ball is released from a stationary position and accelerates towards the ground. The camera observes this fall at a slightly downwards angle which results in motion both along the vertical axis and the depth axis.

a given observation. Only the first term depends on the object hypothesis and has to be evaluated only for those sensel locations occupied by the object.

10.4. Implementation and Validation

Implementation details We implement the equidistant exposure timing of the Kinect sensor [6] in a custom firmware. However, in principle this modification can also be applied to other phase modulation based ToF cameras, *e.g.* to sensors from PMD, Intel, or Mesa Imaging. The tracking algorithm is implemented in C++ on the CPU and the rendering and likelihood computation pipeline is performed entirely on the GPU, implemented in the HLSL shading language. A tiled layout for the rendering pipeline enables to evaluate over 8000 particles in parallel and allows real time tracking at 300 Hz using 4096 particles on modern GPU hardware.

Experimental setup A. We use two different setups for the experiments, depicted in Fig. 10.4 and Fig. 10.5. In the first setup, the scene is observed by a static camera mounted on a tripod and a table tennis ball is released from a fixed position in front of the camera. It is released with no inertia and thus falls downwards accelerated purely by gravity. Because the camera is tilted slightly downwards, the downward motion of the falling ball results in both a motion along the vertical axis and the depth axis of the camera coordinate frame. This allows to evaluate the quality of the depth estimate achieved with the model based tracking approach.

The ball quickly reaches a velocity that prevents a reliable depth reconstruction using phase unwrapping because of insufficient overlap in the individual raw ToF frames (see Fig. 10.7). Thus there is no ground truth available for the whole sequence. To nevertheless evaluate the tracking performance quantitatively we use the following procedure: Accelerated purely by gravity, the trajectory of the table tennis ball lies on a line in

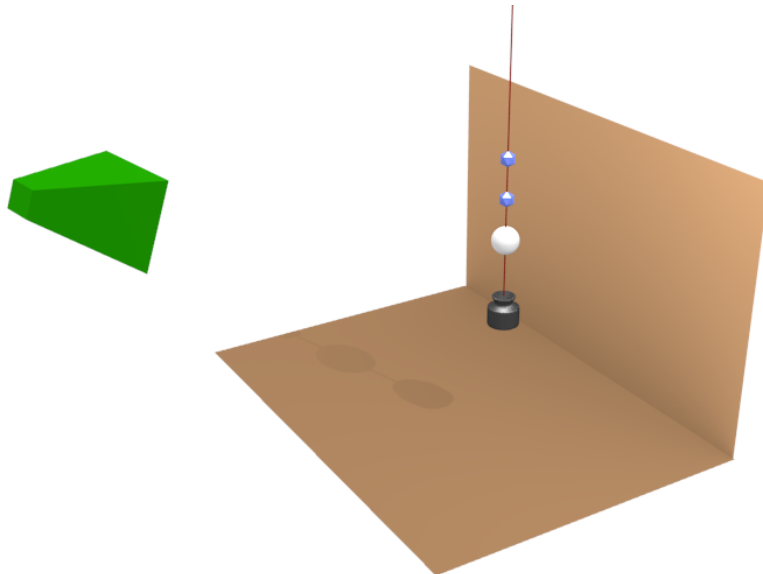


Figure 10.5.: Experimental setup B. A table tennis ball attached to a rope is obtaining a pendulum movement. Attached to the rope are two reflective markers used for motion capture. The rope is ensured to be a straight line by an attached weight. The scene is captured by the Kinect camera and by a commercial Motion Capture system consisting of 11 cameras (not shown).

3D space. The tracking algorithm estimates object coordinates at each observation as the weighted average of the particle positions. We fit a line through these estimated 3D coordinates using least squares and measure the deviation between the estimated coordinates from the ideal linear trajectory. The magnitude of this deviation is a reasonable measure of the tracking quality.

The camera is tilted downwards which results in movement of the ball not only along the vertical y axis but also results in a change of the measured depth along the z axis. Because motion is present only in the y/z plane, we fit a least squares regressor $z_t \approx ay_t + b$ to the estimated object position at step t . As error metric we choose the root mean squared error (RMSE),

$$\text{RMSE} = \sqrt{\frac{1}{T} \sum_{t=1:T} (z_t - (ay_t + b))^2}, \quad (10.10)$$

between the depth z_t , that was estimated with the model based tracking approach, and the depth value given by the regression.

We perform the above evaluation only for the second half timespan of each sequence, when the tracking algorithm has suitably converged, to avoid potential biases due to initialization effects. In all experiments, we use the same transition model and the same parameters in (10.5).

Experimental setup B. To allow for a better quantitative evaluation, we use a second experimental setup: The table tennis ball is attached to a rope together with two reflective markers that are tracked in 3D at 150 Hz using an eleven-camera motion capture system (Qualisys QTM, Qualisys Inc., Gothenburg, Sweden). We choose this setup and do not attach the markers directly to the table tennis ball, otherwise the brightness of the reflective markers would interfere with our model based tracking approach. Attached to the end of the rope is also a weight, which straightens the rope. For quantitative

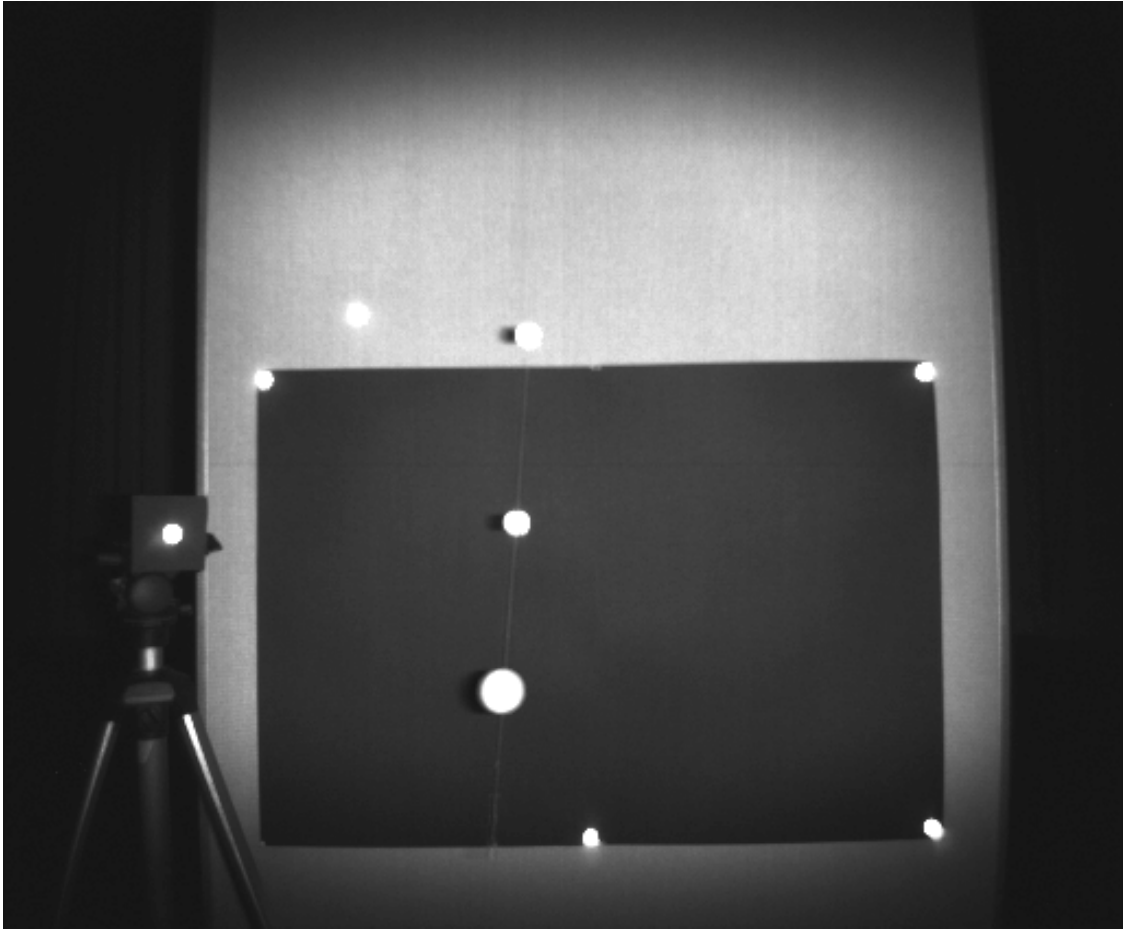


Figure 10.6.: Experimental setup B. A table tennis ball is attached to a rope with two reflective markers. Additional markers in the scene allow to register the coordinate frames of the camera and of the motion capture system. Shown is an averaged infrared image of the ToF camera.

comparison we transform the 3D trajectory of the motion capture system to the Kinect camera coordinate frame and compute the root mean squared error (RMSE) between the three dimensional coordinates of the raw ToF tracking result and the motion capture system output.

Notes on the accuracy: The motion capture system is calibrated with a residual of less than 2 mm. The coordinate frames of the Kinect camera and the motion capture system are registered by using six reflective markers which both are assigned a 3D coordinate by the motion tracking system and which are visible in the Kinect camera frame. In the Kinect camera frame, we measure the depth of the base plate of each marker using the standard depth reconstruction of the Kinect. Finally the registration of both coordinate frames is achieved by using Kabsch’s algorithm [74] with a residual of 8 – 9 mm.

10.5. Experiments

The proposed method combines the use of phase modulated raw ToF observations with a high frame rate. Therefore, we design the experiments to verify that both the ToF modulation and the equispaced timing of the captures are beneficial for tracking and verify that these benefits are complementary.

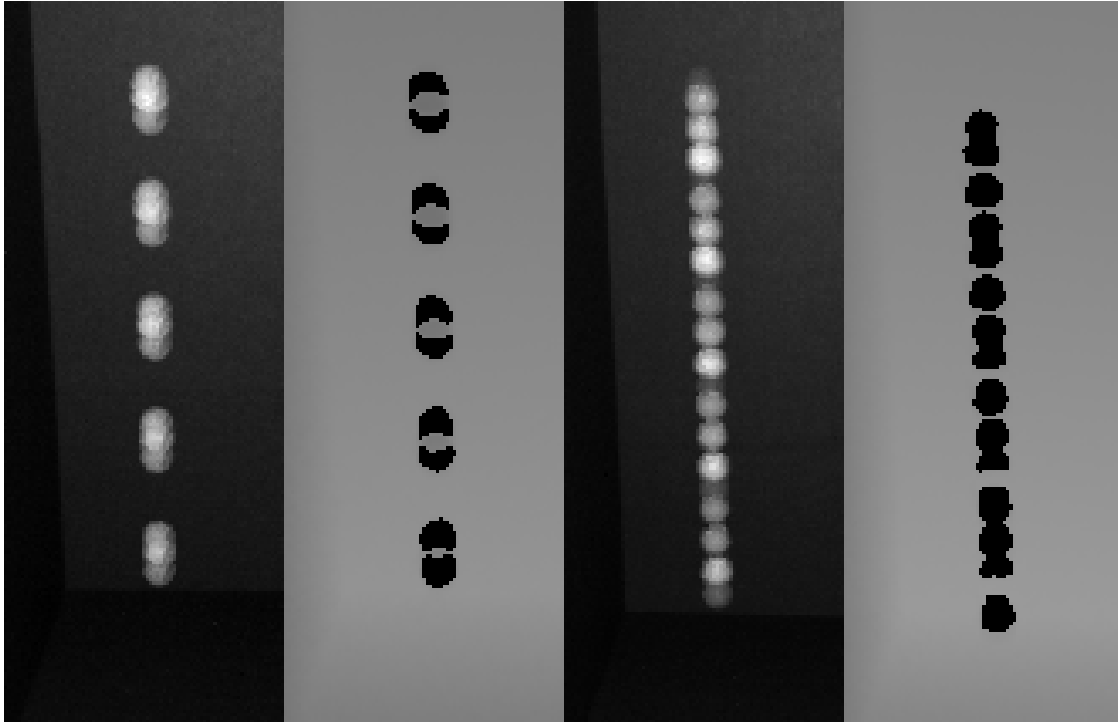


Figure 10.7.: Depth reconstruction failure (Experiment A). The ball quickly reaches a velocity that prevents a successful depth reconstruction by phase unwrapping. This is due to insufficient overlap of the object in the nine frames used for reconstruction. Left two images: an overlay of the raw captures for five frames and the corresponding depth reconstructions, using the standard ‘clustered’ exposure timing of the Kinect. Note that with increasing velocity the depth reconstruction fails in the non-overlapping regions (missing depth values are shown in black). Right two images: Equidistant exposure timing. Depth reconstruction now completely fails. However, we show that this timing is beneficial for the proposed tracking method because it can directly take advantage of the high frame-rate raw ToF information.

First we demonstrate that tracking based on phase unwrapping, the standard depth reconstruction method for ToF cameras, fails for fast moving objects because of motion artifacts due to insufficient overlap of the object in the individual exposures used for phase unwrapping.

10.5.1. Failure of Depth Based Tracking

The underlying assumption of a reconstruction algorithm based on phase unwrapping is a static scene. As a consequence, when an object moves between two raw frames and those frames are used for reconstructing the depth image, artifacts become visible in the depth reconstruction. Fig. 10.7 shows an overlay of the raw frames of the falling table tennis ball together with the depth reconstructions obtained from these frames by using phase unwrapping. A depth value can only be reconstructed in those regions where the moving object overlaps in all the raw frames used for the depth reconstruction. Therefore it is obvious that the strategy of first reconstructing a depth image and then tracking fast moving objects has to fail. We therefore propose to track the object in three dimensions by directly using the raw data of the sensor.

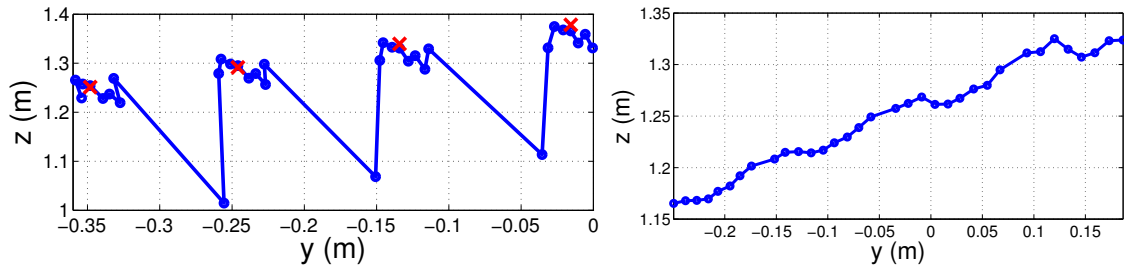


Figure 10.8.: Experiment A. Left: Validation of the estimated depth values when tracking in raw ToF images captured using the standard ‘clustered’ temporal spacing (blue), in comparison to the depth values of the standard time of flight reconstruction method (red). Right: Equispaced exposure timing leads to a more stable depth estimate when tracking from raw ToF captures.

10.5.2. Tracking with Raw ToF Observations

We now show that the unknown depth of an object can be obtained by the proposed model-based tracking approach. Fig. 10.8a depicts the estimated depth with respect to the vertical y coordinate of the falling table tennis ball (Experiment A). To validate the proposed method, we also depict the depth value which was reconstructed with the standard phase unwrapping approach. This value is acquired by averaging over those depth values, that are in the interior of the overlapping region of the table tennis ball in the depth image (this overlapping region is visible in Fig. 10.7).

In the standard exposure timing, all nine raw ToF captures are taken at the beginning of each 30Hz depth frame cycle in order to minimize motion artifacts. For tracking purposes these unevenly spaced exposures are suboptimal: the larger time-gap between the captures results in a low quality estimate of the depth in the first frame of each capture, leading to the sharp drop of the estimated depth in every 9th frame in Fig. 10.8a.

10.5.3. Benefit of Equispacing

To overcome the large time gap between the 30Hz captures we propose to use an equidistant timing of the exposures. Fig. 10.8b clearly demonstrates that this increases the stability of the trajectory estimates. Note that Fig. 10.8b tracks a different sequence than the sequence depicted in Fig. 10.8a, since due to interference we are unable to capture the same scene simultaneously with two cameras, and thus it is necessary to capture separate sequences for different exposure timings.

We also quantitatively compare the effect of the equidistant timing scheme in comparison with the standard clustered exposure timing. Therefore we compute the root mean squared error of the residual towards a linear regressor as explained in the beginning of this section. Both exposure timings are compared by individually tracking 10 sequences with 60 frames each of a table tennis ball falling straight to the ground. The camera is slightly tilted downwards which leads to a linear relation between the y and the z coordinate. Our results in Table 10.1 and Table 10.2 show first that the proposed model-based tracking method is highly accurate and second that the equidistant based shutter profile further improves this accuracy.

Table 10.1.: Experiment A. Quantitative comparison of the standard clustered exposure timing and the proposed equidistant timing for a table tennis ball accelerated by gravity.

		RMSE
Exposure timing	clustered	1.62 cm
	equidistant	1.59 cm

Table 10.2.: Experiment B. Quantitative comparison of the different exposure timings for a slow and fast moving table tennis ball. Shown is the root mean squared error between the raw ToF tracker and a commercial motion capture system, for all three coordinates (RMSE) and for the z coordinate in the camera coordinate frame (RMSE-z).

Exposure timing	Object Speed	RMSE	RMSE-z
clustered	1.40 kmh	4.15 cm	0.94 cm
	2.16 kmh	6.59 cm	2.59 cm
equidistant	1.12 kmh	2.40 cm	0.66 cm
	2.54 kmh	4.47 cm	1.39 cm

10.6. Discussion

The proposed method has two major benefits: First, tracking of an object directly in the raw ToF observations avoids the reconstruction of a depth frame and allows to track much faster motion, and second, equispacing of the raw ToF captures, which increases the stability of the tracking result.

10.6.1. Tracking from Raw ToF

The proposed observation model allows for direct computation of observation likelihoods against the raw ToF captures. In contrast to a comparison in the reconstructed depth frame, a potential benefit of the proposed approach is a reduction in computational cost: whereas a depth-based tracking approach first has to reconstruct a depth frame and then compute the likelihood between the model and the estimated depth, the presented approach allows to skip the potentially costly depth reconstruction process. This can be a significant advantage for power-limited environments, e.g. mobile devices.

An even greater benefit of the proposed raw ToF tracking approach is the avoidance of motion artifacts that would occur in phase unwrapping based depth reconstructions of fast moving objects (examples of fast motion that would cause problems are shown in Fig. 10.2). The individual exposure time of a single raw ToF frame is by an order of magnitude shorter compared to the time interval in which a full sequence of nine frames, used for phase unwrapping based depth reconstruction, is recorded, even when these exposures are clustered in the beginning of the depth frame cycle.

Still very fast object motion can result in motion blurring in the raw ToF capture. But in contrast to the motion artifacts due to phase unwrapping of a sequence of captures, motion blurring in a single raw ToF frame is negligible, because of the much shorter exposure time.

10.6.2. Equispaced ToF Captures

We proposed to space out the raw captures uniformly in time (see Fig. 10.1) and verified in our experiments that this increases the stability of the tracking result. While for the standard exposure timing the goal was to reconstruct depth, it was useful to cluster the frames in time to minimize motion between the captures and achieve the required consistence for phase unwrapping. In the proposed approach, we are instead interested in an exposure timing that is beneficial for tracking. By capturing the frames uniformly in time, the measurements better cover the movement of the object along the trajectory and allow an increased stability of the tracking result.

10.6.3. Limitations and Future Work

As we have demonstrated, the proposed raw ToF tracking framework allows several benefits in comparison to the standard approach of tracking in the depth image. But there are also some limitations in practice. Tracking an object in the ToF captures of a cluttered scene with dynamic background is much harder than tracking in the depth frame.

In future work we hope to generalize the model-based tracking approach to dynamic backgrounds and to allow for tracking more general objects including rigid-body motion and articulated objects. Furthermore, especially for articulated objects, we believe that the benefits of both methods, depth based tracking and raw ToF based tracking, can be combined. A combination allows to benefit from the strengths of both methods by using the more robust depth based tracking for slowly moving object parts and utilizing the higher time resolution of the raw ToF tracking approach for the faster moving parts. While the depth based tracking approach allows easier detection and tracking of the object itself, the raw ToF based approach allows tracking with high time resolution of those parts which move too quickly for a phase based depth reconstruction.

10.7. Conclusion

We proposed a novel framework for high-speed object tracking using an off-the-shelf ToF sensor. Experimental results confirm improved tracking accuracy due to two distinct contributions: an observation model which allows to compare a model based hypothesis against a raw ToF observation, and by spacing out the captures uniformly over time.

We see our work as a first step in adapting ToF sensor operation for computer vision tasks. Here we considered tracking, but other computer vision applications such as surface reconstruction and camera localization may benefit similarly from a co-design of algorithm and sensor operation. In this work we focused on adapting the algorithm to the specific characteristics of raw ToF flight data and used a fixed sensor operation, i.e. using exposure timings and specific frequency and phase delay configurations that are defined a priori. Possible future work could explore how to adaptively configure the sensor operation online depending on observed data and the estimated object trajectory.

Part IV.

Conclusions and Outlook

11. Concluding Remarks

11.1. Summary

In this thesis we presented convex optimization methods for two major computer vision tasks: image segmentation and 3D reconstruction.

We proposed a novel convex formulation of connectivity constraints for image segmentation and 3D reconstruction, that shows several advantages over the established boundary length regularization. The connectivity constraints allow the reconstruction of objects with fine thin structures and additionally increase the speed of convergence towards a smooth solution.

Furthermore, we described an active learning framework for the probabilistic model of the data term, which is especially useful for large scale segmentation problems. The active learning method asks for additional labels for parts of the data that have a high classification uncertainty, which leads to a quick improvement of the classification result.

As additional results, this thesis presented two real-time capable approaches: first, an improvement of our previous real-time dense 3D reconstruction method, and second, a novel approach for real-time object tracking with a time-of-flight camera.

11.2. Advantages

Connectivity Constraints for Image Segmentation We believe that the proposed combination of connectivity constraints with a total variation regularizer can become a new paradigm for image segmentation: Instead of just imposing a compact shape of the segmented object, we additionally formulate the connectivity of the object as a desired property of a valid segmentation. The presented approach has several advantages, including better performance when segmenting objects with thin parts, that would otherwise be smoothed by the regularizer. We demonstrated these benefits in experiments on real world datasets in different application areas: 3D reconstruction of dynamic scenes, 3D angiography, and 2D segmentation in a medical imaging dataset. The results on the medical image segmentation benchmark also demonstrate the practical importance of the proposed framework.

In a recent study, Rempfler et al. [117] compare the proposed method with the global optimal solution of the minimum cost connected subgraph, an NP-hard discrete combinatorial optimization problem that corresponds to the image segmentation problem (5.1) with general connectivity constraints (C0) without the perimeter term. They evaluate both methods on a medical image segmentation benchmark and find no statistically significant difference between both approaches, which validates that the proposed reformulated connectivity constraints yield a very good approximation to the NP-hard optimization problem.

Further more, the connectivity constraints allow to fill in missing parts of the object and, when combined with a total variation regularizer, allow faster convergence for acquiring

a smooth segmentation than with the total variation regularizer alone. To achieve this faster convergence, we developed an efficient projection scheme onto the feasible set of the constraints. This allows the application of connectivity constraints to large scale problems such as 3D reconstruction of dynamic scenes and large medical image segmentation problems.

Real-time Dense 3D Reconstruction The presented approach allows dense reconstructions with a handheld monocular camera in real-time. It contains two improvements in comparison to our earlier work: a dual variable approach for the data term and a robust Huber loss for the regularizer. When integrated together, these improvements result in a much faster run-time performance compared to the previously used half quadratic splitting approach. We achieve a performance of more than 40 fps on a single GPU. This performance increase allows the utilization of additionally available resources to perform high quality online camera pose estimation which, in combination with the proposed method, enables future work on full 3D reconstruction systems at interactive frame rates.

Raw Time-of-Flight Tracking We proposed a novel mode of operation for a time-of-flight camera, that is especially suited for tracking fast moving objects. With the standard approach of first reconstructing depth and performing tracking in the depth image, it is currently not possible to track objects which do not have sufficient overlap within the individual exposures used for depth reconstruction. The proposed method instead tracks the object in the raw infrared signal acquired by the time-of-flight camera. Furthermore, in contrast to the standard mode, where the raw exposures used for depth reconstruction are taken in quick succession, we proposed to distribute the individual exposures equally in time which increases the stability of the tracking output. While here we focus on object tracking, we believe that similar co-design of algorithm and sensor operation allows further improvements when solving other computer vision tasks, such as surface reconstruction and camera localization.

11.3. Limitations and Future Work

In the experiments on real world data sets, we confirmed that the presented approaches have several benefits in practical applications, *e.g.* the connectivity constraints allow a significant improvement on a medical image segmentation benchmark and are basically indistinguishable from the results of a global optimum solution of the more general minimum connected subgraph problem [117]. However, there are still some limitations that leave room for future work.

Connectivity Constraints In the proposed approach, the connectivity constraints are defined by a rooted tree, with a predefined root s . This leads to two limitations: first, the root needs to be specified, and second, the location of the root s also defines the topology of the tree.

In the current approach, the selection of a root was done either by the user, *e.g.* with a scribble in interactive image segmentation, or by an automated approach, as we demonstrated for dynamic 3D reconstruction. In general however, it would be desirable to remove this dependency on a particular root vertex.

The location of the root also influences the topology of the tree on which the constraints are defined and thus determines the quality of the result that can be achieved with the proposed approach. The constraints (C1) on the tree define a certain subset of feasible solutions, which does not necessarily contain the optimal least cost labeling that fulfills the general connectivity constraints (C0).

It turned out however, that the exact location is not very important in practice; *e.g.* in 3D reconstruction it is sufficient that the root is in the largest connected component. But if the root is far away from the optimal location, the tree shape that has to originate from the selected root, might not fit the topology of the data.

Future work could overcome these limitations by solving the NP-hard problem with the general connectivity constraints (C0) that do not require a particular root node. Recent work approaches this problem using integer linear programming [117, 145]. However, the long run-time still prohibits the application of these methods to large scale problems.

3D Reconstruction There are difficult problems remaining in 3D reconstruction, for example how to handle varying material properties, illumination changes, and how to represent large scale dynamic scenes. The particular choice of the scene representation is of key importance for the performance of a 3D reconstruction method. In the proposed real-time dense reconstruction approach, the scene is represented by a dense depth map. While the choice of this representation allows for the high frame rate of 41 frames per second, it only allows a limited representation of the scene. In our work on dynamic scene reconstruction, we instead used a labeling of a space-time volume with a continuous indicator function. This allows to reconstruct objects of arbitrary topology and also to represent a dynamically changing scene. However, this rich representation usually does not allow reconstructions in real-time. Future work could explore possible combinations of both approaches, how to achieve the run-time efficiency of a depth-map representation while still offering some topological flexibility of the representation. An example of such a hybrid representation is *DTAM* [101], which represents a surface by its indicator function in the visibility frustum of the camera. This method however is restricted to small environments and does not allow to represent a scene of larger scale.

Raw Time-of-Flight Tracking We demonstrated several benefits of the proposed method for tracking fast moving objects in comparison to the standard approach of reconstructing a depth image prior to tracking. However, there are also limitations in practice: object tracking in front of a cluttered background in the raw time-of-flight image can be much harder than tracking an object in a depth image. Future work could address these difficulties by applying strategies used for general object tracking in RGB images and by extending these existing methods to the phase encoded raw time-of-flight data.

Also, the current implementation is limited to rotationally invariant objects. However, we believe that the presented idea to perform tracking directly in the raw time-of-flight data is general, and thus should extend to existing tracking approaches for rigid body motion, deformable and articulated objects, *e.g.* the human hand [129].

For articulated objects, we believe that the proposed method can be combined with approaches which track the in depth image, and that both approaches are complementary. While slowly moving parts of the object can be tracked by using a more robust depth image based approach, object parts that undergo fast motions can be tracked with the proposed approach, thus combining the benefits of both methods.

References

- [1] E. Aganj, J.-P. Pons, F. Ségonne, and R. Keriven. Spatio-temporal shape from silhouette using four-dimensional delaunay meshing. In *Proc. International Conference on Computer Vision*, pages 1–8. 2007. (cited on page 74)
- [2] L. Ambrosio, N. Fusco, and D. Pallara. *Functions of bounded variation and free discontinuity problems*. Oxford Mathematical Monographs. The Clarendon Press Oxford University Press, New York, 2000. (cited on pages 15 and 77)
- [3] A. A. Amini, T. E. Weymouth, and R. C. Jain. Using dynamic programming for solving variational problems in vision. *Pattern Analysis and Machine Intelligence, IEEE Transactions on*, 12(9):855–867, 1990. (cited on page 38)
- [4] A. Andriyenko and K. Schindler. Multi-target tracking by continuous energy minimization. In *Computer Vision and Pattern Recognition (CVPR), 2011 IEEE Conference on*. IEEE, 2011. (cited on page 102)
- [5] X. Bai and G. Sapiro. A geodesic framework for fast interactive image and video segmentation and matting. In *Computer Vision, 2007. ICCV 2007. IEEE 11th International Conference on*, pages 1–8. IEEE, 2007. (cited on page 29)
- [6] C. S. Bamji, P. O’Connor, T. A. Elkhatib, S. Mehta, B. Thompson, L. A. Prather, D. Snow, O. C. Akkaya, A. Daniel, A. D. Payne, T. Perry, M. Fenton, and V.-H. Chan. A 0.13 μm CMOS system-on-chip for a 512×424 time-of-flight image sensor with multi-frequency photo-demodulation up to 130 MHz and 2 GS/s ADC. *J. Solid-State Circuits*, 50(1):303–319, 2015. (cited on pages 103, 105, and 109)
- [7] R. Barlow and H. Brunk. The isotonic regression problem and its dual. *Journal of the American Statistical Association*, 67(337):140–147, 1972. (cited on page 49)
- [8] C. Bauer, T. Pock, E. Sorantin, H. Bischof, and R. Beichel. Segmentation of interwoven 3d tubular tree structures utilizing shape priors and graph cuts. *Medical image analysis*, 14(2):172–184, 2010. (cited on page 28)
- [9] F. Benmansour and L. D. Cohen. Tubular structure segmentation based on minimal path method and anisotropic enhancement. *International Journal of Computer Vision*, 92:192–210, 2011. (cited on pages 28 and 29)
- [10] F. Benmansour, L. D. Cohen, M. Law, and A. Chung. Tubular anisotropy for 2d vessel segmentation. In *Computer Vision and Pattern Recognition, 2009. CVPR 2009. IEEE Conference on*, pages 2286–2293. IEEE, 2009. (cited on page 28)
- [11] M. Bergou, M. Wardetzky, S. Robinson, B. Audoly, and E. Grinspun. Discrete Elastic Rods. *ACM Transactions on Graphics (Proc. SIGGRAPH)*, 27(3):63:1–63:12, 2008. (cited on page 38)
- [12] B. Berkels. An unconstrained multiphase thresholding approach for image segmentation. In *International Conference on Scale Space and Variational Methods in Computer Vision*, pages 26–37. Springer, 2009. (cited on page 30)
- [13] M. Bleyer, C. Rother, P. Kohli, D. Scharstein, and S. Sinha. Object stereo—joint stereo matching and object segmentation. In *Proc. International Conference on Computer Vision and Pattern Recognition*, pages 3081–3088. IEEE, 2011. (cited on pages 75 and 87)

-
- [14] J. F. Blinn. Models of light reflection for computer synthesized pictures. *ACM SIGGRAPH Computer Graphics*, 11(2):192–198, 1977. (cited on page 107)
- [15] S. Bougleux, A. Elmoataz, and M. Melkemi. Discrete regularization on weighted graphs for image and mesh filtering. In F. Sgallari, A. Murli, and N. Paragios (Editors), *SSVM*, volume 4485 of *Lecture Notes in Computer Science*, pages 128–139. Springer, 2007. (cited on pages 33 and 34)
- [16] S. Boyd, N. Parikh, E. Chu, B. Peleato, and J. Eckstein. Distributed optimization and statistical learning via the alternating direction method of multipliers. *Foundations and Trends® in Machine Learning*, 3(1):1–122, 2011. (cited on page 14)
- [17] S. Boyd and L. Vandenberghe. *Convex Optimization*. Cambridge University Press, New York, NY, USA, 2004. (cited on pages 9, 10, and 11)
- [18] Y. Boykov and V. Kolmogorov. An experimental comparison of min-cut/max-flow algorithms for energy minimization in vision. *Pattern Analysis and Machine Intelligence, IEEE Transactions on*, 26(9):1124–1137, 2004. (cited on pages 25 and 32)
- [19] Y. Boykov, O. Veksler, and R. Zabih. Fast approximate energy minimization via graph cuts. *Pattern Analysis and Machine Intelligence, IEEE Transactions on*, 23(11):1222–1239, 2001. (cited on pages 27, 28, 32, and 60)
- [20] K. Bredies and D. Lorenz. Mathematische bildverarbeitung. *Vieweg+ Teubner*, 4(6):12, 2011. (cited on page 15)
- [21] A. Chambolle. An algorithm for total variation minimization and applications. *J. Math. Imaging Vis.*, 20(1-2):89–97, 2004. (cited on page 92)
- [22] A. Chambolle, V. Caselles, D. Cremers, M. Novaga, and T. Pock. An introduction to total variation for image analysis. *Theoretical foundations and numerical methods for sparse recovery*, 9(263-340):227, 2010. (cited on page 15)
- [23] A. Chambolle, D. Cremers, and T. Pock. A convex approach for computing minimal partitions. Technical report TR-2008-05, Dept. of Computer Science, University of Bonn, Bonn, Germany, 2008. (cited on pages 14, 15, 67, and 85)
- [24] A. Chambolle and T. Pock. A first-order primal-dual algorithm for convex problems with applications to imaging. *J. Math. Imaging Vis.*, 40(1):120–145, 2011. (cited on pages 14, 15, 33, 34, 47, 48, 67, 85, and 92)
- [25] T. Chan, S. Esedoğlu, and M. Nikolova. Algorithms for finding global minimizers of image segmentation and denoising models. *SIAM Journal on Applied Mathematics*, 66(5):1632–1648, 2006. (cited on pages 17, 28, 30, 60, 67, and 85)
- [26] T. F. Chan and L. A. Vese. Active contours without edges. *IEEE Trans. on Image Processing*, 10(2):266–277, 2001. (cited on page 28)
- [27] C. Chen, D. Freedman, and C. H. Lampert. Enforcing topological constraints in random field image segmentation. In *Proc. International Conference on Computer Vision and Pattern Recognition*, pages 2089–2096. IEEE, 2011. (cited on pages 27 and 28)
- [28] D. Comaniciu, V. Ramesh, and P. Meer. Kernel-based object tracking. *IEEE Trans. Pattern Anal. Mach. Intell.*, 25(5):564–575, 2003. (cited on page 102)

- [29] A. Criminisi, T. Sharp, and A. Blake. Geos: Geodesic image segmentation. In *Computer Vision–ECCV 2008*, pages 99–112. Springer, 2008. (cited on page 29)
- [30] L. Csató and M. Opper. Sparse on-line gaussian processes. *Neural Computation*, 14(3):641 – 668, 2002. (cited on page 60)
- [31] T. K. Dey, F. Fan, and Y. Wang. An efficient computation of handle and tunnel loops via reeb graphs. *ACM Trans. Graph.*, 32(4):32, 2013. (cited on page 80)
- [32] T. K. Dey, K. Li, J. Sun, and D. Cohen-Steiner. Computing geometry-aware handle and tunnel loops in 3d models. *ACM Trans. Graph.*, 27(3), 2008. (cited on page 80)
- [33] R. Diestel. *Graph Theory*. Springer-Verlag, Berlin, Heidelberg, 2006. (cited on pages 19 and 21)
- [34] E. Dijkstra. A note on two problems in connexion with graphs. *Numerische Mathematik*, 1:269–271, 1959. (cited on page 39)
- [35] A. Doucet and A. M. Johansen. A tutorial on particle filtering and smoothing: Fifteen years later. *Handbook of Nonlinear Filtering*, 12:656–704, 2009. (cited on page 106)
- [36] J. Douglas and H. H. Rachford. On the numerical solution of heat conduction problems in two and three space variables. *Transactions of the American mathematical Society*, 82(2):421–439, 1956. (cited on page 14)
- [37] J. Durbin and S. Koopman. *Time Series Analysis by State Space Methods: Second Edition*. Oxford Statistical Science Series. OUP Oxford, 2012. (cited on pages 105 and 106)
- [38] N. Y. El-Zehiry and L. Grady. Fast global optimization of curvature. In *Proc. International Conference on Computer Vision and Pattern Recognition*, pages 3257–3264. IEEE, 2010. (cited on pages 18, 25, and 52)
- [39] P. Elias, A. Feinstein, and C. Shannon. A note on the maximum flow through a network. *IRE Transactions on Information Theory*, 2(4):117–119, 1956. (cited on page 32)
- [40] A. Elmoataz, O. Lezoray, and S. Boughleux. Nonlocal discrete regularization on weighted graphs: A framework for image and manifold processing. *Image Processing, IEEE Transactions on*, 17(7):1047 –1060, 2008. (cited on pages 33 and 34)
- [41] J. Engel, J. Sturm, and D. Cremers. Semi-dense visual odometry for a monocular camera. In *Proc. International Conference on Computer Vision*. Sydney, Australia, 2013. (cited on pages 89, 90, and 96)
- [42] C. H. Esteban and F. Schmitt. Silhouette and stereo fusion for 3d object modeling. *Computer Vision and Image Understanding*, 96(3):367–392, 2004. (cited on pages 76 and 89)
- [43] H. Federer. Curvature measures. *Transactions of the American Mathematical Society*, 93(3):418–491, 1959. (cited on page 16)
- [44] P. F. Felzenszwalb and D. P. Huttenlocher. Efficient graph-based image segmentation. *International Journal of Computer Vision*, 59(2):167–181, 2004. (cited on page 61)

-
- [45] W. H. Fleming and R. Rishel. An integral formula for total gradient variation. *Archiv der Mathematik*, 11(1):218–222, 1960. (cited on page 16)
- [46] L. R. Ford and D. R. Fulkerson. Maximal flow through a network. *Canadian journal of Mathematics*, 8(3):399–404, 1956. (cited on page 32)
- [47] A. F. Frangi, W. J. Niessen, K. L. Vincken, and M. A. Viergever. Multiscale vessel enhancement filtering. In *Medical Image Computing and Computer-Assisted Intervention MICCAI 98*, pages 130–137. Springer, 1998. (cited on page 28)
- [48] N. Friedman and S. Russell. Image segmentation in video sequences: A probabilistic approach. In *Proceedings of the Thirteenth Conference on Uncertainty in Artificial Intelligence, UAI'97*. 1997. (cited on page 108)
- [49] Y. Furukawa and J. Ponce. Accurate, dense, and robust multiview stereopsis. *IEEE Transactions on Pattern Analysis and Machine Intelligence*, 32(8):1362–1376, 2010. (cited on pages 85 and 86)
- [50] D. Gabay and B. Mercier. A dual algorithm for the solution of nonlinear variational problems via finite element approximation. *Computers & Mathematics with Applications*, 2(1):17–40, 1976. (cited on page 14)
- [51] D. Geman and G. Reynolds. Constrained restoration and the recovery of discontinuities. 14(3):367–383, 1992. (cited on pages 89, 91, and 94)
- [52] G. Gilboa and S. Osher. Nonlocal operators with applications to image processing. *Multiscale Modeling & Simulation*, 7(3):1005–1028, 2008. (cited on page 34)
- [53] R. Glowinski and A. Marroco. Sur l’approximation, par éléments finis d’ordre un, et la résolution, par pénalisation-dualité d’une classe de problèmes de dirichlet non linéaires. *Revue française d’automatique, informatique, recherche opérationnelle. Analyse numérique*, 9(2):41–76, 1975. (cited on page 14)
- [54] B. Goldluecke and D. Cremers. Convex relaxation for multilabel problems with product label spaces. In *Proc. European Conference on Computer Vision*. 2010. (cited on page 17)
- [55] B. Goldluecke and D. Cremers. Introducing total curvature for image processing. In *Proc. International Conference on Computer Vision*. 2011. (cited on pages 18 and 25)
- [56] B. Goldluecke, I. Ihrke, C. Linz, and M. Magnor. Weighted minimal hypersurface reconstruction. *IEEE Transactions on Pattern Analysis and Machine Intelligence*, 29(7):1194–1208, 2007. (cited on page 74)
- [57] B. Goldluecke and M. Magnor. Space-time isosurface evolution for temporally coherent 3D reconstruction. In *Proc. International Conference on Computer Vision and Pattern Recognition*, volume I, pages 350–355. 2004. (cited on page 74)
- [58] N. J. Gordon, D. J. Salmond, and A. F. Smith. Novel approach to nonlinear/non-Gaussian Bayesian state estimation. *IEE Proceedings F (Radar and Signal Processing)*, 140(2):107–113, 1993. (cited on pages 105 and 106)
- [59] L. Grady. Random walks for image segmentation. *Pattern Analysis and Machine Intelligence, IEEE Transactions on*, 28(11):1768–1783, 2006. (cited on page 25)

- [60] J.-Y. Guillemaut and A. Hilton. Space-time joint multi-layer segmentation and depth estimation. In *Proc. International Conference on 3D Imaging, Modeling, Processing, Visualization and Transmission (3DIMPVT)*, pages 440–447. 2012. (cited on page 75)
- [61] V. Gulshan, C. Rother, A. Criminisi, A. Blake, and A. Zisserman. Geodesic star convexity for interactive image segmentation. In *Proc. International Conference on Computer Vision and Pattern Recognition*, pages 3129–3136. IEEE, 2010. (cited on page 27)
- [62] M. Gupta, S. K. Nayar, M. B. Hullin, and J. Martin. Phasor imaging: A generalization of correlation-based time-of-flight imaging. Technical Report, Department of Computer Science, Columbia University, 2014. (cited on page 104)
- [63] X. Han, C. Xu, and J. L. Prince. A topology preserving level set method for geometric deformable models. *Pattern Analysis and Machine Intelligence, IEEE Transactions on*, 25(6):755–768, 2003. (cited on pages 25, 27, and 28)
- [64] A. Handa, R. A. Newcombe, A. Angeli, and A. J. Davison. Real-time camera tracking: When is high frame-rate best? In *Computer Vision - ECCV 2012 - 12th European Conference on Computer Vision, Florence, Italy, October 7-13, 2012, Proceedings, Part VII*. Springer, 2012. (cited on page 102)
- [65] M. E. Hansard, S. Lee, O. Choi, and R. Horaud. *Time-of-Flight Cameras - Principles, Methods and Applications*. Springer Briefs in Computer Science. Springer, 2013. (cited on page 104)
- [66] M. Hein, J.-Y. Audibert, and U. von Luxburg. Graph laplacians and their convergence on random neighborhood graphs. *Journal of Machine Learning Research*, 8:1325–1368, 2007. (cited on page 33)
- [67] B. K. P. Horn and B. G. Schunck. Determining optical flow. *Artificial Intelligence*, 17:185–203, 1981. (cited on page 90)
- [68] P. J. Huber. Robust estimation of a location parameter. *The Annals of Mathematical Statistics*, 35(1):73–101, 1964. (cited on pages 94 and 95)
- [69] Institut national de recherche en informatique et en automatique (INRIA) Rhône Alpes. 4d repository. <http://4drepository.inrialpes.fr/>. (cited on pages 74 and 85)
- [70] M. Isard and A. Blake. CONDENSATION - conditional density propagation for visual tracking. *International Journal of Computer Vision*, 29(1):5–28, 1998. (cited on page 105)
- [71] M. Isard and A. Blake. A smoothing filter for CONDENSATION. In H. Burkhardt and B. Neumann (Editors), *Computer Vision - ECCV'98, 5th European Conference on Computer Vision, Freiburg, Germany, June 2-6, 1998, Proceedings, Volume I*, volume 1406 of *Lecture Notes in Computer Science*, pages 767–781. Springer, 1998. (cited on page 106)
- [72] M. Jancosek and T. Pajdla. Multi-view reconstruction preserving weakly-supported surfaces. In *Proc. International Conference on Computer Vision and Pattern Recognition*, pages 3121–3128. 2011. (cited on pages 85 and 86)

- [73] H. Jin, P. Favaro, and S. Soatto. Real-time 3-d motion and structure of point-features: A front-end for vision-based control and interaction. In *Proc. International Conference on Computer Vision and Pattern Recognition*, pages 2778–2779. 2000. (cited on page 89)
- [74] W. Kabsch. A solution for the best rotation to relate two sets of vectors. *Acta Crystallographica Section A*, 32(5):922–923, 1976. (cited on page 111)
- [75] A. Kapoor, K. Grauman, R. Urtasun, and T. Darrell. Gaussian processes for object categorization. *International Journal of Computer Vision*, 88(2):169–188, 2010. (cited on page 60)
- [76] M. Kass, A. Witkin, and D. Terzopoulos. Snakes: Active contour models. *International journal of computer vision*, 1(4):321–331, 1988. (cited on page 28)
- [77] M. M. Kazhdan, M. Bolitho, and H. Hoppe. Poisson surface reconstruction. In *Symposium on Geometry Processing*, pages 61–70. 2006. (cited on pages 85 and 86)
- [78] C. Kerl, J. Sturm, and D. Cremers. Robust odometry estimation for rgb-d cameras. In *Robotics and Automation (ICRA), 2013 IEEE International Conference on*, pages 3748–3754. IEEE, 2013. (cited on page 90)
- [79] G. Klein and D. Murray. Parallel tracking and mapping for small AR workspaces. In *Proc. Sixth IEEE and ACM International Symposium on Mixed and Augmented Reality (ISMAR’07)*. Nara, Japan, 2007. (cited on pages 90 and 96)
- [80] M. Klodt. *Convex Relaxation Methods for Image Segmentation and Stereo Reconstruction*. Dissertation, Technische Universität München, München, 2014. (cited on page 35)
- [81] M. Klodt, T. Schoenemann, K. Kolev, M. Schikora, and D. Cremers. An experimental comparison of discrete and continuous shape optimization methods. In *European Conference on Computer Vision (ECCV)*. Marseille, France, 2008. (cited on page 31)
- [82] K. Kolev, M. Klodt, T. Brox, and D. Cremers. Continuous global optimization in multiview 3d reconstruction. *International Journal of Computer Vision*, 84(1):80–96, 2009. (cited on pages 75 and 89)
- [83] D. Koller, K. Daniilidis, and H. H. Nagel. Model-based object tracking in monocular image sequences of road traffic scenes. *International Journal of Computer Vision*, 10(3):257–281, 1993. (cited on page 105)
- [84] K. Krissian, G. Malandain, N. Ayache, R. Vaillant, and Y. Troussel. Model-based detection of tubular structures in 3d images. *Computer Vision and Image Understanding*, 80(2):130–171, 2000. (cited on page 28)
- [85] M. Kristan, R. P. Pflugfelder, A. Leonardis, J. Matas, L. Cehovin, G. Nebehay, T. Vojír, G. Fernández, A. Lukežič, A. Dimitriev, A. Petrosino, A. Saffari, B. Li, B. Han, C. Heng, C. Garcia, D. Pangercic, G. Häger, F. S. Khan, F. Oven, H. Possegger, H. Bischof, H. Nam, J. Zhu, J. Li, J. Y. Choi, J.-W. Choi, J. F. Henriques, J. van de Weijer, J. Batista, K. Lebeda, K. Öfjäll, K. M. Yi, L. Qin, L. Wen, M. E. Maresca, M. Danelljan, M. Felsberg, M.-M. Cheng, P. H. S. Torr, Q. Huang, R. Bowden, S. Hare, S. Y. Lim, S. Hong, S. Liao, S. Hadfield, S. Z. Li, S. Duffner, S. Golodetz, T. Mauthner, V. Vineet, W. Lin, Y. Li, Y. Qi, Z. Lei, and Z. H.

- Niu. The visual object tracking VOT2014 challenge results. In *ECCV Workshops*. Springer, 2014. (cited on page 102)
- [86] C. H. Lampert and J. Peters. Real-time detection of colored objects in multiple camera streams with off-the-shelf hardware components. *Journal of Real-Time Image Processing*, 7(1):31–41, 2012. (cited on page 102)
- [87] R. Lange and P. Seitz. Solid-state time-of-flight range camera. *IEEE Journal of Quantum Electronics*, 37(3):390–397, 2001. (cited on page 104)
- [88] N. Lawrence, M. Seeger, and R. Herbrich. Fast sparse gaussian process methods: The informative vector machine. *Adv. in neural inf. proc. systems*, 15:609–616, 2002. (cited on page 60)
- [89] N. D. Lawrence, J. C. Platt, and M. I. Jordan. Extensions of the informative vector machine. In *Proc. of the First Intern. Conf. on Deterministic and Statistical Methods in Machine Learning*, pages 56–87. Springer-Verlag, 2004. (cited on page 64)
- [90] J. M. Lee. *Introduction to Topological Manifolds*. Springer-Verlag, New York, 2000. (cited on pages 19 and 20)
- [91] D. Lefloch, R. Nair, F. Lenzen, H. Schäfer, L. Streeter, M. J. Cree, R. Koch, and A. Kolb. Technical foundation and calibration methods for time-of-flight cameras. In *Time-of-Flight and Depth Imaging: Sensors, Algorithms, and Applications*, pages 3–24. Springer, 2013. (cited on page 104)
- [92] J. Lellmann, F. Becker, and C. Schnörr. Convex optimization for multi-class image labeling with a novel family of total variation based regularizers. In *2009 IEEE 12th International Conference on Computer Vision*, pages 646–653. 2009. (cited on page 17)
- [93] D. Lesage, E. D. Angelini, I. Bloch, and G. Funka-Lea. A review of 3d vessel lumen segmentation techniques: Models, features and extraction schemes. *Medical image analysis*, 13(6):819–845, 2009. (cited on page 28)
- [94] H. Lombaert, Y. Sun, L. Grady, and C. Xu. A multilevel banded graph cuts method for fast image segmentation. In *Proc. International Conference on Computer Vision*, pages 259–265. 2005. (cited on page 60)
- [95] W. E. Lorensen and H. E. Cline. Marching cubes: A high resolution 3d surface construction algorithm. *SIGGRAPH Comput. Graph.*, 21:163–169, 1987. (cited on page 76)
- [96] J. Moreau. Inf-convolution des fonctions numeriques sur un espace vectoriel proximite et dualite dans un espace hilbertien. *Comptes Rendus de l’Academie des Sciences de Paris*, 256:125–129, 1963. (cited on page 94)
- [97] J. Moreau. Proximite et dualite dans un espace hilbertien. *Bulletin de la Société Mathématique de France*, 93:273–299, 1965. (cited on page 94)
- [98] Y. Nakabo, M. Ishikawa, H. Toyoda, and S. Mizuno. 1ms column parallel vision system and it’s application of high speed target tracking. In *ICRA. IEEE*, 2000. (cited on page 102)
- [99] R. A. Newcombe and A. J. Davison. Live dense reconstruction with a single moving camera. In *Proc. International Conference on Computer Vision and Pattern Recognition*. 2010. (cited on page 89)

-
- [100] R. A. Newcombe, S. Izadi, O. Hilliges, D. Molyneaux, D. Kim, A. J. Davison, P. Kohi, J. Shotton, S. Hodges, and A. Fitzgibbon. Kinectfusion: Real-time dense surface mapping and tracking. In *Mixed and augmented reality (ISMAR), 2011 10th IEEE international symposium on*, pages 127–136. IEEE, 2011. (cited on page 89)
- [101] R. A. Newcombe, S. J. Lovegrove, and A. J. Davison. Dtam: Dense tracking and mapping in real-time. In *2011 international conference on computer vision*, pages 2320–2327. IEEE, 2011. (cited on pages 89 and 121)
- [102] C. Nieuwenhuis and D. Cremers. Spatially varying color distributions for interactive multi-label segmentation. *IEEE Transactions on Pattern Analysis and Machine Intelligence*, 35(5):1234–1247, 2013. (cited on pages 60, 63, 67, 68, and 69)
- [103] D. Nister. Preemptive ransac for live structure and motion estimation. In *Proc. International Conference on Computer Vision*, pages 199–206. 2003. (cited on page 89)
- [104] S. Nowozin and C. H. Lampert. Global connectivity potentials for random field models. In *Proc. International Conference on Computer Vision and Pattern Recognition*, pages 818–825. IEEE, 2009. (cited on page 27)
- [105] K. Okuma, A. Taleghani, N. de Freitas, J. J. Little, and D. G. Lowe. A boosted particle filter: Multitarget detection and tracking. In *Computer Vision - ECCV 2004, 8th European Conference on Computer Vision, Prague, Czech Republic, May 11-14, 2004. Proceedings, Part I*. Springer, 2004. (cited on page 102)
- [106] M. R. Oswald. *Convex Variational Methods for Single-View and Space-Time Multi-View Reconstruction*. Dissertation, Technische Universität München, München, 2015. (cited on page 73)
- [107] M. R. Oswald and D. Cremers. A convex relaxation approach to space time multi-view 3d reconstruction. In *ICCV - Workshop on Dynamic Shape Capture and Analysis (4DMOD)*. 2013. (cited on pages 73, 74, 75, 76, 85, and 86)
- [108] M. R. Oswald, J. Stühmer, and D. Cremers. Generalized connectivity constraints for spatio-temporal 3d reconstruction. In *Proc. European Conference on Computer Vision*, pages 32–46. 2014. (cited on pages 73, 80, 81, and 82)
- [109] P. M. Pardalos and G. Xue. Algorithms for a class of isotonic regression problems. *Algorithmica*, 23(3):211–222, 1999. (cited on pages 49, 50, and 51)
- [110] N. Parikh and S. P. Boyd. Proximal algorithms. *Foundations and Trends in optimization*, 1(3):127–239, 2014. (cited on pages 9, 14, and 94)
- [111] R. Paul, R. Triebel, D. Rus, and P. Newman. Semantic categorization of outdoor scenes with uncertainty estimates using multi-class Gaussian process classification. In *Proc. of the Intern. Conf. on Intelligent Robots and Systems (IROS)*. 2012. (cited on page 61)
- [112] T. Pock and A. Chambolle. Diagonal preconditioning for first order primal-dual algorithms in convex optimization. In *Computer Vision (ICCV), 2011 IEEE International Conference on*, pages 1762–1769. IEEE, 2011. (cited on pages 14, 35, 40, 85, and 94)
- [113] T. Pock, A. Chambolle, H. Bischof, and D. Cremers. A convex relaxation approach for computing minimal partitions. In *IEEE Conference on Computer Vision and*

- Pattern Recognition (CVPR)*. Miami, Florida, 2009. (cited on pages 14, 15, 17, 67, and 85)
- [114] T. Pock, D. Cremers, H. Bischof, and A. Chambolle. An algorithm for minimizing the piecewise smooth mumford-shah functional. In *Proc. International Conference on Computer Vision*. Kyoto, Japan, 2009. (cited on pages 14, 15, 34, 47, 48, 67, and 85)
- [115] T. Pock, T. Schoenemann, G. Graber, H. Bischof, and D. Cremers. A convex formulation of continuous multi-label problems. In *European Conference on Computer Vision (ECCV)*. Marseille, France, 2008. (cited on page 17)
- [116] C. E. Rasmussen and C. K. I. Williams. Gaussian processes for machine learning, 2006. (cited on page 65)
- [117] M. Rempfler, B. Andres, and B. Menze. The minimum cost connected subgraph problem in medical image analysis. In *MICCAI*. 2016. (Accepted). (cited on pages 4, 27, 42, 119, 120, and 121)
- [118] R. T. Rockafellar. *Convex analysis*. Princeton Landmarks in Mathematics. Princeton University Press, Princeton, NJ, 1997. Reprint of the 1970 original, Princeton Paperbacks. (cited on page 94)
- [119] D. A. Ross, J. Lim, R.-S. Lin, and M.-H. Yang. Incremental learning for robust visual tracking. *International Journal of Computer Vision*, 77(1-3):125–141, 2008. (cited on page 102)
- [120] C. Rother, V. Kolmogorov, and A. Blake. Grabcut: Interactive foreground extraction using iterated graph cuts. *ACM Trans. on Graphics (TOG)*, 23(3):309–314, 2004. (cited on page 60)
- [121] L. I. Rudin, S. Osher, and E. Fatemi. Nonlinear total variation based noise removal algorithms. *Phys. D*, 60(1-4):259–268, 1992. (cited on page 92)
- [122] O. Russakovsky, J. Deng, H. Su, J. Krause, S. Satheesh, S. Ma, Z. Huang, A. Karpathy, A. Khosla, M. Bernstein, A. C. Berg, and L. Fei-Fei. ImageNet Large Scale Visual Recognition Challenge. *International Journal of Computer Vision (IJCV)*, 115(3):211–252, 2015. (cited on page 59)
- [123] J. Santner, T. Pock, and H. Bischof. Interactive multi-label segmentation. In *Proc. Asian Conference on Computer Vision*, pages 397–410. Springer, 2011. (cited on pages 67 and 69)
- [124] T. Schoenemann and D. Cremers. Introducing curvature into globally optimal image segmentation: Minimum ratio cycles on product graphs. In *Proc. International Conference on Computer Vision*. Rio de Janeiro, 2007. (cited on page 18)
- [125] T. Schoenemann, F. Kahl, and D. Cremers. Curvature regularity for region-based image segmentation and inpainting: A linear programming relaxation. In *Proc. International Conference on Computer Vision*. Kyoto, Japan, 2009. (cited on page 18)
- [126] T. Schoenemann, F. Kahl, S. Masnou, and D. Cremers. A linear framework for region-based image segmentation and inpainting involving curvature penalization. *International Journal of Computer Vision*, 2012. (cited on pages 18 and 25)

-
- [127] R. Schwarte, Z. Xu, H.-G. Heinol, J. Olk, R. Klein, B. Buxbaum, H. Fischer, and J. Schulte. New electro-optical mixing and correlating sensor: facilities and applications of the photonic mixer device (PMD). In *Proc. SPIE*, volume 3100, pages 245–253. 1997. (cited on page 104)
- [128] J. A. Sethian. A fast marching level set method for monotonically advancing fronts. *Proceedings of the National Academy of Sciences*, 93(4):1591–1595, 1996. (cited on page 38)
- [129] T. Sharp, C. Keskin, D. Robertson, J. Taylor, J. Shotton, D. Kim, C. Rhemann, I. Leichter, A. Vinnikov, Y. Wei, D. Freedman, P. Kohli, E. Krupka, A. Fitzgibbon, and S. Izadi. Accurate, robust, and flexible real-time hand tracking. CHI, 2015. (cited on pages 101 and 121)
- [130] J. Shotton, T. Sharp, A. Kipman, A. Fitzgibbon, M. Finocchio, A. Blake, M. Cook, and R. Moore. Real-time human pose recognition in parts from single depth images. *Communications of the ACM*, 56(1):116–124, 2013. (cited on page 101)
- [131] J. Staal, M. D. Abràmoff, M. Niemeijer, M. A. Viergever, and B. van Ginneken. Ridge-based vessel segmentation in color images of the retina. *Medical Imaging, IEEE Transactions on*, 23(4):501–509, 2004. (cited on pages 42, 43, and 54)
- [132] J. Starck and A. Hilton. Surface capture for performance-based animation. *IEEE Computer Graphics and Applications*, 27(3):21–31, 2007. (cited on page 75)
- [133] C. Stauffer and W. E. L. Grimson. Adaptive background mixture models for real-time tracking. In *CVPR*. 1999. (cited on page 108)
- [134] J. Stühmer. *Ein Variationsansatz zur Schätzung von dichten Tiefenkarten im Kontext des Structure-from-Motion*. Diplomarbeit, TU Dresden, Germany, 2010. (cited on pages 6 and 89)
- [135] J. Stühmer and D. Cremers. A fast projection method for connectivity constraints in image segmentation. In X.-C. Tai, E. Bae, T. F. Chan, and M. Lysaker (Editors), *Proceedings of the International Conference on Energy Minimization Methods in Computer Vision and Pattern Recognition*, LNCS. 2015. (cited on page 45)
- [136] J. Stühmer, S. Gumhold, and D. Cremers. Parallel generalized thresholding scheme for live dense geometry from a handheld camera. In *ECCV Workshop on Computer Vision on GPUs (CVGPU)*. Heraklion, Greece, 2010. (Part of Diploma Thesis). (cited on pages 89, 92, and 94)
- [137] J. Stühmer, S. Gumhold, and D. Cremers. Real-time dense geometry from a handheld camera. In *Pattern Recognition (Proc. DAGM)*, pages 11–20. Darmstadt, Germany, 2010. (Part of Diploma Thesis). (cited on pages 89, 90, 91, 92, 97, 98, and 100)
- [138] J. Stühmer, S. Nowozin, A. Fitzgibbon, R. Szeliski, T. Perry, S. Acharya, D. Cremers, and J. Shotton. Model-based tracking at 300hz using raw time-of-flight observations. In *Proc. International Conference on Computer Vision*. Santiago, Chile, 2015. (cited on page 101)
- [139] J. Stühmer, P. Schröder, and D. Cremers. Tree shape priors with connectivity constraints using convex relaxation on general graphs. In *Proc. International Conference on Computer Vision*. Sydney, Australia, 2013. (cited on pages 25, 45, 46, 47, 48, 52, 54, 74, 86, and 87)

- [140] W. A. Sutherland. *Introduction to metric and topological spaces*. Clarendon Press, Oxford, 1975. (cited on pages 19 and 20)
- [141] P. Tanskanen, K. Kolev, L. Meier, F. Camposeco, O. Saurer, and M. Pollefeys. Live metric 3d reconstruction on mobile phones. In *Proceedings of the IEEE International Conference on Computer Vision*, pages 65–72. 2013. (cited on page 90)
- [142] R. Triebel, H. Grimmett, R. Paul, and I. Posner. Driven learning for driving: How introspection improves semantic mapping. In *Proc of Intern. Symposium on Robotics Research (ISRR)*. 2013. (cited on page 60)
- [143] R. Triebel, J. Stühmer, M. Souiai, and D. Cremers. Active online learning for interactive segmentation using sparse gaussian processes. In *German Conference on Pattern Recognition*. 2014. (cited on page 59)
- [144] J. Tsitsiklis. Efficient algorithms for globally optimal trajectories. *Automatic Control, IEEE Transactions on*, 40(9):1528–1538, 1995. (cited on page 38)
- [145] E. Turetken, F. Benmansour, B. Andres, P. Glowacki, H. Pfister, and P. Fua. Reconstructing curvilinear networks using path classifiers and integer programming. *IEEE Transactions on Pattern Analysis and Machine Intelligence*, PP(99):1–1, 2016. (cited on page 121)
- [146] M. Unger, T. Pock, M. Grabner, A. Klaus, and H. Bischof. A variational approach to semiautomatic generation of digital terrain models. In *5th International Symposium on Visual Computing*, LNCS. Springer, Las Vegas, Nevada, USA, 2009. (cited on pages 90 and 95)
- [147] M. Unger, T. Pock, W. Trobin, D. Cremers, and H. Bischof. Tvseg-interactive total variation based image segmentation. In *British Machine Vision Conference*, volume 2. Citeseer, 2008. (cited on pages 25 and 60)
- [148] J. Valentin, V. Vineet, M.-M. Cheng, D. Kim, J. Shotton, P. Kohli, M. Niessner, A. Criminisi, S. Izadi, and P. Torr. Semanticpaint: Interactive 3d labeling and learning at your fingertips. *ACM Trans. on Graphics (TOG)*, 2015. (cited on page 101)
- [149] A. Vezhnevets, E. J. Buhmann, and V. Ferrari. Active learning for semantic segmentation with expected change. In *Proc. International Conference on Computer Vision and Pattern Recognition*. 2012. (cited on pages 60 and 61)
- [150] S. Vicente, V. Kolmogorov, and C. Rother. Graph cut based image segmentation with connectivity priors. In *Proc. International Conference on Computer Vision and Pattern Recognition*. 2008. (cited on pages 27, 29, 41, 45, and 52)
- [151] D. Wang, C. Yan, S. Shan, and X. Chen. Active learning for interactive segmentation with expected confidence change. In *Proc. Asian Conference on Computer Vision*. 2012. (cited on pages 60 and 61)
- [152] M. Werlberger, W. Trobin, T. Pock, A. Wedel, D. Cremers, and H. Bischof. Anisotropic Huber-L1 optical flow. In *Proceedings of the British Machine Vision Conference (BMVC)*. London, UK, 2009. (cited on pages 90 and 95)
- [153] T. Whelan, H. Johannsson, M. Kaess, J. J. Leonard, and J. McDonald. Robust real-time visual odometry for dense rgb-d mapping. In *Robotics and Automation (ICRA), 2013 IEEE International Conference on*, pages 5724–5731. IEEE, 2013. (cited on page 90)

-
- [154] T. Whelan, M. Kaess, M. Fallon, H. Johannsson, J. Leonard, and J. McDonald. Kintinuous: Spatially extended kinectfusion. 2012. (cited on page 90)
- [155] A. D. Worrall, R. F. Marslin, G. D. Sullivan, and K. D. Baker. Model-based tracking. In P. Mowforth (Editor), *BMVC*, pages 1–9. BMVA Press, 1991. (cited on page 105)
- [156] H. Yang, L. Shao, F. Zheng, L. Wang, and Z. Song. Recent advances and trends in visual tracking: A review. *Neurocomputing*, 74(18):3823–3831, 2011. (cited on page 102)
- [157] A. Yilmaz, O. Javed, and M. Shah. Object tracking: a survey. *ACM Computing Surveys*, 38(4):13:1–13:45, 2006. (cited on page 102)
- [158] K. Yosida. Functional analysis. 1965. *Die Grundlehren der Mathematischen Wissenschaften*, 1965. (cited on page 94)
- [159] C. Zach, T. Pock, and H. Bischof. A duality based approach for realtime TV-L1 optical flow. In *Pattern Recognition (Proc. DAGM)*, LNCS, pages 214–223. Springer, Heidelberg, Germany, 2007. (cited on pages 90 and 91)
- [160] Y. Zeng, D. Samaras, W. Chen, and Q. Peng. Topology cuts: A novel min-cut/max-flow algorithm for topology preserving segmentation in n-d images. *Computer Vision and Image Understanding*, 112(1):81–90, 2008. (cited on page 27)
- [161] Z. Zivkovic. Improved adaptive Gaussian mixture model for background subtraction. In *ICPR*. 2004. (cited on page 108)